Theses and Dissertations   1. Thesis and Dissertation Collection, all items

2001-09

The NPS Virtual Thermal Image processing model

Kenter, Yucel

http://hdl.handle.net/10945/9737

NAVAL POSTGRADUATE SCHOOL
Monterey, California

THESIS

THE NPS VIRTUAL THERMAL IMAGE PROCESSING MODEL

by

Yucel Kenter

September 2001

Thesis Advisor:	A. W. Cooper
Thesis Co-Advisor:	R. J. Pieper

REPORT DOCUMENTATION PAGE			*Form Approved OMB No. 0704-0188*

Public reporting burden for this collection of information is estimated to average 1 hour per response, including the time for reviewing instruction, searching existing data sources, gathering and maintaining the data needed, and completing and reviewing the collection of information. Send comments regarding this burden estimate or any other aspect of this collection of information, including suggestions for reducing this burden, to Washington headquarters Services, Directorate for Information Operations and Reports, 1215 Jefferson Davis Highway, Suite 1204, Arlington, VA 22202-4302, and to the Office of Management and Budget, Paperwork Reduction Project (0704-0188) Washington DC 20503.

1. AGENCY USE ONLY *(Leave blank)*	2. REPORT DATE September 2001	3. REPORT TYPE AND DATES COVERED Master's Thesis	
4. TITLE AND SUBTITLE: The NPS Virtual Thermal Image Processing Model		**5. FUNDING NUMBERS**	
6. AUTHOR(S) Yucel Kenter			
7. PERFORMING ORGANIZATION NAME(S) AND ADDRESS(ES) Naval Postgraduate School Monterey, CA 93943-5000		**8. PERFORMING ORGANIZATION REPORT NUMBER**	
9. SPONSORING / MONITORING AGENCY NAME(S) AND ADDRESS(ES) N/A		**10. SPONSORING / MONITORING AGENCY REPORT NUMBER**	
11. SUPPLEMENTARY NOTES The views expressed in this thesis are those of the author and do not reflect the official policy or position of the Department of Defense or the U.S. Government.			
12a. DISTRIBUTION / AVAILABILITY STATEMENT Approved for public release; distribution is unlimited		**12b. DISTRIBUTION CODE**	

13. ABSTRACT *(maximum 200 words)*

A new virtual thermal image-processing model that has been developed at the Naval Postgraduate School is introduced in this thesis. This visualization program is based on an earlier work, the Visibility MRTD model, which is focused on predicting the minimum resolvable temperature difference (MRTD). The MRTD is a standard performance measure for forward-looking infrared (FLIR) imaging systems. It takes into account thermal imaging system modeling concerns, such as modulation transfer functions (MTFs), sampling, aliasing and noise, and provides virtual visual images that are associated with the thermal imaging system being modeled. This capability of the model allows the user to virtually evaluate the effects of component variation, noise, sampling and aliasing on the final four-bar image. The analysis demonstrated that aliasing effects in thermal images of four-bar patterns cannot, in general, be adequately modeled as noise. For example, the simulation experiments showed that under the right conditions aliasing can create a noticeable contrast enhancement in the output images.

14. SUBJECT TERMS FLIR-92 Model, Visibility MRTD Model, Infrared Imaging Systems; Aliasing Effects, Virtual Thermal Image Processing Model			15. NUMBER OF PAGES 193
			16. PRICE CODE

17. SECURITY CLASSIFICATION OF REPORT Unclassified	18. SECURITY CLASSIFICATION OF THIS PAGE Unclassified	19. SECURITY CLASSIFICATION OF ABSTRACT Unclassified	20. LIMITATION OF ABSTRACT UL

NSN 7540-01-280-5500

Standard Form 298 (Rev. 2-89)
Prescribed by ANSI Std. 239-18

i

THIS PAGE INTENTIONALLY LEFT BLANK

THE NPS VIRTUAL THERMAL IMAGE PROCESSING MODEL

Yucel Kenter
1st Lieutenant, Turkish Army
B.S., Turkish War College, 1994

Submitted in partial fulfillment of the
requirements for the degree of

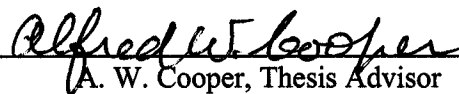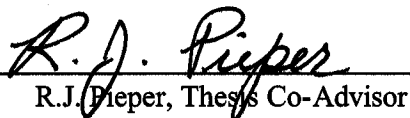**MASTER OF SCIENCE IN SYSTEMS ENGINEERING**

from the

NAVAL POSTGRADUATE SCHOOL
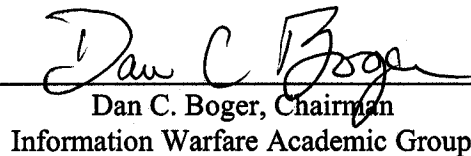**September 2001**

Author: _____
Yucel Kenter

Approved by: _____
A. W. Cooper, Thesis Advisor

_____
R.J. Pieper, Thesis Co-Advisor

_____
Dan C. Boger, Chairman
Information Warfare Academic Group

iii

THIS PAGE INTENTIONALLY LEFT BLANK

ABSTRACT

A new virtual thermal image-processing model that has been developed at the Naval Postgraduate School is introduced in this thesis. This visualization program is based on an earlier work, the Visibility MRTD model, which is focused on predicting the minimum resolvable temperature difference (MRTD). The MRTD is a standard performance measure for forward-looking infrared (FLIR) imaging systems. It takes into account thermal imaging system modeling concerns, such as modulation transfer functions (MTFs), sampling, aliasing and noise, and provides virtual visual images that are associated with the thermal imaging system being modeled. This capability of the model allows the user to virtually evaluate the effects of component variation, noise, sampling and aliasing on the final four-bar image. The analysis demonstrated that aliasing effects in thermal images of four-bar patterns cannot, in general, be adequately modeled as noise. For example, the simulation experiments showed that under the right conditions aliasing can create a noticeable contrast enhancement in the output images.

THIS PAGE INTENTIONALLY LEFT BLANK

TABLE OF CONTENTS

THIS PAGE INTENTIONALLY LEFT BLANK

LIST OF FIGURES

THIS PAGE INTENTIONALLY LEFT BLANK

LIST OF TABLES

THIS PAGE INTENTIONALLY LEFT BLANK

LIST OF SYMBOLS, ACRONYMS, AND/OR ABBREVIATIONS

α_T	Temporal correction factor
$\alpha(f_Z)$	Visibility model transference parameter
δ	Detector angular subtense (mrad)
δ_H	Detector horizontal instantaneous field of view (mrad)
δ_V	Detector vertical instantaneous field of view (mrad)
Δd	Pixel pitch (m)
Δf_N	Equivalent system noise bandwidth
Δf_P	Actual system noise bandwidth
ΔT	Target-to-background temperature difference (C)
ΔT_S	Contrast degraded temperature difference (C)
ΔT_{SC}	Minimum threshold resolvable contrast (C)
ΔV	Differential signal voltage produced by the thermal imager (V)
ΔV_{NOISE}	Differential noise voltage read on the oscilloscope screen (V)
ΔV_{SIGNAL}	Differential signal voltage read on the oscilloscope screen (V)
Δx	In-scan detector angular subtense (mrad)
Δy	Cross-scan detector angular subtense (mrad)
η	Vertical spatial frequency (cy/mrad)
η_{CS}	Cold shield efficiency
η_{SC}	Scan efficiency
λ	Wavelength (m)
μ	Micron (micrometer)
ν	Spatial frequency (cy/mrad)
θ	Scene phase angle (rad)
ρ_X	Noise filter factor

σ	Standard deviation of the monitor Gaussian blur spot diameter
σ_{ALIAS}	Visibility model alias-noise term
σ_{BLUR}	Standard deviation of the blur spot diameter
σ_{H}	Fixed column noise
σ_{T}	Frame-to-frame noise
σ_{TH}	Temporal column noise
σ_{TOTAL}	Overall system noise
σ_{TV}	Temporal row noise
σ_{TVH}	Random spatio-temporal noise
σ_{V}	Fixed row noise
σ_{VH}	Random spatial noise
σ^2_{WHITE}	Variance of Gaussian white noise
τ_{O}	Optical transmittance
ξ	Horizontal spatial frequency (cy/mrad)
Ω_{T}	Solid angle subtense of the square target (mrad^2)
$\partial N/\partial T$	Thermal gradient
A_{D}	Detector area (m^2)
A_{T}	Target area (m^2)
ATR	Automated target recognizer
A/D	Analog-to-digital
B_{FX}	Noise equivalent bandwidth in x direction
B_{FY}	Noise equivalent bandwidth in y direction
CCD	Charged-coupled devise
CRT	Cathode ray tube
D	Optics diameter (m)
D_{O}	Optics diameter (m)
DAS	Detector angular subtense (mrad)
D^{*}	Band averaged detector detectivity (cmHz$^{1/2}$ W^{-1})

$D^*(\lambda, 300)$	Detector noise-limited spectral detectivity
E_H	Horizontal integration factor
E_T	Temporal integration factor
E_V	Vertical integration factor
f	Two-dimensional spatial frequency (cy/mrad)
f_C	Electronics cutoff frequency (cy/mrad)
f_{MAX}	Maximum spatial frequency that can be represented using 2-D FFT in MATLAB (cy/mrad)
f_N	Nyquist frequency (samples/rad)
f_{NO}	Optical f-number
f_{OPTICS}	Optical focal length (m)
f_S	Sampling frequency (samples/rad)
f_x	Spatial frequency along the horizontal direction
f_y	Spatial frequency along the vertical direction
FFT	Fast Fourier Transform
FOV_X	In-scan field of view (mrad)
FOV_Y	Cross-scan field of view (mrad)
FPA	Focal plane array
F_R	Frame rate (Hz)
$F(x)$	Normalization function used in the Virtual Thermal Image-Processing model
$g(\alpha)$	Derivative of the normalization function $F(x)$
$h_{electronics}$	Electronics impulse response function
H_{blur}	Geometric blurred optical transfer function
H_{CCD}	CCD display transfer function
H_{CRT}	CRT display transfer function
$H_{detector}$	Detector transfer function
H_{DI}	Focal plane array integration transfer function
H_{DIG}	Digital filter transfer function
$H_{display}$	Display transfer function

H_{DS}	Detector spatial transfer function
H_{DSH}	Display sample and hold transfer function
H_{DT}	Detector temporal transfer function
H_{EB}	Boosting transfer function
H_{ELP}	Electronics low frequency response
H_{EHP}	Electronics high frequency response
$H_{electronics}$	Electronics transfer function
H_{eye}	Eye transfer function
$H_{imageformation}$	Image-formation transfer function
$H_{imagereconstruction}$	Image-reconstruction transfer function
H_{ML}	Linear image motion transfer function
H_{MR}	Random image motion transfer function
H_{MS}	Sinusoidal image motion transfer function
H_{MUX}	Electro-optical Multiplexor transfer function
H_{NFH}	Horizontal system noise filter transfer function
H_{NFV}	Vertical system noise filter transfer function
H_{ODL}	Diffraction limited optical transfer function
H_{OGB}	Geometric blurred optical transfer function
H_{optics}	Optical transfer function
H_{scene}	Sample scene phase transfer function
H_{SSP}	Sample scene phase transfer function
H_{SYSTEM}	Overall system transfer function
IFFT	Inverse Fast Fourier Transform
IR	Infrared
$I(\xi,\eta)$	Input spectrum
$I(f_x,f_y)$	Two-dimensional FFT of the four-bar pattern
i(x,y)	Input function
k_Z	Noise correction factor
L	Length-to-width aspect ratio of the target bar
LWIR	Long-wavelength infrared

MDT(D)	Minimum detectable temperature (difference)
MRT(D)	Minimum resolvable temperature (difference)
$MRTD_H$	Horizontal minimum resolvable temperature difference
$MRTD_V$	Vertical minimum resolvable temperature difference
$MRTD_{2D}$	Two-dimensional minimum resolvable temperature difference
MTF	Modulation transfer function
MTF_{blur}	Geometric blurred optical modulation transfer function
$MTF_{detector}$	Detector modulation transfer function
$MTF_{display}$	Display modulation transfer function
$MTF_{electronics}$	Electronics modulation transfer function
$MTF_{imageformation}$	Image-formation modulation transfer function
$MTF_{imagereconstruction}$	Image-reconstruction modulation transfer function
MTF_{optics}	Diffraction-limited optical modulation transfer function
MTF_{scene}	Scene-phasing modulation transfer function
MTF_{SYSTEM}	Overall system modulation transfer function
MWIR	Mid-wavelength infrared
n	Number of ripples observed along a bar
N_D	Number of detectors
N_{OS}	Over-scan ratio
N_{SS}	Serial scan ratio
N_V	Noise voltage (V)
NETD	Noise equivalent temperature difference
NPS	Naval Postgraduate School
NVESD	Night Vision Electronic Sensors Directorate
NVL	Night Vision Laboratory
o(x,y)	Output function
OTF	Optical transfer function
$O(\xi,\eta)$	Output spectrum
PSF	Point spread function

PtSi	Platinum Silicide
PTF	Phase transfer function
r_B	System back-end resolution (mrad)
r_S	Overall system resolution (mrad)
S	Global average
S_h	Samples per detector horizontal instantaneous field of view
s_v	Samples per detector vertical instantaneous field of view
S{}	System operator
S{ν}	Noise power spectrum
SNR	Signal-to-noise ratio
SNRT	Threshold signal-to-noise ratio
SWIR	Short-wavelength infrared
t_e	Eye integration time(s)
T	Spatial sampling period (Hz)
T_P	Average peak value (c)
T_T	Average trough value (c)
TDI	Time delay and integration
TIS	Thermal imaging system
U{T,V,H}	Composite noise data set used in FLIR-92
UV	Ultraviolet
V_S	Scan velocity (mrad/s)
W	Angular width of a bar (mrad)
z	Direction of interest either horizontal or vertical

THIS PAGE INTENTIONALLY LEFT BLANK

ACKNOWLEDGMENTS

First of all, I would like to thank the Turkish Army and the U.S. Navy for providing this great opportunity for me.

I would like to thank my thesis advisors, Professor Alfred W. Cooper and Professor Ron J. Pieper, for their valuable help and insight in the pursuit of this study. Their support, corporation and guidance made everything easier to work with.

I have special thanks for Mustafa Celik, Turkish Army, for his friendship and support during all stages of this thesis.

Finally, I would like to thank my family for always being there for me. I could not have finished my thesis without the great support and patience of my wife, Sevgi, and the fun hours spent with my lovely daughter Gulsah.

THIS PAGE INTENTIONALLY LEFT BLANK

I.   INTRODUCTION

With the discovery of the infrared radiation by Herschel, its applications became a major technology. Since then, the designers and the engineers have searched for a summary measure of quality in the evaluation process of infrared systems. Finally, the concept of minimum resolvable temperature difference (MRTD) proposed by Sendall and Lloyd [Ref.1] has been widely accepted as a figure of merit in predicting thermal imaging system (TIS) performance because it is the first comprehensive measure that includes system resolution, noise, and the observer into calculations.

The first standard model was the U.S. Army Night Vision Laboratory (NVL) Static Performance Model (also known as the Ratches Model), which was developed in 1975. It was a one-dimensional model that was used for the first-generation serial and parallel scanning thermal imaging systems. The model gained widespread acceptance for successfully treating the human eye-brain recognition process as a matched filter; however, it did not incorporate sampling effects and noise sources other than the detector noise [Ref. 1]. Moreover, improvements in the second-generation thermal imaging systems, such as the widespread use of focal plane arrays (FPA) and digital signal processing technology made it necessary to revise the so-called Ratches Model.

Therefore, the U.S. Army Night Vision Laboratory and Electronic Sensors Directorate (NVESD) presented a new model, called FLIR-90, that was later refined to FLIR-92. FLIR-92 was capable of introducing the 3-D noise effects into the model and predicting the two-dimensional MRTD values successfully, but it did not account for scene-phasing effects. Furthermore, it did not address the aliasing problem that was experienced due to the undersampling process in the FPAs. Since the treatment of sampling effects limited the MRTD predictions to sub-Nyquist frequencies, the information above the Nyquist frequency was not completely quantified by FLIR-92. Hence, the range performance of the system was artificially limited [Ref. 2].

The above named models named above made some assumptions regarding human eye-brain judgement in the recognition process, which brought some limitations to the performance predictions of the thermal imagers. Therefore a visibility model, which predicts the MRTD of second generation thermal imaging systems based on a minimum threshold input contrast parameter and a contrast reduction factor due to aliasing and blurring effects was proposed by A.W.Cooper and R.J.Pieper of the Naval Postgraduate School in 1994. The model makes no assumptions about the recognition process, and thus it suggests defining an individual threshold value for each observer (either human or machine). Moreover, the model includes the aliasing phenomenon and provides MRTD predictions beyond the Nyquist frequency limit [Ref. 3].

In 1999, NVTherm was developed by NVEOD as a new model adopting two major modifications to FLIR-92, which were the new eye model and the MTF squeeze phenomenon. The new eye model brought a limitation to the eye spatial resolution capability, which made the results more realistic. On the other hand, the MTF squeeze phenomenon degraded the system MTF to account for aliasing effects by taking the frequencies beyond the Nyquist limit into consideration [Refs. 4 and 5].

There is no doubt that staring systems will be dominant in this discipline someday. Furthermore, many possible developments are expected in the next generation of thermal-imaging technology. Today some of the topics of interest are: a near-unity fill-factor detector array, two or more colored-images, automated motion detection, tracking and identification functions on the focal plane arrays, user-friendly image processing, 3-D image processing and passive millimeter wave imaging on the same FPA with infrared. [Ref. 6] No matter how far the thermal imaging system technology improves, the practical modeling efforts in predicting its performance will definitely continue.

The main objective of this thesis is to develop a virtual thermal image-processing model [Ref. 23], which takes some of the current thermal imaging system modeling concerns into account, such as noise, sampling and aliasing, and creates visual images that can be obtained with the actual thermal imaging systems being modeled. A further analysis of these images will provide some useful insights into the problems encountered

2

in modeling efforts. Besides that, it is also intended to validate the performance of the Visibility Model by comparing the subjective and objective MRTD predictions to the measurement results in this thesis.

As a starting point, the fundamentals of thermal imaging systems and their operation will be explained in Chapter II. Chapter III will provide a general overview of the principles behind the FLIR-92 model. Considering that the Virtual Thermal Image-Processing model is based on the Visibility Model, Chapter IV will discuss the Visibility concept with the latest modifications. Then the experimental setup and the methodology used in subjective and objective MRTD measurements will be presented in Chapter V. This chapter will also provide the measurement results and a comparative analysis to the predictions obtained from the Visibility and FLIR-92 Models. Next, the Virtual Thermal Image-Processing model will be introduced in Chapter VI. Chapter VII will analyze the images created by this model, and this work will conclude with some conclusions and suggested directions for future studies.

THIS PAGE INTENTIONALLY LEFT BLANK

II.   THERMAL IMAGING SYSTEMS

The purpose of this chapter is to give a summary of the basic principles of thermal imaging system operation, which will be necessary for the reader in understanding the content of the following chapters.

A.   TYPICAL THERMAL IMAGING SYSTEM OPERATION

The region of the electromagnetic spectrum covering optical wavelengths is called the optical spectrum, including the ultraviolet (UV), the visible, and the infrared (IR) spectral bands. The ultraviolet (UV) spectral band occupies the wavelengths from 0.1 to 0.4 μm while the visible spectral band occupies the wavelengths from 0.4 to 0.7 μm where the human eye can produce images. Bounded by the visible and the microwave spectral bands, the infrared spectral band is also divided into four sub-regions. These are: the near infrared or short-wavelength infrared (SWIR) band from 0.7 to 3 μm, the mid-wavelength infrared (MWIR) band from 3 to 8 μm, the long-wavelength infrared (LWIR) band from 8 to 14 μm, and the far and the extreme infrared bands from 14 to 1000 μm, respectively. The corresponding spectra can be seen in Figure 2.1 [Ref. 7].
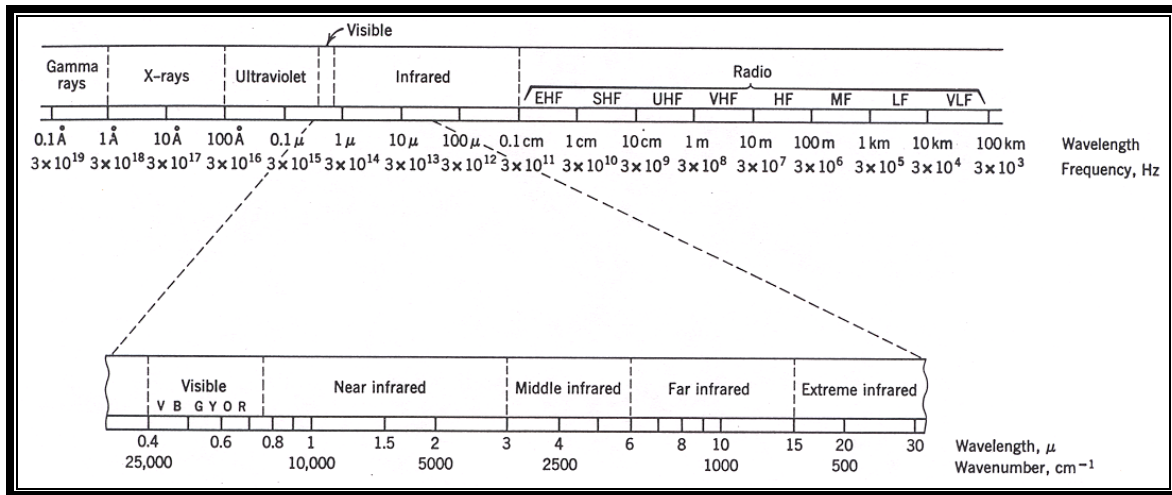
Figure 2.1.   The Electromagnetic Spectrum [Ref. 8].

Thermal imagers are passive optical systems, which are used to extend the human vision beyond the visible spectral region limits by making the naturally generated radiation in the mid-wavelength and long-wavelength infrared regions visible. Thermal imagers (i.e. Forward Looking Infrared (FLIR) Systems) sense the self-emitted thermal energy of the target and the background in the field of interest. Unlike thermal imagers, the electro-optical systems (e.g. night vision devices) utilize the reflected energy from the target and the background in the near infrared region, which is generated by an external energy source (i.e. starlight). Therefore, the reflectivity characteristics of the target and background become an interest area of electro-optical imaging studies, while the emissivity reflectivity characteristics of the target and background become an interest area of the thermal imaging studies [Refs. 9 and 10].
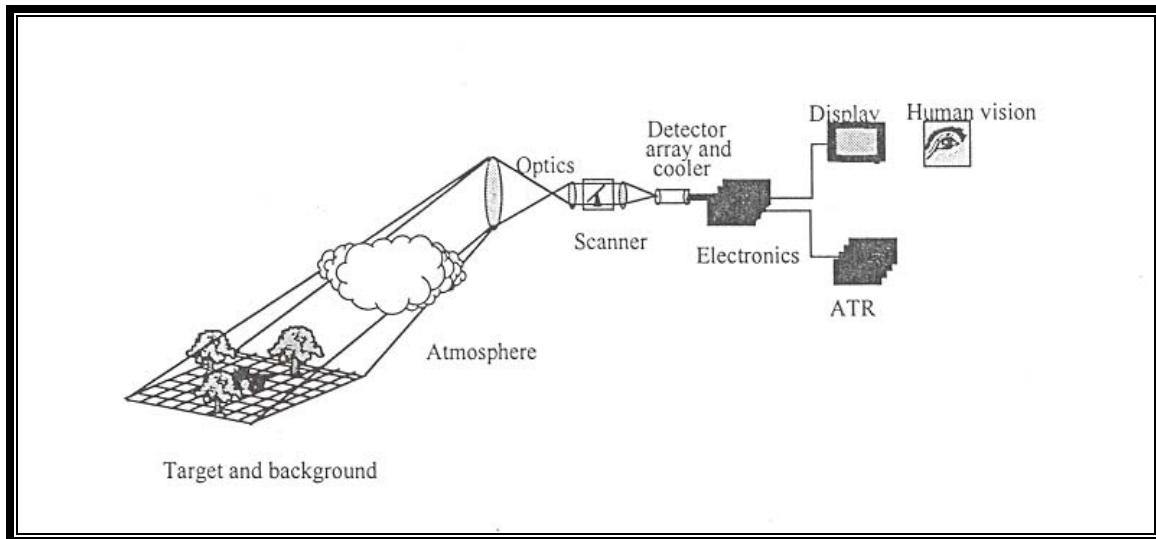
Figure 2.2.   Thermal Imaging System Block Diagram [Ref. 9].

A simplified diagram illustrating the fundamental components of a thermal imaging system is presented above in Figure 2.2. First, a target should produce a sufficient target-to-background apparent temperature difference in order to be detected, recognized or identified.   Then the radiation from the scene of interest, which is a combination of the target, the background and the atmospheric properties, passes through the atmosphere on the way to the sensor. The atmosphere modifies the amplitude and the

phase of the radiated light between the scene and the sensor by absorbing and scattering. These phenomena together degrade the information content of the radiation reaching the sensor. Moreover, unwanted rays of light are reflected into the sensor aperture. [Refs. 9, 10, 11]

The first component of the sensor, the optics, gathers the incoming radiation, filters it spectrally and spatially and focuses it at the optics image plane, where a detector is mounted. The detector converts the optical signals into analog electrical signals, which represent the spatial distribution of the radiant flux intensity leaving the scene. [Ref. 10]

The sensor detector may be a single detector, a linear array (a column or a few columns) or a two-dimensional staring array. No matter what kind of detector system is mounted at the image plane, the sampling phenomenon, which is necessary for the image formation in the latter stages of the process, is accomplished there. In the scanning systems (single detector systems or linear array detector systems) the image is moved across the detector(s) while the image is sampled perpendicular to the scanning direction. The output of every single detector symbolizes the local scene intensity across a scanning line. The staring array technology does not require a scanner mechanism because the image of the scene is sampled by the physically separated detector elements in the array [Refs. 4 and 9].

Due to the differing objects in the scene of interest, the scene intensity distribution results in various detector output voltage levels. Therefore, the output voltage distribution of the detector array produces an electronic signal after being processed and amplified by the electronics. The electronic analog signal is usually digitized for ease of manipulation in the reconstruction process of the image. The main goal of the electronics here is to arrange the signal at the detector output so that it becomes applicable to be displayed for the human observer. The video display may or may not be a component of the system in case the signal is arranged for an automated image processing system (i.e. automated target recognizer (ATR)) whose output is adopted for operator tracking [Refs. 4, 9 and 11].

B. LINEAR SYSTEM THEORY

A system is the mapping of an input function into an output function. The input and output functions have different characteristics for the various systems. For example, these functions for the electrical networks are real for which time is the only independent variable. On the other hand, for the imaging systems where space is the two-dimensional independent variable, they can be either real or complex [Ref. 12]

A convenient mathematical representation of an imaging system can be the operator $S\{\}$. The response of the system to the input function yields the output function. If i(x,y) and o(x,y) are the input and the output functions respectively, the input-output relation of the system can be represented as:

$$S\{i(x,y)\} = o(x,y) \qquad (2.1)$$

where x and y are the spatial variables [Ref. 9].

In order to call a system linear there are two essential requirements to be met: the superposition and scaling properties should be applicable to the system. The superposition property suggests that the response of the system to the sum of all input functions is equal to the sum of the individual system responses to each input function as stated in Equation (2.2) where $i_1(x,y)$ and $i_2(x,y)$ are individual input functions.

$$S\{i_1(x,y) + i_2(x,y)\} = S\{i_1(x,y)\} + S\{i_2(x,y)\} \qquad (2.2)$$

On the other hand, scaling property suggests that a scale factor applied at the input results in the same scale factor at the output of the system. Using the same notation, this property can be expressed as in Equation (2.3) where K represents the constant scaling factor [Refs. 9 and 12].

$$S\{K\,i(x,y)\} = K\,S\{i(x,y)\} = o(x,y) \qquad (2.3)$$

8

The advantage of linearity is essential in the imaging system analysis because it allows us to decompose a complicated input function into a group of much simpler input functions to calculate the system responses to each of these elementary inputs. Thus, the superposition of the calculated individual responses yields the total system response. One such decomposition process can be performed using Fourier analysis [Ref. 12].

The system response to a delta function is called the impulse response for electronic networks, or point spread function (PSF) for the optical imaging systems. Since imaging is a convolutionary process, once the imaging system's response behavior to a delta function is fully described, then the output to any input function can easily be determined. Equation 2.4 represents the two-dimensional convolution integral of the input function with the system's point spread function h(x,y) where α and β are dummy variables.

$$o(x,y) = \int_{-\alpha}^{+\alpha} \int_{-\alpha}^{+\alpha} i(\alpha,\beta)\, h(x-\alpha, y-\beta)\, d\alpha d\beta \qquad (2.4)$$

The Fourier Transform of the point-spread function is called the optical transfer function (OTF) while the Fourier Transform of the impulse response is called the transfer function in a general fashion. Note that any transfer function is the frequency domain representation of an impulse response function. Remembering the Fourier property that the convolution in the temporal domain corresponds to multiplication in the frequency domain, Equation 2.4 can be rewritten as Equation 2.5 where $O(\xi,\eta)$ and $I(\xi,\eta)$ are the output and the input spectrum representations respectively, and $H(\xi,\eta)$ is the transfer function. Notice that $I(\xi,\eta)$ and $O(\xi,\eta)$ are the Fourier Transforms of i(x,y) and o(x,y) functions where ξ and η are horizontal and vertical spatial frequencies respectively which have units in cycles per radian.

$$O(\xi,\eta) = I(\xi,\eta)H(\xi,\eta) \qquad (2.5)$$

At this point, it is appropriate to discuss the relationship between temporal and spatial frequencies. Just as temporal frequency is often a convenient parameter in

9

describing electrical signals, spatial frequency is often used to describe objects, their images and imaging systems designed to render these images. Whereas an electrical signal can be described in terms of its amplitude, characteristics or in the Fourier Transform domain by its frequency content, an object can be described in space by its radiance or its spatial frequency content.

As mentioned previously in Chapter II, the detector component converts the incoming photon energy into electrical energy. This suggests the necessity of using both spatial and temporal frequencies in thermal imaging system analysis. However, spatial frequency analysis is easier to apply in sensor performance calculations because spatial frequency is range-independent by definition. Therefore, the temporal frequencies are generally converted into spatial frequencies using Equation 2.6 for scanning systems.

$$f = \xi \times v_{SCAN} \tag{2.6}$$

Where

f is the temporal frequency in Hz

v_{SCAN} is the scan velocity in mrad/s or m/s

ξ is the spatial frequency in cycles/mrad or cycles/m

C.   OPTICAL TRANSFER FUNCTION THEORY

As mentioned in the previous section, the optical transfer function is simply defined as the Fourier Transform of the point spread function. The optical transfer function is multiplied with the input spectrum in order to calculate the output spectrum of a system meaning that each frequency component of the input spectrum is weighted and altered by a factor determined by the optical transfer function [Ref. 9].

In the case of a cascaded system, the product of each sub-system transfer function (assuming the sub-system impulse responses being linear and independent of each other) would determine the overall system transfer function. Notice that it is more practical to do the computations in the spatial frequency domain than to do them in the spatial

domain because the simple product of the transfer functions will replace the complicated operation of the multiple convolution integrals in the spatial domain [Ref. 10].

The transfer function for optical systems, in other words, the optical transfer function (OTF) is a complex quantity as mentioned earlier in this chapter. The magnitude of OTF yields the modulation transfer function (MTF), which is a sine wave amplitude response function. By convention, MTF approaches zero at the system cut-off spatial frequency, which indicates the highest detail of the target that can be reproduced by the system. The phase of the OTF gives the phase transfer function (PTF) that denotes the phase shifts brought about by the system [Ref. 10]. Equation (2.7) obviously shows the relationship between OTF, MTF and PTF functions.

$$OTF \ (\xi, \eta) = MTF \ (\xi, \eta) e^{\ jPTF \ (\xi, \eta)} \tag{2.7}$$

The effect of PTF can be neglected if the impulse response is a symmetric function. In that case, MTF becomes the primary physical parameter in the specification of the thermal imaging system and its components. Moreover, in the areas of the system requirement analysis, optimum system design and the system trade-off analysis, it is one of the system parameters most commonly manipulated by the system designers and system engineers.

However, using MTF theory requires some assumptions. Although the linear theory and the MTF theory provide very practical tools to the system evaluation analysis, there is a great concern about the assumptions that are made because they are frequently violated to some extent in real system applications. For example, individual detector responses in a detector array being uniform, the electronic processing being linear and the system mapping being single valued and non-noisy are some of the primary violations that have been experienced [Ref. 10].

D.   RESOLUTION AND SENSITIVITY

The thermal imaging systems' image quality specifications and sensor trade-off studies are after discussed in terms of spatial resolution and sensitivity. Resolution refers

to how well a sensor can perceive and reproduce the smallest detail of the target while sensitivity gives a visual measure of how well the sensor can detect a target signal in the presence of noise [Ref. 4].

Although resolution and sensitivity are conflicting terms most of the time, change in one affects the other. The relationship between sensitivity and resolution is indicated schematically in Figure 2.3, which reveals that there is a significant trade-off between resolution and sensitivity. Neither resolution nor sensitivity defines the overall sensor performance very well, but together they produce a more comprehensive characterization [Ref. 9].
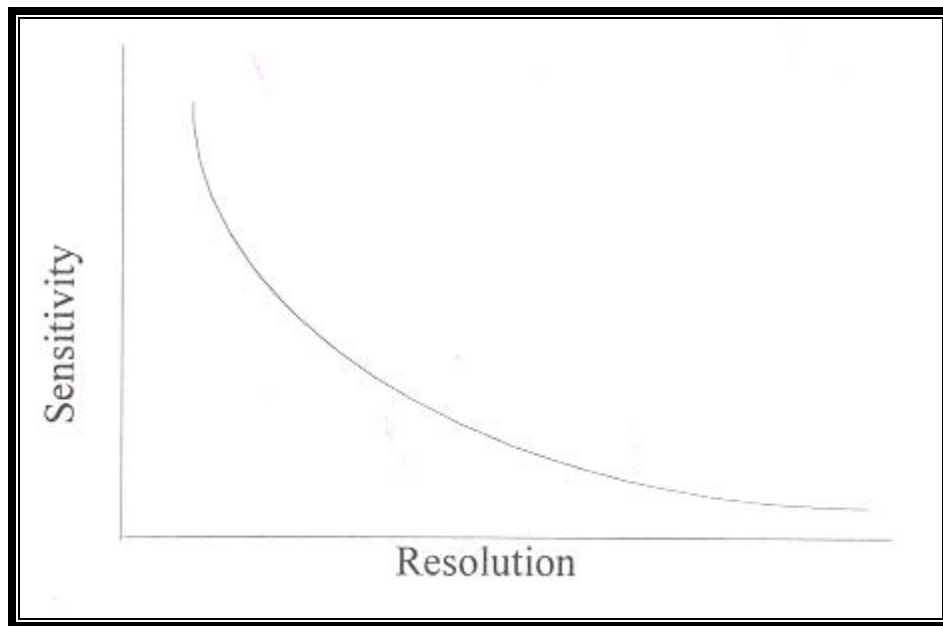
Figure 2.3.   Resolution and Sensitivity Relationship [Ref. 9].

Sensitivity becomes especially important when viewing or detecting the signals from the target of interest immersed in the noise generated by a variety of sources. These sources, either environmental or sensor-based, introduce noise in every stage of the thermal imaging process [Ref. 9]. Therefore, radiometry which describes the amount of energy leaving the object space and arriving at the sensor, light gathering properties of

optics design, detector performance specifications such as responsivity, and system noise become essential tools in the system sensitivity analysis [Refs. 4 and 9].

Sensitivity is usually described by a noise equivalent parameter, frequently defined as the target-to-background radiance difference giving a signal to noise ratio (SNR) of one at the sensor (i.e. NEI). Noise equivalent temperature difference (NETD) is a commonly used noise equivalent parameter, which is a good measure of sensitivity, measured at the amplified detector output of the thermal imager. [Refs.9 and 10]

On the other hand, resolution is the capability of the sensor that makes the discrimination tasks of detection, recognition and identification applicable, when a sufficient level of sensor sensitivity is achieved. Resolution depends on the sensor sub-system parameters such as optical aberration and diffraction, detector size, detector shape and focal length of the optical aperture. Moreover, the electronic bandwidth, the display resolution and many other parameters influence the sensor overall resolution capacity. Notice that resolution does not involve the noise effects [Refs. 4 and 9].

The resolution requirement of a sensor is determined by the most stringent demand of the recognition task. More stringent discrimination tasks, such as identification, are mostly performed in a narrow field-of-view. Field-of-view is defined as the system's total angular space in the scene from where the radiation is received. Due to the technological limitations of the number of detectors in a focal plane array and the number of corresponding samples taken across the target, a narrow field-of-view provides more samples across a smaller area within the scene, providing more details on the target. Today there are sensors having both narrow field-of-view capability providing better resolution and wide field-of-view providing better coverage over large areas [Ref. 9].

E.   SAMPLING THEORY AND ALIASING

Sampling is an unavoidable process in all real thermal imaging systems in which an array of the samples is taken from a two-dimensional image function at a discrete set of points in the image plane. These samples will represent the original image function if the samples are taken sufficiently close to each other. Consequently, the original function

would be reconstructed by a simple interpolation applied to the sampled values with considerable accuracy to form the original image [Ref. 12].

Horizontal Pixel Pitch

Vertical Pixel Pitch
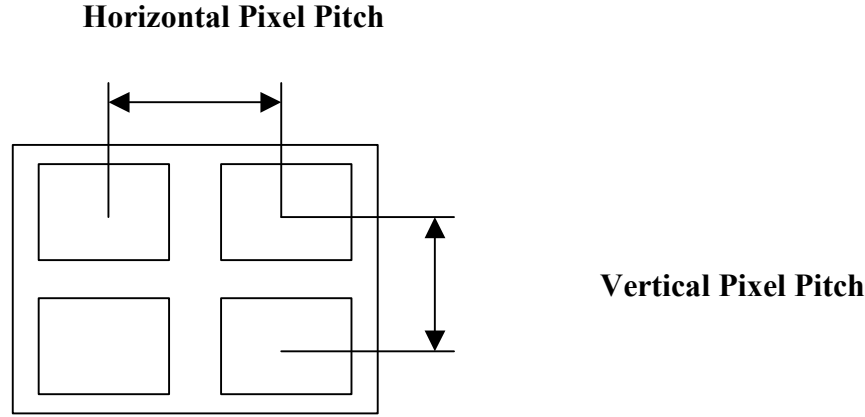
Figure 2.4.   Spatial Sampling in a FPA.

Sampling can be performed in several ways and in several dimensions. In scanning systems, the detector acts as a sampling aperture while the analog-to-digital (A/D) converter acts as a second sampler in case the detector output is digitized. In staring systems, the discrete detectors present in a focal plane array sample the scene spatially [Ref. 4]. One primary characteristic of the staring systems is that they introduce sampling in two dimensions. The spatial sampling process in a focal plane array is shown above in Figure 2.4. The outer rectangular frame represents the FPA in which the discrete detector elements are located. The detector elements are assumed to be rectangular because it is more convenient for analysis and it is the most common geometry encountered. The spatial sampling frequency depends on the distance between two adjacent detector-element centers, called the pixel "pitch". Therefore, spatial sampling period is calculated as:

$$\text{T} = \left(\frac{\Delta d}{f_{OPTICS}} \right)$$
(2.8)

14

where T is the sampling period in radians, Δd is the pixel pitch in meters and f_{OPTICS} is the focal length of the sensor optics in meters. The sampling frequency is defined as:

$$f_S = \left(\frac{1}{T}\right) \tag{2.9}$$

where f_s is the sampling frequency in samples (cycles) per radian. It is clear that the sampling frequency in the vertical direction is equal to the sampling frequency in the horizontal direction for square detector geometry.

The sampling theory requires that if the original image being sampled contains information with frequencies above half the sampling frequency, which is called the Nyquist frequency, the final image will contain spurious information after the reconstruction process. In this process, a frequency component, which is above the Nyquist limit in the original image, appears as a lower frequency component after sampling due to the phenomenon called "aliasing". The Nyquist frequency (f_N) is defined as:

$$f_N = \left(\frac{f_S}{2}\right) \tag{2.10}$$

The result of aliasing can be observed as distortions and degradation in the image produced.

One-dimensional frequency spectra of an original signal before and after sampling at differing sampling rates are given in Figure 2.5. The band-limited signal in Figure 2.5(a), which is also called the baseband, is the original signal before the sampling process. It is important to notice that sampling theory can only be applied to band-limited functions for an exact reconstruction process of the original functions.

The replication property of delta function suggests that sampling of a signal in the spatial domain corresponds to the replication of the band-limited original spectrum in the spatial frequency-domain. As a result of this concept, the sidebands represent the

replications of the original signal at frequencies Kf_s after being sampled, where K is an integer (K = 1,2,3…). If the sampling frequency were increased so that there would be no overlapping, the sampled image would be perfectly recovered. This phenomenon is called oversampling and is depicted in Figure 2.5(b). Oversampling does not necessarily mean that there is excessive sampling in the process.

Figure 2.5(c) shows the critical sampling case in which the sampling frequency is arranged so that the Nyquist frequency requirement is barely reached ($f_s = 2 f_h$). Only a perfect low-pass filter can recover the original input image by removing the sidebands.

If a frequency of the original signal is greater than the Nyquist frequency f_N which is the half of the sampling rate, the system is undersampled. The overlap of the baseband and the sidebands causes aliasing as in Figure 2.6 where $f_h = f_s = 2 f_N$. There would be an ambiguity within the overlapping frequency band because it would be impossible to know the origin of the reconstructed spectrum frequency components [Refs. 4 and 11].
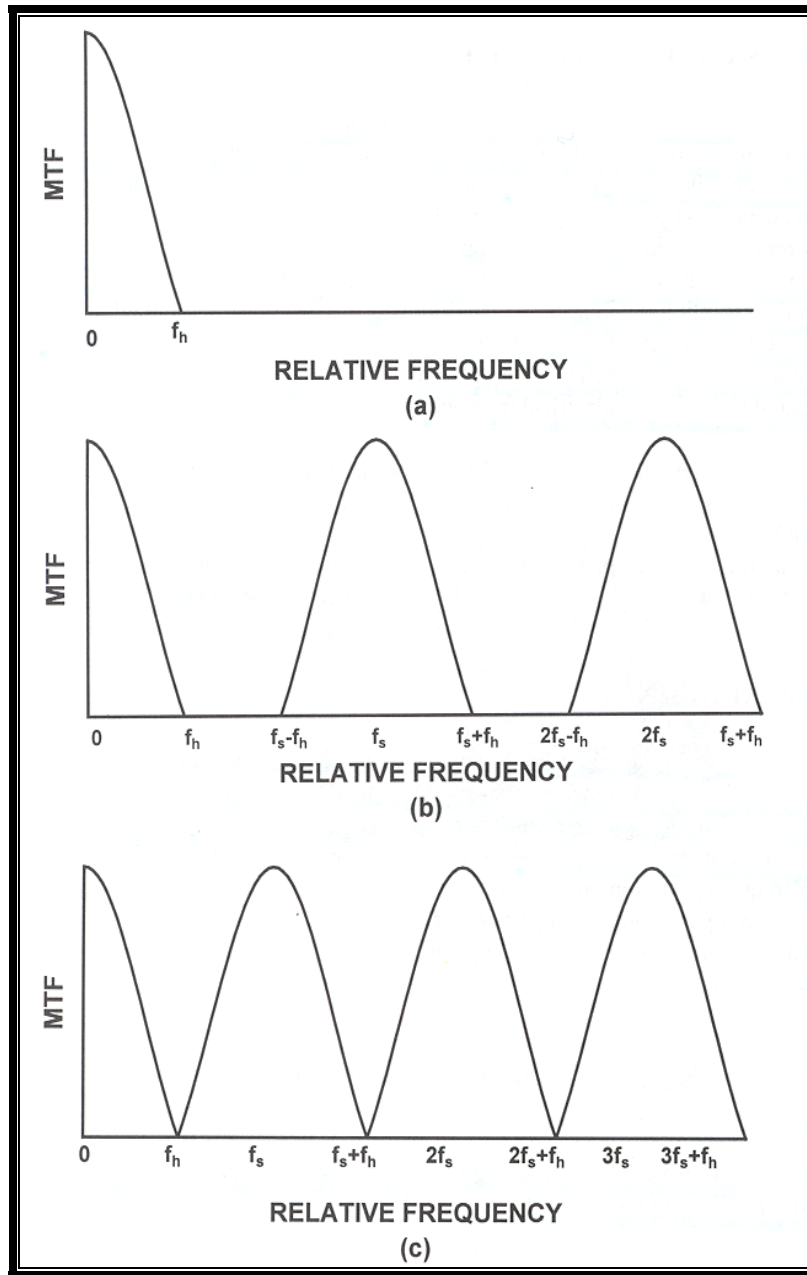
Figure 2.5.   Sampling Process at Different Sampling Frequencies (A) Original Band-Limited Signal (B) Frequency Spectrum after Sampling and (C) when ($f_s = 2 f_h$), the Bands Adjoin [Ref. 4].

17
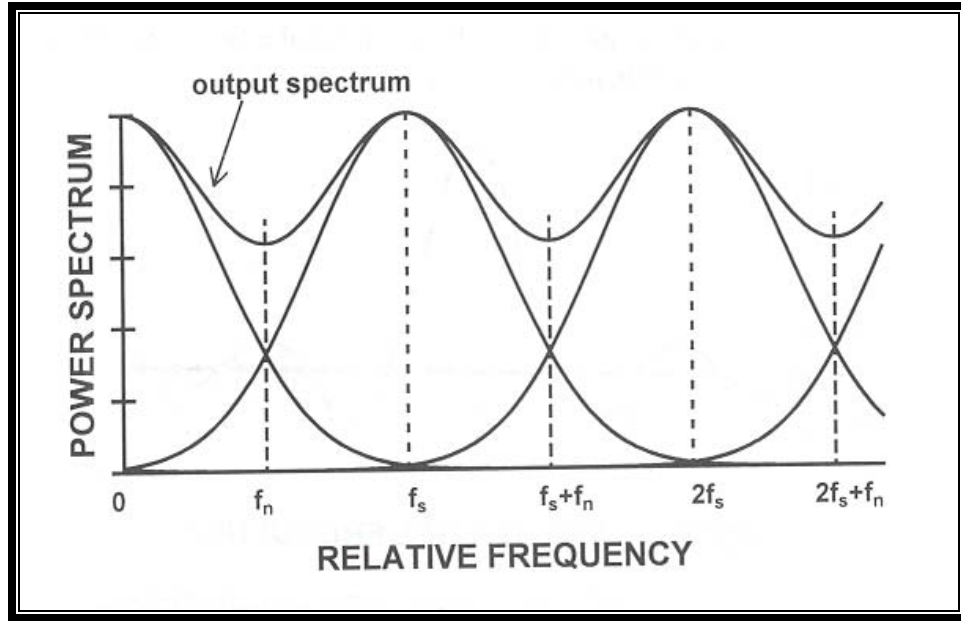
Figure 2.6.   The Overlap of the Baseband and the Sidebands Causes Distortion in the Output Spectrum due to Undersampling [Ref. 4].

Many methods have been suggested to reduce the aliasing effect in the final image. One of them suggests equating the pitch to the sampling period using a fill factor of 100% where fill factor is defined as the ratio of the FPA active area to the FPA total area. However, 100% fill factor in FPAs is inapplicable due to the fabrication technology limitations today. Another method suggests increasing the detector dimensions decreasing the spectral width, but that reduces the modulation of detectable spatial frequencies. Consequently, there seems to be a trade-off between system MTF and the aliasing phenomenon. An alternate way might be to increase the sampling rate. This can be accomplished either by increasing the number of detector elements in an array or by decreasing the field-of-view. Increasing the number of detector elements is difficult again due to the technological limitations, while decreasing the field-of-view approach might be undesirable.

The last but the most popular method being suggested, which is also in use today, is the micro-scanning process. This technique is a way of increasing the sampling rate by moving the image around on the detector array by fractions of a pixel size and

18

recording the successive images for each shift. The recorded images are then combined to produce a final image. Although the micro-scanning technique is applicable to today's thermal imagers, it brings the trade-off between aliasing or integration time together [Ref. 13].

F.   SYSTEM PERFORMANCE PARAMETERS

The following section describes the three basic parameters: Noise Equivalent Temperature Difference (NETD), Minimum Resolvable Temperature Difference (MRTD) and Minimum Detectable Temperature Difference (MDTD) that are used in the performance specifications of the thermal imaging systems.

1.   Noise Equivalent Temperature Difference (NETD)

NETD is an intermediate sensitivity parameter defined as the target-to-background differential temperature generating a peak signal to rms noise ratio of one while imaging relatively large targets [Ref. 14]. For system measurements, NETD is determined at the analog video or at the output of the monitor through a standard filter, which corresponds to the filtering performed by the electronics prior to the measurement point [Refs. 15 and 16]. Basically, NETD for a typical thermal imaging system is determined by the simple equation given below:

$$NETD = \left(\frac{\Delta T}{V_S / V_N} \right) \tag{2.11}$$

where ΔT represents the temperature difference between the target and the background. Notice that when the denominator value is set to one, NETD becomes equal to ΔT by definition.

For a scanning system, Shumaker [Ref. 14] defines NETD with the equation given below:

$$NETD = \frac{10(FOV_X FOV_Y F_R N_{OS} N_{SS})^{1/2}}{(\pi N_D \eta_{SC})^{1/2} D \Delta x \Delta y D^{**} \eta_{CS} (\partial N / \partial T) \tau_O} \tag{2.12}$$

where:

N_{os} is the over-scan ratio

N_{ss} is the serial scan ratio

N_D is the number of detectors

$\partial N/\partial T$ is the thermal gradient ("the derivative of Planck's equation" in watt cm^{-2} K^{-1} sr^{-1})

η_{sc} is the scan efficiency

η_{cs} is the cold-shield efficiency

D is the optics diameter (m)

D^{**} is the band averaged detector detectivity (cm Hz$^{\frac{1}{2}}$ W^{-1})

Δx is the in-scan detector angular subtense (mRad)

Δy is the cross-scan detector angular subtense (mRad)

FOV_x is the in-scan field-of-view (mRad)

FOV_y is the cross-scan field-of-view (mRad)

F_r is the frame rate (1/sec)

τ_O is the optical transmittance

With the growth of the thermal imaging technology, NETD has become a major performance predictor parameter. Its use simplified the formulations for the more comprehensive prediction parameters such as MRTD and MDTD. However, NETD does not include the temporal and spatial integration effects of the eye, and characterizes only the temporal detector noise, instead of accounting for overall system noise from various sources.

2. Minimum Resolvable Temperature Difference (MRT)

Minimum resolvable temperature difference (MRTD or MRT) is the primary summary measure of a thermal imaging system performance including resolution,

sensitivity, and the observer [Ref. 17]. It is defined as the temperature difference between a uniform background and the bars of a four-bar target, which makes the individual bars just resolvable through a thermal imager to a trained observer [Ref. 11]. Four-bar patterns are standardized by a 7:1 aspect ratio, which makes the overall pattern a square.

A typical MRT curve can be formed with respect to the relative sizes of the bar patterns as in Figure 2.7. Some of the substantial characteristics of MRT can be observed in this figure. First, MRT is not a single number; furthermore, it is a function of spatial frequency [Ref. 14]. Second, the temperature difference to resolve the four-bar chart increases as the bar dimensions decrease [Ref. 11]. The MRT curve ultimately shows an asymptotic characteristic at a spatial frequency around the 1/DAS value, which makes the TIS to be limited by the detector characteristics, since even very large temperature differences will not make the individual bars resolvable [Ref. 14]. DAS is the detector angular subtense, which describes the achievable sensor resolution relative to the detector dimension limitations. Dividing the detector dimension (width or height) by the optical focal length yields DAS in that dimension [Ref. 9]. A final aspect of MRT to be noticed is that it is not an objective measurement because it comprises the human eye-brain performance.
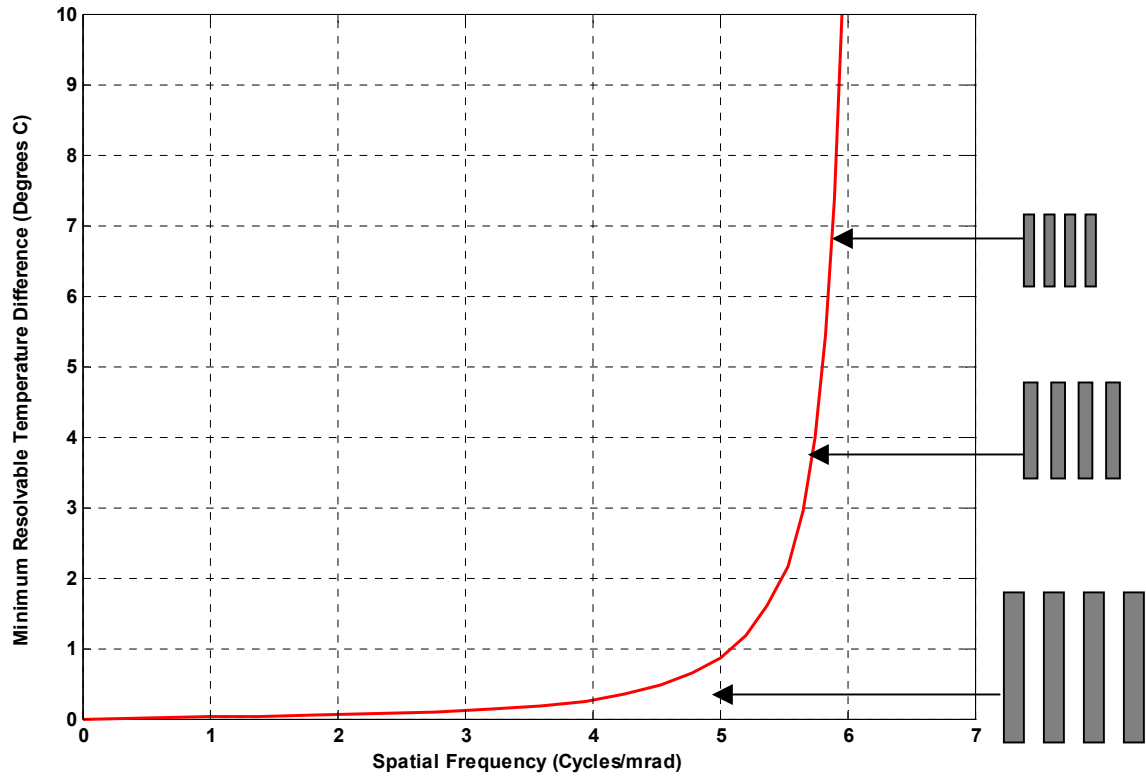
Figure 2.7.   A Typical MRT Plot [After Ref. 11].

Numerous equations with various modifications and approximations have been proposed for MRT prediction. One general form for a scanning system is given by Shumaker [Ref. 14] in the following formula:

$$MRT(v) = \frac{20 SNRT \left(FOV_x FOV_y v^2 \right)^{1/2} \rho_x^{1/2}}{\tau_0 DD^{**} \left(\pi N_D \eta_{sc} \right)^{1/2} \eta_{cs} \left(\Delta x \Delta y \right)^{1/2} MTF_S(v)(Lt_e)^{1/2} \partial N / \partial T} \qquad (2.13)$$

Where:

v is the spatial frequency (cycles/mRad)

t_e is the eye integration time (s)

$\partial N/\partial T$ is the thermal gradient ("the derivative of Planck's equation" in watt cm^{-2}
K^{-1} sr^{-1})

N$_D$ is the number of detectors

η_{sc} is the scan efficiency

η_{cs} is the cold-shield efficiency

FOV$_x$ is the in-scan field-of-view (mRad)

FOV$_y$ is the cross-scan field-of-view (mRad)

Δx is the in-scan detector angular subtense (mRad)

Δy is the cross-scan detector angular subtense (mRad)

MTF$_S$ is the overall system modulation transfer function

SNRT is the threshold signal-to-noise ratio

D   is the diameter of the optical aperture (m)

D**   is the band-average detector specific detectivity for 2π steradians (cm Hz$^{\frac{1}{2}}$
W^{-1})

τ_o is the optical transmittance

L   is the length-to-width aspect ratio of the target bar

ρ_x is the noise filter factor

3.   **Minimum Detectable Temperature Difference (MDT)**

Although the definition of the minimum detectable temperature difference
(MDTD or MDT) is almost the same as the definition of the MRT, the difference
between the two arises from the representation of the target. MDT is a function of target
size where the target is represented by an isolated square. Therefore, MDT is defined as

the differential temperature between the square target and a uniform background, which makes the square just detectable through a thermal imager to a trained observer [Ref. 14].

A representative MDT curve can be formed with respect to the relative sizes of the square targets as in Figure 2.8. Similarly, MDT is plotted as a function of spatial frequency, which can be calculated as the reciprocal of twice the angular subtense of the side of the square target [Ref. 14]. The plot shows that the required temperature difference to detect the square target increases as the target size decreases and the MDT curve does not show an asymptotic characteristic as the MRT curve does because even a point target can be made detectable by increasing its temperature.
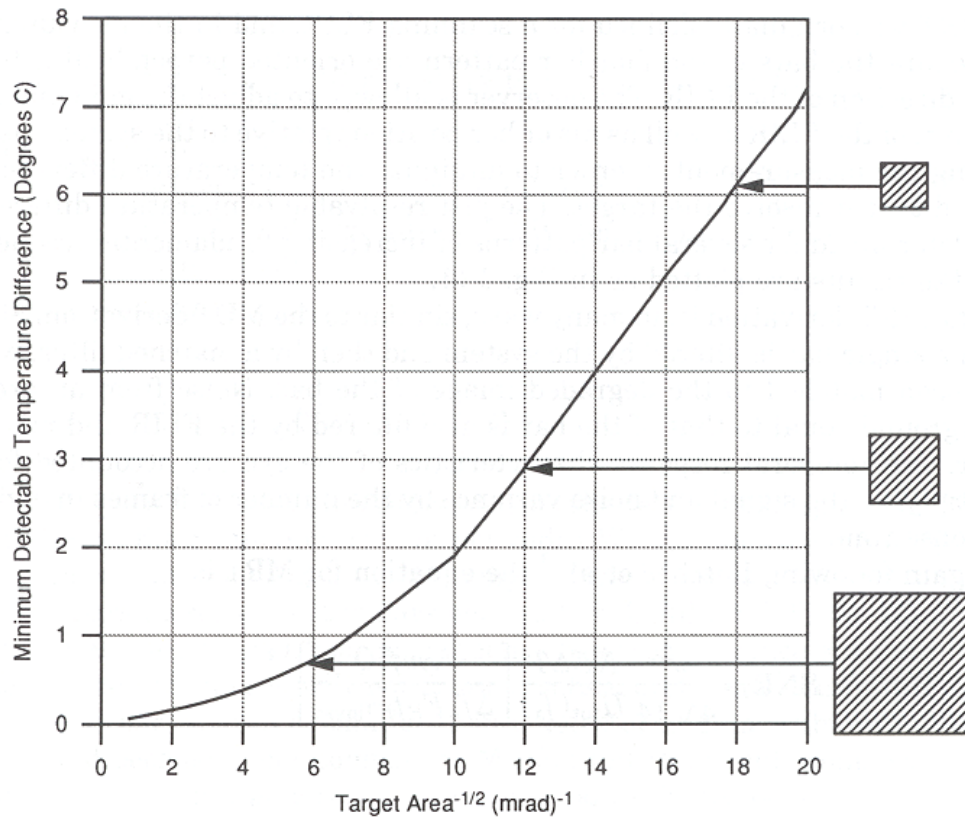
Figure 2.8.   A Typical MDT Plot [Ref. 11].

A commonly known equation for MDT is given by Shumaker [Ref. 14] as:

$$MDT(v) = \frac{20 SNRT \left(FOV_x FOV_y \Delta x \Delta y\right)^{1/2} \left(\Omega_T + r_S^2\right)}{\pi \tau_0 D \Delta x \Delta y D^{**} \, \partial N / \partial T \, \eta_{cs} \left(N_D \eta_{sc} t_e\right)^{1/2} \Omega_T \left(r_S^2 + r_B^2 + \Omega_T\right)^{1/2}}$$ (2.14)

where:

v is the spatial frequency (cycles/mRad)

t_e is the eye integration time (s)

$\partial N / \partial T$ is the thermal gradient ("the derivative of Planck's equation" in watt cm^{-2} K^{-1} sr^{-1})

N_D is the number of detectors

η_{sc} is the scan efficiency

η_{cs} is the cold-shield efficiency

FOV_x is the in-scan field-of-view (mRad)

FOV_y is the cross-scan field-of-view (mRad)

Δx is the in-scan detector angular subtense (mRad)

Δy is the cross-scan detector angular subtense (mRad)

r_S is the overall resolution of the imaging system (mRad)

r_B is the overall resolution of the back-end components including components from the detector electronics through the observer(mRad)

Ω_T is the solid angular subtense of the square target (mRad)^2

SNRT is the threshold signal-to-noise ratio

D   is the diameter of the optical aperture (m)

D**   is the band-average detector specific detectivity for 2π steradians (cm $Hz^{\frac{1}{2}}$ W^{-1})

τ_o is the optical transmittance

The equation above indicates a weaker dependence on the system MTF when compared to the MRT prediction characteristics. On the other hand, it is directly related to the detection capability of a noise-limited system, which makes MDT a measure of thermal system sensitivity. It differs from NETD in that the observer eye-brain performance is accounted for in MDT calculations [Ref. 11].

III. FLIR-92 TIS PERFORMANCE MODEL

The purpose of this chapter is to summarize the basic principles of the current standard FLIR-92 model that are relevant to the content of the proceeding chapters.

FLIR-92 is a computer-based model used as a system evaluation tool, which predicts standard summary performance measures for thermal imaging systems. It operates in the DOS environment and calculates the modulation transfer function (MTF), noise equivalent temperature difference (NETD), minimum resolvable temperature difference (MRTD) and minimum detectable temperature difference (MDTD) utilizing the primary sensor parameters. It has a principal function of predicting whether or not a system achieves the desired MTF, system noise, MRTD and MDTD determined necessary to perform mission-specific target discrimination and acquisition tasks [Ref. 2].

FLIR-92 can be used in modeling both scanning and staring thermal imagers that operate in mid-infrared (3-5 μm.) and far-infrared (8-12 μm.) spectral bands. However, it cannot be used for any type of electro-optical sensors other than thermal imagers (e.g. night vision devices). Furthermore, acquisition and discrimination range performance prediction is beyond the capabilities of FLIR-92 [Ref. 2].

The details of the model will be covered under three topics:

- Modulation Transfer Functions (MTFs)
- 3-D Noise Concept
- MRTD and MDTD Predictions

A. MODULATION TRANSFER FUNCTIONS (MTFS)

The FLIR-92 model assumes the thermal imaging system under evaluation to be linear to enable the use of linear system analysis in calculations. The evaluation process starts with recording the system parameters in the list of inputs, which will be used in the component MTF calculations. At this point the analyst has the flexibility of either using the built-in default system parameters or configuring them as desired [Ref. 2].

27

In FLIR-92, system component MTFs are grouped into three categories for modeling purposes: pre-filters, temporal post-filters and spatial post-filters. The MTF groups and their components are listed in Table 3.1 and the corresponding equations used in the calculations are presented in Appendix A. As a result of the linear system approach, FLIR-92 calculates the overall system transfer function by simply multiplying together the entire set of component MTFs.

Pre-filter MTFs	OPTICS MTFS	-Diffraction-limited MTF -Geometric Blur MTF
	Detector Spatial MTF	
	Focal Plane Array Integration MTF	
	Sample-scene Phase MTF	
	Image Motion MTFs	-Linear Image Motion MTF -Random Image Motion MTF -Sinusoidal Image Motion MTF
Temporal Post-filter MTFs	Detector Temporal MTF	
	Electronics Low Frequency Response	
	Electronics High Frequency Response	
	Boosting MTF	
Spatial Post-filter MTFs	Electro-optical Multiplexor MTF	
	Digital Filter MTF	
	Display MTF	-CRT Display MTF
	CCD Charge Transfer Efficiency MTF	
	Display Sample and Hold MTF	
	Eye MTF	-Non-limiting Eye MTF -Limiting Eye MTF

Table 3.1.   FLIR-92's Sub-system MTFs Grouped into Three Categories.

FLIR-92 gives the MTF results in two different forms. The short output lists the MTF results for only three main groups (pre-filters MTF, temporal post-filters MTF and spatial post-filters MTF), while the long output gives each single MTF calculation selected by the analyst under these groups.

B.   3-D NOISE CONCEPT

In the early models, the system noise was adequately quantified by a one-dimensional NETD value, which was assumed to be equal to the predominant detector noise for the first-generation thermal imagers. With the introduction of the advanced scanning and staring thermal imagers, temporal detector noise can no longer sufficiently characterize the system noise due to the use of focal plane array technology and the associated non-uniformity correction schemes, which are considered as complex noise sources for the sensors. Moreover, Time Delay and Integration (TDI), digital sampling and digital processing techniques, which were used to increase the signal-to-noise ratio (SNR), introduced additional noise terms to the system [Ref. 18].

It was observed that the noise patterns produced by these thermal imagers show direction dependent characteristics. In order to provide more accurate predictions, D'Agostino and Webb developed a new approach that takes the new noise components into consideration. Their methodology suggests dividing the total noise present at the output of the sensor into a group of seven direction dependent noise components, which simplifies the analysis, the understanding and also the incorporation of the noise terms into model formulations. Each noise component shows specific characteristics in each direction in a three-dimensional coordinate system that is shown in Figure 3.1 [Ref. 2].
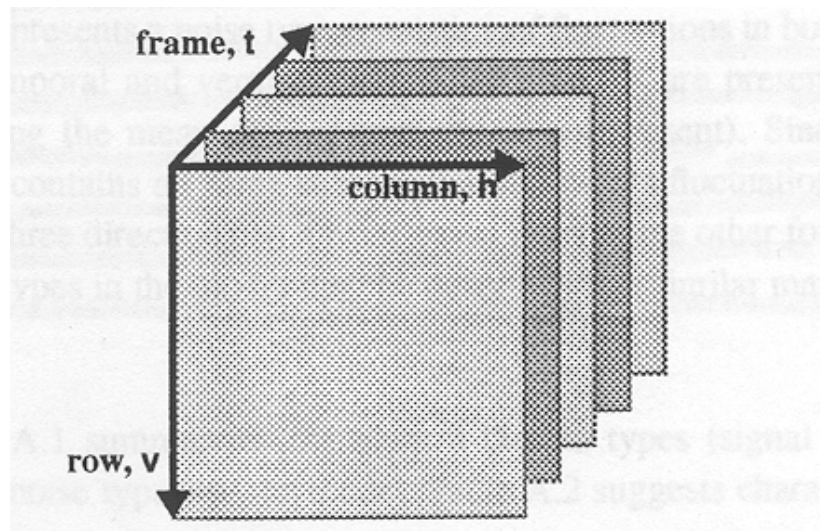
Figure 3.1.   Three-dimensional Coordinate System [Ref. 2].

29

The script t represents the temporal (time) dimension or sequential frames, while h represents the horizontal direction or the sequential columns within a frame and v represents the vertical direction or the sequential rows within a frame. The horizontal and vertical directions provide the spatial information in the original image. Depending on the type of the thermal imager, the horizontal direction may represent a spatial location in a staring sensor or time in a scanning system [Ref. 4].

Noise	Description	Source
σ_{TVH}	Random spatio-temporal noise	Basic detector temporal noise
σ_{TV}	Temporal row noise (i.e. line bounce)	Line processing, 1/f, readout
σ_{TH}	Temporal column noise (i.e. column bounce)	Scan effects
σ_{VH}	Random spatial noise (i.e. bi-directional fixed pattern noise	Pixel processing, detector-to-detector non-uniformity, 1/f
σ_{V}	Fixed row noise (i.e. line-to-line non-uniformity)	Detector-to-detector non-uniformity
σ_{H}	Fixed column noise (i.e. column -to- column non-uniformity)	Scan effects, detector-to-detector non-uniformity
σ_{T}	Frame-to-frame noise (i.e. frame bounce)	Frame processing
S	Mean of all noise components	

Table 3.2.   3-D Noise Component Descriptions [Ref. 2].

The components that define the overall noise are measured at the system output and they are finally converted to temperature (degrees C) in the same manner as done for NETD. The components, their descriptions and sources are as given in Table 3.2. The subscripts indicate the directions in which the noise fluctuations about a mean of zero occur. The missing subscripts indicate the directions in which the averaging operation is done. The averaging operation, which is done using the "D operator" within the coordinate system, enables the decomposition of the complex noise into its components. A detailed explanation of the D operator and its function is provided in Appendix B. Averaging complex noise in a specific direction yields the desired noise component present in the other directions in which no averaging operation is done. For example, σ_{TV}

represents the rms noise value that is present in the temporal and vertical directions calculated by averaging the complex noise in the horizontal direction [Refs. 2 and 9].

The noise components are assumed to be independent of each other. As a result of this the total system noise is defined as the root sum square of the noise components. This relation is shown in the following equation:

$$\Omega = (\sigma_{TVH}^2 + \sigma_{TV}^2 + \sigma_{TH}^2 + \sigma_{VH}^2 + \sigma_{V}^2 + \sigma_{H}^2 + \sigma_{T}^2)^{0.5} \tag{3.1}$$

where Ω represents the overall system noise.

All noise components may not be seen in every imaging system and depending on the specific system design one or more may dominate the others. They can be determined either from real system measurements or from estimates except for the random spatio-temporal noise component (σ_{TVH}). σ_{TVH} is the basic detector noise that is seen due to arriving photons (shot noise) and flowing current (Johnson noise). Therefore, it can be calculated in a similar fashion to that used in the first generation systems and can be related to the NETD value as seen in the following equation.

$$\sigma_{TVH} = NETD \times \frac{\sqrt{\Delta f_P}}{\sqrt{\Delta f_N}} \tag{3.2}$$

where Δf_N is the equivalent noise bandwidth for NETD calculation and Δf_P is the actual system noise bandwidth associated with the electronics prior to the display [Ref. 2]. It is obvious from the equation above that FLIR-92 calculates σ_{TVH} using the actual system bandwidth rather than using an artificial reference bandwidth as done for NETD.

The rest of the noise components other than σ_{TVH} can be classified into two groups. Random spatial noise or so-called fixed pattern noise (σ_{VH}), fixed row noise (σ_V) and fixed column noise (σ_H) are all time independent noise components [Ref. 19]. They occur due to the detector and electronics non-uniform responses over the focal plane array that might originate from the detector material variations, impurities or

31

imperfections, electrical circuit tolerances, and so on [Ref. 9]. The time dependent noise components, which can be listed as frame-to-frame noise (σ_T), temporal row noise (σ_{TV}) and temporal column noise (σ_{TH}) are mostly seen in scanning imaging systems. σ_T is assumed negligible so that it is not included in the model predictions [Ref. 19]. The global average, the mean of all noise, is denoted by the symbol S.

As mentioned previously the observer is one of the system components in FLIR-92 predictions. To incorporate the observer's eye-brain effects, FLIR-92 uses a "synchronous integrator model" for MRTD predictions while it uses the "matched filter model" for the MDTD predictions. The eye-brain effects are included into the three-dimensional noise methodology using the eye-brain integration factors E_T, E_H, E_V, which describe the temporal integration, horizontal integration and vertical integration respectively [Ref. 4]. The integration factors are effective only when the integration direction and the noise component direction coincide. As a consequence of this approach the total system noise term can be modified as the root sum square of the components as in Equation 3.3.

$$\Omega\left(f_S\right) = (\sigma^2{}_{TVH}E_T E_{V_Z}(f_S)E_{H_Z}(f_S) + \sigma^2{}_{VH}E_{V_Z}(f_S)E_{H_Z}(f_S) + \sigma^2{}_{TH}E_T E_{H_Z}(f_S) +$$
$$\sigma^2{}_{TV}E_T E_{V_Z}(f_S) + \sigma^2{}_{V}E_T E_{V_Z}(f_S) + \sigma^2{}_{H}E_{H_Z}(f_S))^{\frac{1}{2}} \qquad (3.3)$$

Note that the σ_T component has been neglected in the equation above [Ref. 2].

C.   MRTD AND MDTD PREDICTIONS

FLIR-92 uses different eye-brain models for the predictions of MRTD and MDTD as mentioned in the previous section. For predicting MRTD it uses the synchronous integrator model, which assumes the eye-brain components to be a spatially integrating system over the image, while ignoring blurring effects caused by the finite sized sensor apertures. On the other hand, for the prediction of MDTD it uses the matched filter model, which relates the eye-brain effects to a matched filter resulting in the increase of SNR ratio. Both models yield the same results for the periodic targets such

as four-bar pattern. Due to the simplicity of integrating the algorithm into FLIR-92, the synchronous integrator model is preferred for the MRTD calculations [Ref. 2].

Once all noise components are determined either by measurement or calculation, the components in the horizontal direction are integrated into the horizontal MRTD equation while the components in the vertical direction are integrated into the vertical MRTD equation in the same way. Including the noise effects degrades the overall system performance. A general interpretation of the MRTD, which clearly shows the inclusion of the correction factor into the MRTD prediction, is presented in the equation below.

$$MRTD_z(f_s) = \left(\frac{\left(\frac{\pi^2}{8} SNR_{TH} \sigma_{TVH} k_z(f_s) \right)}{MTF_{SYS_z}(f_s)} \right) \left[E_T E_{V_z}(f_s) E_{H_z}(f_s) \right]^{1/2} \qquad (3.4)$$

The subscript z in the equation refers to the direction of interest either horizontal or vertical. The other parameters and their descriptions are given in Table 3.3.

PARAMETERS	DESCRIPTION
SNR_{THR}	Threshold signal-to-noise ratio
σ_{TVH}	Random spatio-temporal noise
k_Z	Noise correction function
MTF_{SYS}	Overall system modulation transfer function
E_T	Eye temporal integration factor
$E_{Hz}(f_S)$	Eye horizontal integration factor in the direction of interest
$E_{Vz}(f_S)$	Eye vertical integration factor in the direction of interest

Table 3.3.   MRTD Equation Parameters [Ref. 2].

In the equation above, σ_{TVH} (the random detector noise or spatio-temporal noise) is the only term that has units (degrees Celsius). The rest of the terms, which are

dimensionless, are functions of spatial frequency. The U.S. Army Night Vision and Electronic Sensors Directorate (NVESD) recommends a value of 2.5 for the threshold SNR and a value of 0.1 seconds for the eye integration time E_T as reasonable averages for those quantities [Ref. 2].

The σ_{TVH} noise term, which is sometimes approximated with NETD, is generally given by:

$$\sigma_{TVH} = \frac{4 f_{NO}^2 \sqrt{\Delta f_P}}{\pi \tau_O \sqrt{A_D} \left(\int\limits_{\lambda 1}^{\lambda 2} D^*(\lambda, 300) \frac{\delta W}{\delta T_{300}}(\lambda) d\lambda \right)} \qquad (3.5)$$

where:

f_{NO} is the optical f-number

Δf_P is the system noise bandwidth

τ_O is the optical transmittance

A_D is the detector area

$D^*(\lambda, 300)$ is the detector noise-limited spectral detectivity

$(\delta W / \delta T)$ is the thermal derivative of Planck's Law [Ref. 2]

The noise correction function for the horizontal direction is given as:

$$k_H(f_s) = \left(1 + \frac{\sigma_{VH}^2}{\sigma_{TVH}^2} \frac{1}{E_T} + \frac{\sigma_{TH}^2}{\sigma_{TVH}^2} \frac{1}{E_{V_H}(f_s)} + \frac{\sigma_H^2}{\sigma_{TVH}^2} \frac{1}{E_T E_{V_H}(f_s)} \right)^{1/2} \qquad (3.6)$$

The correction function for the vertical direction is given as:

$$k_V(f_s) = \left(1 + \frac{\sigma_{VH}^2}{\sigma_{TVH}^2} \frac{1}{E_T} + \frac{\sigma_{TV}^2}{\sigma_{TVH}^2} \frac{1}{E_{H_V}(f_s)} + \frac{\sigma_V^2}{\sigma_{TVH}^2} \frac{1}{E_T E_{H_V}(f_s)} \right)^{1/2} \qquad (3.7)$$

It is important to note that the eye-brain integration factors and the noise components in one direction can only modify the correction function in that direction. The eye-brain integration factors are calculated differently for staring and scanning systems except for the time integration factor, which is given in the equation below.

$$E_T = \frac{\alpha_T}{F_R \tau_E} \tag{3.8}$$

where:

α_T is the temporal correlation factor

F_R is the system frame rate (Hz)

τ_E is the eye integration time (s).

The spatial integration factors for staring and scanning systems are calculated as in the equations given in Appendix C.
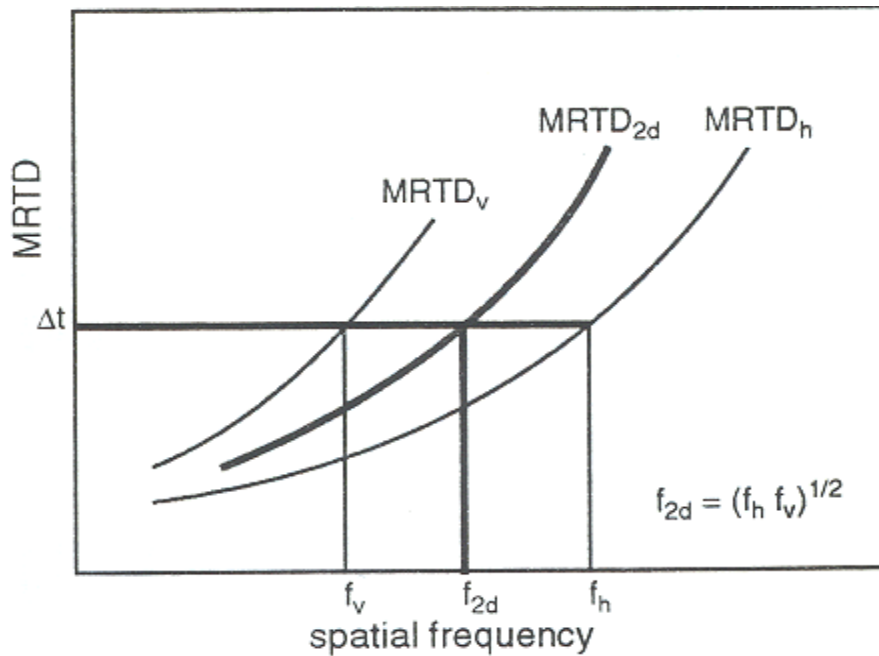
Figure 3.2.   **A Typical 2-D MRTD Plot.**

35

The FLIR-92 model calculates the horizontal and the vertical MRTD values for a subset of spatial frequencies. Furthermore, the model calculates the two-dimensional MRTD values and their corresponding spatial frequencies from the geometric mean of the horizontal and vertical MRTD spatial frequency values as presented in Figure 3.2. Since each MRTD component is weighted with respect to its frequency axis, the $MRTD_{2d}$ curve asymptotes to the geometric mean value of the horizontal and vertical spatial cutoff frequencies as seen in the figure below.

The FLIR-92 model predicts MDTD using Equation 3.9, which is very similar to the MRTD equation.

$$MDTD\ (f_s) = \left(\frac{SNR_{TH}\ \sigma_{TVH}\ k_{MDT}\ (f_s)}{A_T Q_H (f_s) Q_V (f_s)} \right) (E_T E_H (f_s) E_V (f_s))^{1/2} \quad (3.9)$$

f_s is the spatial frequency in units of mrad^{-1} where A_T is the target area. The overall system MTFs in the horizontal direction and in the vertical direction are embedded in the quantities $Q_H(f_s)$ and $Q_V(f_s)$ respectively.

$Q_H(f_s)$ is calculated as:

$$Q_H(f_s) = \int_{-\alpha}^{\alpha} H^2_{SYS_H}(v) \left(\frac{\sin\left(\pi v \dfrac{1}{f_s} \right)}{\pi v \dfrac{1}{f_s}} \right)^2 dv \quad (3.10)$$

$Q_V(f_s)$ is calculated as:

$$Q_V(f_s) = \int_{-\alpha}^{\alpha} H^2_{SYS_V}(v) \left(\frac{\sin\left(\pi v \dfrac{1}{f_s} \right)}{\pi v \dfrac{1}{f_s}} \right)^2 dv \quad (3.11)$$

In the two equations given above, H_{SYS} represents the overall system MTF in the given direction and the sinc term $((\sin X)/X)$ in the brackets represents the Fourier Transform of the square target by definition. For both staring and scanning systems, the same equations are used in MDTD predictions [Ref. 2]. The other terms in the MDTD formula are calculated using the same equations as defined in the MRTD case except for the correction function $k_{MDT}(f_S)$ given in Equation 3.12.

$$k_{MDT}(f_S) = \left(1 + \frac{\sigma^2_{VH}}{\sigma^2_{TVH}E_T} + \frac{\sigma^2_{TH}}{\sigma^2_{TVH}E_V(f_S)} + \frac{\sigma^2_H}{\sigma^2_{TVH}E_T E_V(f_S)} + \frac{\sigma^2_{TV}}{\sigma^2_{TVH}E_H(f_S)} + \frac{\sigma^2_V}{\sigma^2_{TVH}E_T E_H(f_S)}\right)^{1/2}$$

(3.12)

THIS PAGE INTENTIONALLY LEFT BLANK

IV. THE VISIBILITY MODEL

The main purpose of this chapter is to overview the basic principles of the Visibility concept, which was proposed by R.J.Pieper and A.W.Cooper of the Naval Postgraduate School in 1994. This chapter will also serve as an introduction to the Virtual Thermal Image-Processing model that will be presented in Chapter VI because the Virtual Thermal Image-Processing model is based on the Visibility model. A short review of the latest modifications in the Visibility model is included here because these amendments are also utilized in constructing the Virtual Thermal Image-Processing model. The chapter will close with the presentation of the objective MRTD predicting version of the Visibility model.

A. THE VISIBILITY CONCEPT

Several models have been proposed for predicting the performance of staring thermal imaging systems. Among these, the infrared community standard model FLIR-92 has gained a wider acceptance. As mentioned in Chapter III, the FLIR-92 model predicts MRTD below the Nyquist limit and does not take into account the aliasing effects. It also makes a set of assumptions regarding the observer eye-brain recognition process, which brings some limitations to the performance predictions. Therefore the FLIR-92 predictions were observed to be overly optimistic at low spatial frequencies and overly pessimistic at high spatial frequencies [Ref. 17].

The Visibility model, which was based on a minimum threshold input contrast parameter and a contrast reduction factor due to aliasing and blurring effects, was proposed for predicting the MRTD performance of staring systems. The model makes no assumptions about the observer's judgment in the recognition process. Therefore it can easily be used for the performance predictions of a thermal imaging system utilizing an Automatic Target Recognizer (ATR) device instead of a human observer, which makes the Visibility model more adaptable to the goal of modeling an objective MRTD prediction [Ref. 3]. The details of the objective MRTD measurement procedure will be discussed later in Chapter V.

The Visibility model suggests the incorporation of a low frequency limit into the MRTD calculations in the form of

$$MRTD(f_z) = MRTD(f_z \rightarrow 0) x \frac{1}{\alpha(f_z)}$$ (4.1)

where subscript z indicates either the horizontal or the vertical direction, f_z is the spatial frequency and $\alpha(f_z)$ is the contrast transference parameter. Equation 4.1 has a significant physical appeal because it is based on the fact that to resolve a target with an input contrast of zero is not possible. This is why the laboratory-based MRTD measurements extend to a certain non-zero limit at low spatial frequencies [Refs. 3 and 20].

Depending on this simple but important physical reality, a threshold contrast value of ΔT_{SC} is defined at the low frequency limit below which recognition is not possible. ΔT_{SC} is an observer and system dependent term that inherently comprises all noise effects without making any assumptions about their natures. For that reason an observer may have different thresholds for various thermal imaging systems [Refs. 3, 19 and 20].

The block diagram in Figure 4.1 shows the fundamental processes taken into account in the model. First a four-bar target with a high contrast ΔT is modeled as a rectangular function, which is considered as the input to the system. During the image formation the input experiences contrast degradation due to blurring effects at the optics while aliasing effects due to the sampling process are introduced in two dimensions at the detector plane. Scene phasing effects, which are observed due to the target misalignment from the center of the detector elements, are also taken into account throughout the sampling process. Next the model utilizes the electronics OTF which brings a non-zero PTF into the predictions before the introduction of the display MTF into the image reconstruction process.
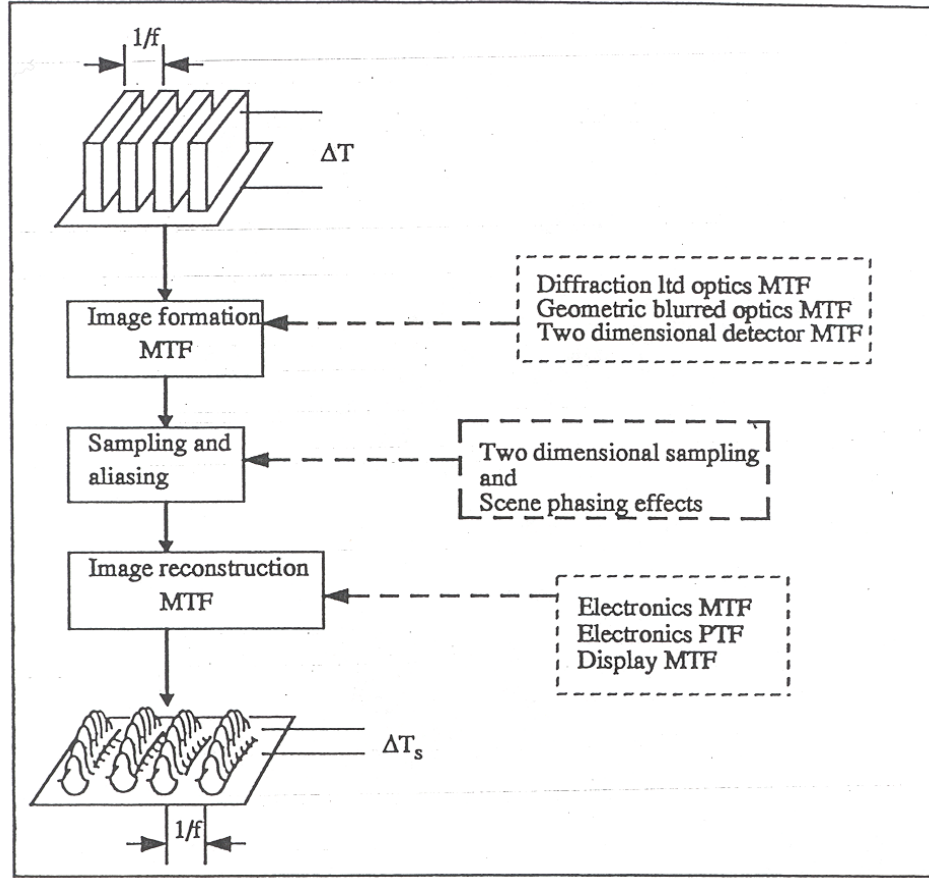
Figure 4.1.   The Visibility Model block diagram [Ref. 3].

Finally, the rectangular input function with a high contrast ΔT appears as a smoothed-out image with a degraded contrast of ΔT_S at the display [Ref. 3]. Related to the parameters shown in Figure 4.1, the contrast transference parameter for a particular bar spatial frequency is given as in Equation 4.2.

$$\alpha(f) = \frac{\Delta T_S(f)}{\Delta T} \tag{4.2}$$

Depending on the physical reasoning of the Visibility model, the relationship between the contrast transference parameter and MRTD value is constructed by the following equation.

41

$$MRTD(f) = \frac{\Delta T_{SC}}{\alpha(f)} \tag{4.3}$$

B.   THE CALCULATION OF THE THRESHOLD INPUT CONTRAST PARAMETER ΔTSC

The input contrast threshold parameter ΔT_{SC} in Equation 4.3 can be determined in two ways. It can be obtained from the laboratory measurements or it can be calculated from the system parameters using the following heuristic formulation [Ref. 19].

$$\Delta T_{SC} = \frac{\pi^2}{8} SNR_{THR} \sigma_{TVH} \left(1 + \frac{\sigma^2_{VH}}{\sigma^2_{TVH}}\right)^{0.5} (E_T)^{0.5} \tag{4.4}$$

where

SNR$_{THR}$ is the threshold signal-to-noise ratio

E$_T$ is the temporal integration factor of the eye

σ_{TVH} is the random temporal pixel noise

σ_{VH} is the random spatial noise

Equation 4.4 apparently shows that ΔT_{SC} calculations incorporate the 3-D noise concept. Only temporal pixel noise (σ_{TVH}) and spatial noise (σ_{VH}) are included in the analysis since they are the dominant noise components in staring systems, which can be determined from measurements. If measurement data is not available σ_{TVH} can be calculated using Equation 3.2 and σ_{VH} can be estimated from its default value that was determined to be $0.40\sigma_{TVH}$ as in the FLIR-92 model [Ref. 19].

The eye temporal integration factor is also included as an enhancement element into Equation 4.4 since the observer is considered as a part of the system. Therefore this formula provides a subjective prediction for the threshold contrast parameter ΔT_{SC}.

C.   THE   CALCULATION   OF   THE   CONTRAST   TRANSFERENCE PARAMETER α(F)

The contrast transference parameter α(f) brings all frequency dependent system components characterized in terms of the sub-system MTFs into the MRTD predictions. It also accounts for the two-dimensional sampling and aliasing effects that are inherent in the staring thermal imagers [Ref. 19].

For the calculation of the contrast transference parameter, an averaging process is applied to the portions of the output image corresponding to the center of the leftmost bar and to the center of the leftmost trough lying in between the two bars. The difference between the average obtained from the bar represented by T_P and the average obtained from the trough represented by T_T yields a unaliased output contrast value as shown in Figure 4.2. On the other hand a set of alias-noise values is calculated by subtracting the aliased output image from the unaliased one point by point. Then the standard deviation of the alias-noise values is taken to be the alias-noise parameter denoted by σ_{ALIAS}. Finally the output contrast is determined by subtracting the alias-noise parameter σ_{ALIAS} from the unaliased contrast value that is given by Equation 4.5 [Ref. 19].

$$\Delta T_S(f) = T_P(f) - T_T(f) - \sigma_{ALIAS}(f)$$

(4.5)

As the input contrast is set to one for all spatial frequencies, the contrast transference parameter is calculated as

$$\alpha(f) = \Delta T_S(f)$$

(4.6)

When this process is repeated over the range of all spatial frequencies, the contrast transference parameter is obtained as a function of spatial frequency. The results obtained in the previous works [Refs. 3 and 20] indicated that the Visibility model predictions were reasonably accurate. Therefore the model was confirmed to be a simple

but precise means of predicting the performance of thermal imaging sensors [Ref. 3]. This is the most significant reason why the Virtual Thermal Image-Processing model is based on the Visibility model.
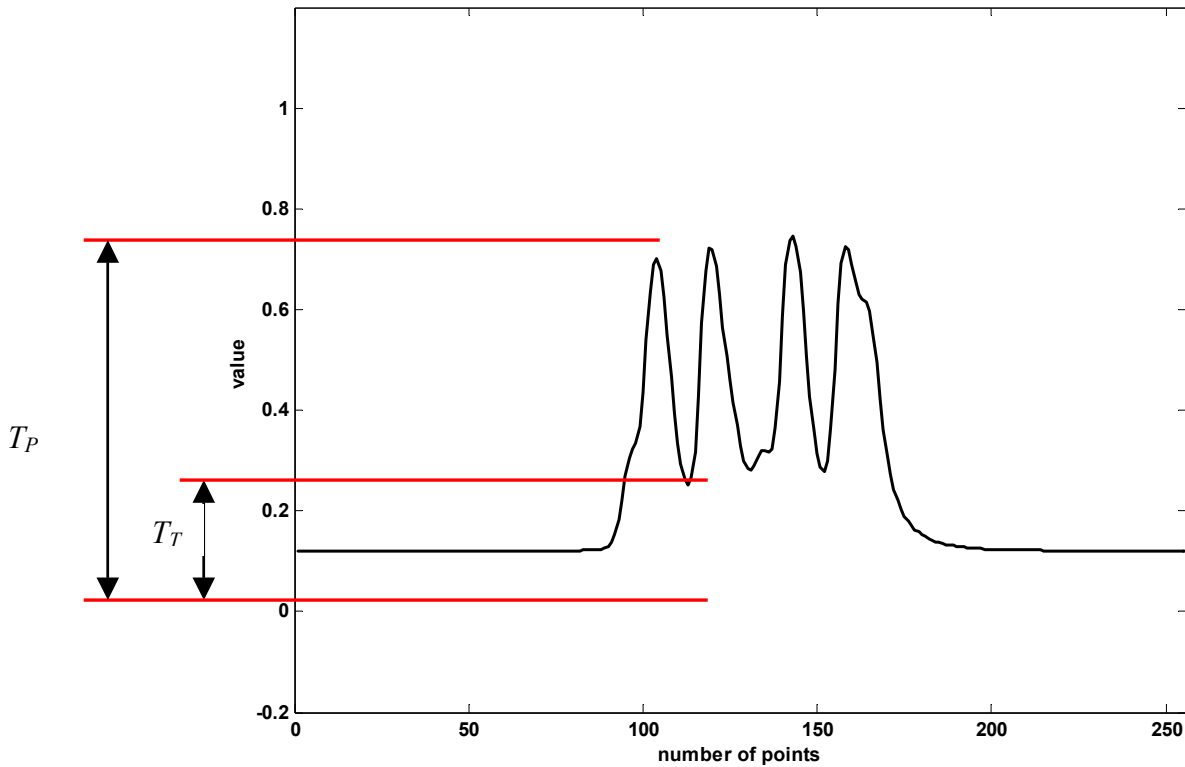
Figure 4.2. **A Typical Contrast Calculation Shown on a Profile Across the Horizontal Bar Pattern Image Generated at 0.65 Cycles/Mrad.**

D. THE LATEST AMENDMENTS IN THE VISIBILITY MODEL

The Visibility model has been modified to enable a more precise modeling of the thermal imaging systems without changing any of the primary concepts of its origin. Basically, the modifications can be discussed under two main headings: the modifications concerning the calculation of the threshold contrast parameter ΔT_{SC} and the modifications concerning the contrast transference parameter $\alpha(f)$.

1. Modifications concerning the Calculation of ΔTsc

For the calculation of the threshold contrast parameter ΔT_{SC}, a correction is proposed to Equation 4.4. According to the 3-D noise concept in FLIR-92, the eye temporal integration factor E_T should only enhance the random temporal pixel noise component σ_{TVH} that has noise in the temporal direction. Therefore E_T should not impact the random spatial noise (fixed pattern noise) component σ_{VH} as it does in Equation 4.4. The proposed formulation for the calculation of ΔT_{SC} is given below in Equation 4.7.

$$\Delta T_{SC} = \frac{\pi^2}{8} SNR_{THR} \left(\sigma^2_{TVH} E_T + \sigma^2_{VH} \right)^{0.5} \tag{4.7}$$

Another modification affecting ΔT_{SC} is made in calculating the system total bandwidth Δf_P used in the determination of the noise component σ_{TVH}. The relationship between σ_{TVH} and Δf_P was given as in Equation 3.2. In the original model, Δf_P was calculated using only the reconstruction MTF. The amendment suggests including the eye MTF into the Δf_P calculation, which will also be discussed under the noise analysis topic of the Virtual Thermal Image-Processing model in Chapter VI.

2. Modifications concerning the Calculation of α(F)

For the calculation of the contrast transference parameter $\alpha(f)$, a new method has been developed in which $\alpha(f)$ is computed directly from the output image. Instead of an averaging process, the maximum values on each bar and minimum values on each space are computed first. Then, contrast values are calculated by subtracting the minimum from the maximum for each adjacent bar and space in the image. Finally, the minimum contrast value among the successive contrast values in the image is named to be the contrast transference value for that specific bar spatial frequency. When this process is repeated over the range of all spatial frequencies, the contrast transference parameter is obtained as a function of spatial frequency.

Further changes affecting the contrast transference parameter were made in the calculation of the sub-system MTFs. First, the methodology of obtaining electronics OTF was modified. In the original model, it was calculated from the electronics MTF and

electronics PTF equations directly. The new approach suggests obtaining the electronics OTF by simply taking the 2-D FFT of its impulse response function for a more accurate calculation. Second, an additional detector MTF was included into the image reconstruction process as treated by Lloyd in Reference 10. The details for the image formation and image reconstruction are provided in Chapter 6.

All transfer function equations used in the Visibility model predictions will be given in Chapter VI since the Virtual Thermal Image-Processing model utilizes the same sub-system transfer functions. Further details of the revisions accomplished in the Visibility model can be found in Reference 21.

E. THE OBJECTIVE MRTD PREDICTIONS OF THE VISIBILITY MODEL

Up to this point in the discussions concerning the MRTD predictions, the human observer was considered as a part of the experimental process, which makes this type of assessment subjective and less accurate because the results depend on the performance of the person making the measurement. Although experienced observers tend to produce repeatable results, it would be preferred to make these measurements such that the results are independent of the observer [Ref. 22].

With this motivation, a new Visibility model is constructed for predicting the objective MRTD performance of thermal imaging systems taking into account the enhancements performed in the Visibility model that makes subjective MRTD predictions. In contrast to the subjective model, the objective model takes the human observer and the display out of the loop and calculates the threshold contrast parameter ΔT_{SC} using the simpler Equation 4.8.

$$\Delta T_{SC} = SNR_{THR} \frac{\Delta T}{\Delta V} N_V \tag{4.8}$$

In Equation 4.8,

SNR_{THR} is the threshold signal-to-noise ratio for a system to resolve a target

46

ΔT is the temperature difference between the target and the background

ΔV is the differential signal voltage produced by the thermal imaging system due to the temperature difference of ΔT between the target and the background

N_V is the noise voltage

Equation 4.8 is based on the assumption that a differential temperature between the target and the background would produce a relative differential voltage at the sensor, which makes the $(\Delta T/\Delta V)$ ratio approximately a constant. The data obtained from the objective MRTD measurements performed in a laboratory environment also support this theory strongly. Another significant feature of Equation 4.8 is that a SNR_{THR} parameter is integrated into the predictions because an increase in the SNR_{THR} requirement for a system to resolve a target suggests an increase in the system ΔT_{SC} value, which makes Equation 4.8 applicable for different system SNR_{THR} requirements.

Further details of the Visibility model that makes objective MRTD predictions can be found in Reference 21. Both subjective and objective MRTD predictions of the Visibility model will be compared to the laboratory measurements in Chapter V.

THIS PAGE INTENTIONALLY LEFT BLANK

V. SUBJECTIVE AND OBJECTIVE MRTD MEASUREMENTS AND THE COMPARATIVE ANALYSIS OF THE DATA

The purpose of this chapter is to explain the experimental setup and the methodology used in both subjective and objective MRTD measurements made in our laboratory at the Naval Postgraduate School and to present the results. Ultimately, these results will also be compared with the recently modified Visibility model and the FLIR-92 model predictions in this chapter.

A. THE SUBJECTIVE MRTD MEASUREMENTS

1. Experimental Setup

A staring thermal imaging device, the Mitsubishi Electronics IR-M500 model, utilizing a 512x512 PtSi detector array was used in the subjective MRTD measurements. The imager's system parameters are given in Appendix D.

The experimental equipment was arranged as shown in Figure 5.1. Composed of a front plate and a heated back plate, a target platform was placed at a distance of R from the thermal imager. Figure 5.2 shows the details of this platform. For a proper alignment, the imager optical aperture and the target front plate were placed parallel to each other at the same height. Therefore the effects of scene phasing phenomenon were minimized and a clean image was presented to the observer.

Both plates on the target platform were made of shot-blasted aluminum to provide high thermal conductivity and temperature uniformity on the surfaces visible to the thermal imager and they were painted in a non-reflective flat black to ensure uniform emissivity. The temperature of the back plate was adjusted by controlling the electrical current provided to the resistive heating elements placed on its back surface. On the other hand the front plate remained near its ambient temperature since it was separated by 10cm from the back plate. A thermocouple mounted on each plate enabled the temperature difference between the target and the background to be read directly.
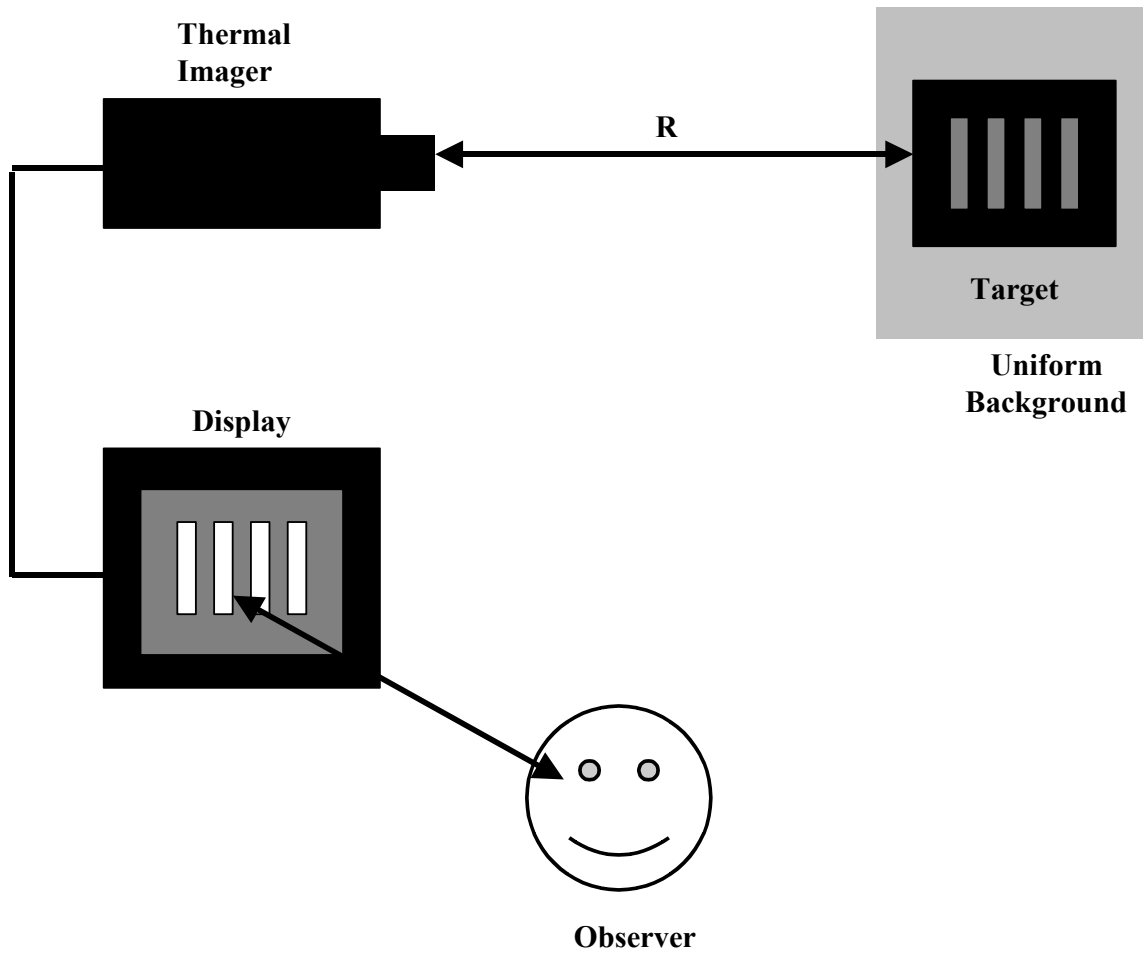
Figure 5.1.   The Experimental Setup.

As seen in Figure 5.2, standard four-bar patterns (7:1 aspect ratio) with various sizes were cut through the front plates allowing the observer to make measurements at different spatial frequencies. Once one of these front plates was slid over the fixed template in front of the back plate, the thermal imager viewed the heated back plate through the openings on the front plate. With this configuration, the front plate represented the uniform background while the back plate represented the hot target in the scene of interest.
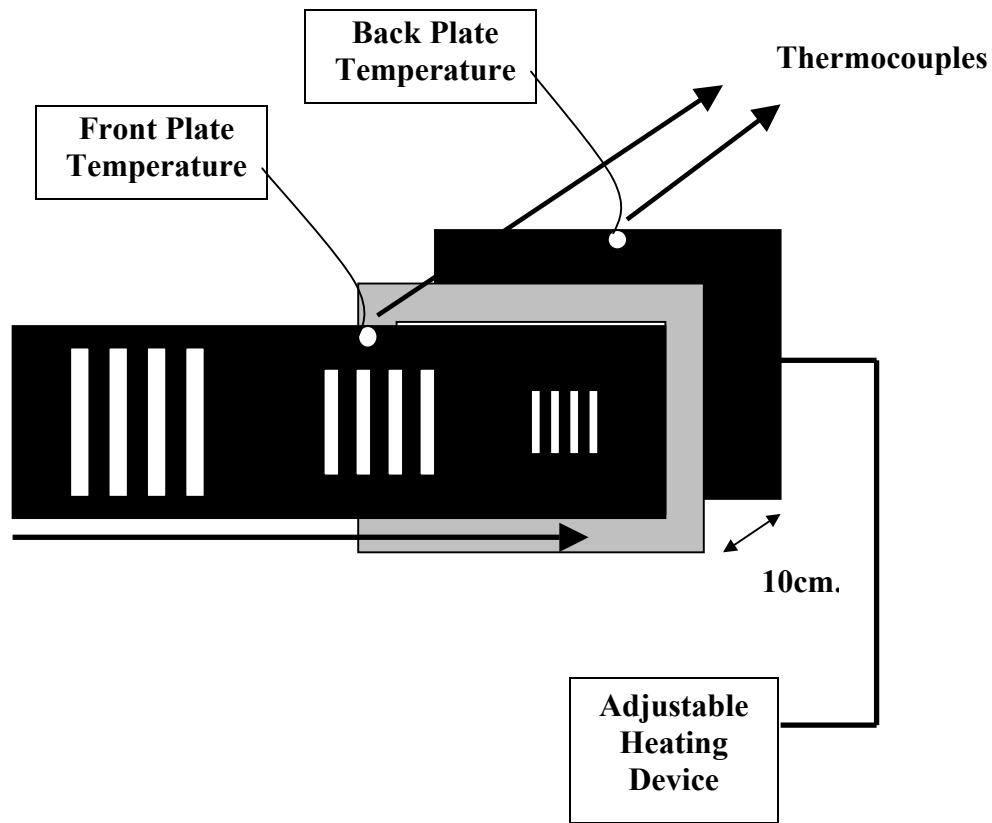
Figure 5.2.   The Target Platform.

The measurements were conducted at an ambient room temperature of 300 degrees Kelvin. The laboratory environment was organized so that the reflected radiation from other emitting objects in the laboratory environment was minimized. Since the experimental equipment was static, the motion effects of the thermal imager and the target were not accounted for, which is consistent with the static nature of most of the laboratory performance measurements in the literature.

2.   Experimental Methodology

Some preparations were made before the actual measurements. The observers were trained first for the recognition criteria. The target was called 'resolved' whenever all observers fully agreed that it consisted of four bars. Therefore the MRTD measurement process was based on a probability of 100% detection, which corresponds

to a SNR of about 6.0 [Ref. 25]. Other measurement methodologies utilizing various detection probabilities suggest different SNR values. As a result adjusting the SNR makes it easy to incorporate various measurement methodologies in the model predictions.

Then the thermal imager was focused and aligned with the target platform to optimize the system response. After darkening the laboratory, the observers were allowed sufficient time to adapt to the environmental conditions and to adjust the system gain and monitor contrast and brightness to enhance the viewing conditions.

Two sets of measurement data were taken during the experiment. One set was taken while the back plate was heated up. The observers waited until they could resolve the four bars. Then the second set of data was taken while the back plate was left to cool down. The observers waited until they could no longer resolve the four bars. In both measurements, the temperature difference between the front plate and the back plate was recorded as the MRTD. These steps were repeated for a range of spatial frequencies. Finally one set of MRTD as a function of spatial frequency was calculated by averaging these data taking all trial results into account. Both the horizontal and vertical MRTD measurements were taken repeating the same process. As in FLIR-92, the two-dimensional MRTD were also calculated for a complete analysis.

3.   Measurement Results

The complete set of the subjective MRTD measurement results is given in Appendix E. Figure 5.3 portrays the corresponding MRTD plots as a function of spatial frequency. As mentioned before this data will be compared to the Visibility model and the FLIR-92 model predictions later in this chapter.

There are several conclusions that should be pointed out from the subjective MRTD measurement results as follows.

There is an eye-catching difference between the horizontal and vertical MRTD measurement results. System MRTD performance in the horizontal direction appeared to

be better than that in the vertical direction. This conclusion can be tied to the difference between the horizontal and vertical MTF values of the system.

The MRTDs of the Mitsubishi system seemed to have nonzero low spatial frequency limits that were measured to be 0.08 and 0.15 degrees C in the horizontal and vertical directions respectively. As mentioned in Chapter IV, this physical reality was used as the principal construction milestone of the Visibility model.

The typical asymptotic characteristic of an MRTD curve above a particular spatial frequency value is clearly noticeable in the MRTD plots of the Mitsubishi system as in Figure 5.3. Finally, a close examination of the results and plots provided in Appendix E indicates a significant difference between the measurements taken as the back plate is heated up and the measurements taken as the back plate is cooled down. This observation can be attributed to a perception experience such that it is easier to track a bar pattern as it disappears after it has been resolved than to recognize a new pattern as it starts to appear out of noise.

The tolerance of the thermocouples used to measure the plate temperatures was not perfect. They had a measurement precision of 0.0556 degrees C that corresponds to 0.1 degrees F.
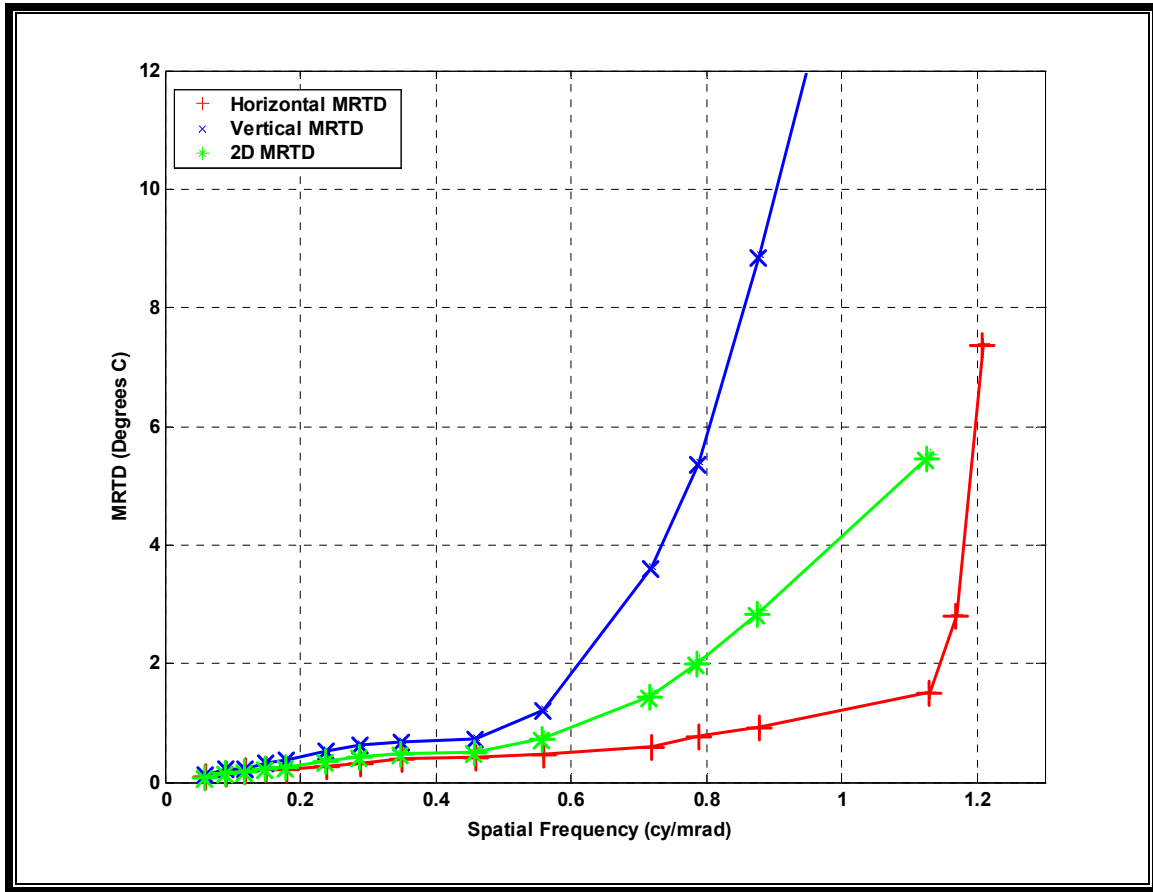
Figure 5.3.   Mitsubishi System Average Subjective MRTD Plots.

B.   THE OBJECTIVE MRTD MEASUREMENTS

1.   Experimental Setup

As discussed before in Chapter IV, the dependence on human observer makes the MRTD measurements subjective and unrepeatable. Although several approaches have been proposed in the literature [Refs. 27, 28, 29 and 30], there is no standard objective MRTD measurement procedure that has been accepted yet. However the trend in operating an ATR device to objectively decide the resolvability of a target in the presence of noise is becoming an effective method of eliminating the human dependence.

The objective MRTD experimental equipment at the Naval Postgraduate School was arranged as shown in Figure 5.4. In contrast to the subjective MRTD measurement

setup the display and the observer were taken out of the loop while an oscilloscope was directly connected to the thermal imager, simulating the simplest form of an ATR device.

Thermal Imager

R

Target

Uniform
Background

Oscilloscope
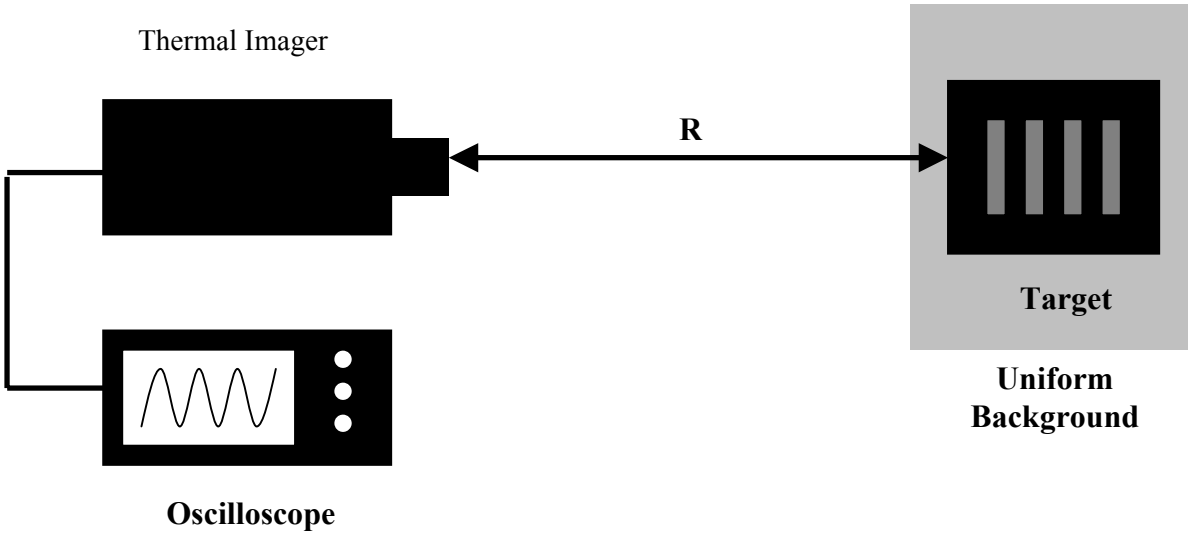
Figure 5.4.   The Experimental Setup.

2.   **Experimental Methodology**

Since ATR based MRTD measurements are basically related to SNR, calculation of noise becomes a major preliminary process. First the noise voltage measured along a video scan line across the target pattern was viewed on an oscilloscope screen as seen in Figure 5.5. Next, the average noise voltage was calculated as 8.1mV by taking samples from the curve in the figure. Then the SNR requirement for the desired discrimination task was determined from the ratio of the voltages ($\Delta V_{SIGNAL}/\Delta V_{NOISE}$), where ΔV_{NOISE} was set to 8.1mV.
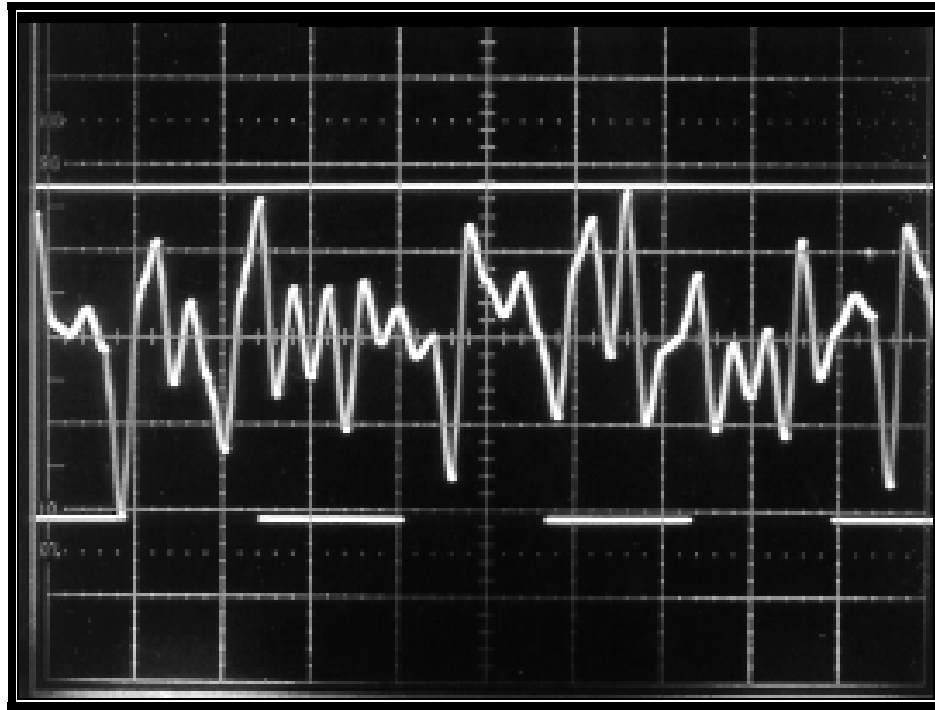
Figure 5.5.   Noise Voltage as seen on the Oscilloscope.

A typical SNR measurement is demonstrated in Figure 5.6. For example, a signal voltage level (ΔV_{SIGNAL}) of 32.6mV is required on the oscilloscope screen to call a target 'resolved' for a SNR requirement of 4.0.

Two sets of measurements were taken in the objective MRTD experiment. First, SNR was held constant while the MRTD values were recorded for a range of bar spatial frequencies. SNR was set to 6.0 for a 100% probability of detection. Second, bar spatial frequency was held constant while the MRTD values were recorded for various SNR requirements.
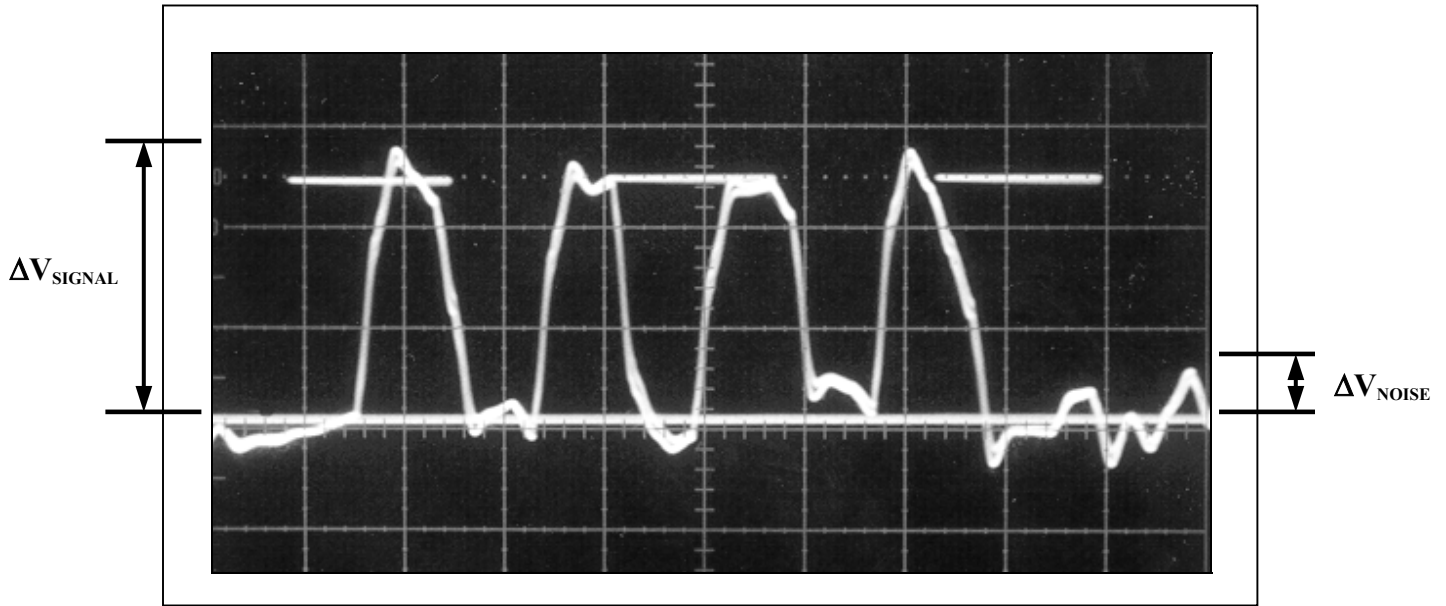
Figure 5.6.   A Typical SNR Measurement on the Oscilloscope.

3.   Measurement Results

A complete set of measurement data is provided in Appendix E. Figures 5.7 and 5.8 below show the plots of MRTD versus spatial frequency for a constant SNR of 6.0 and MRTD versus SNR for various constant spatial frequencies respectively.

When the MRTD values obtained from the two sets of measurements are compared i.e. for SNR of 6.0, it is obvious that the objective MRTD scheme yields considerably more reproducible results. However, objective MRTD values turned out to be much higher than the MRTD values obtained from the subjective measurements i.e. for SNR value of 6.0. This conclusion suggests that the eye is an outstanding detector of signal out of noise. The objective measurement results will be compared to the objective predictions of the Visibility model also in this chapter.
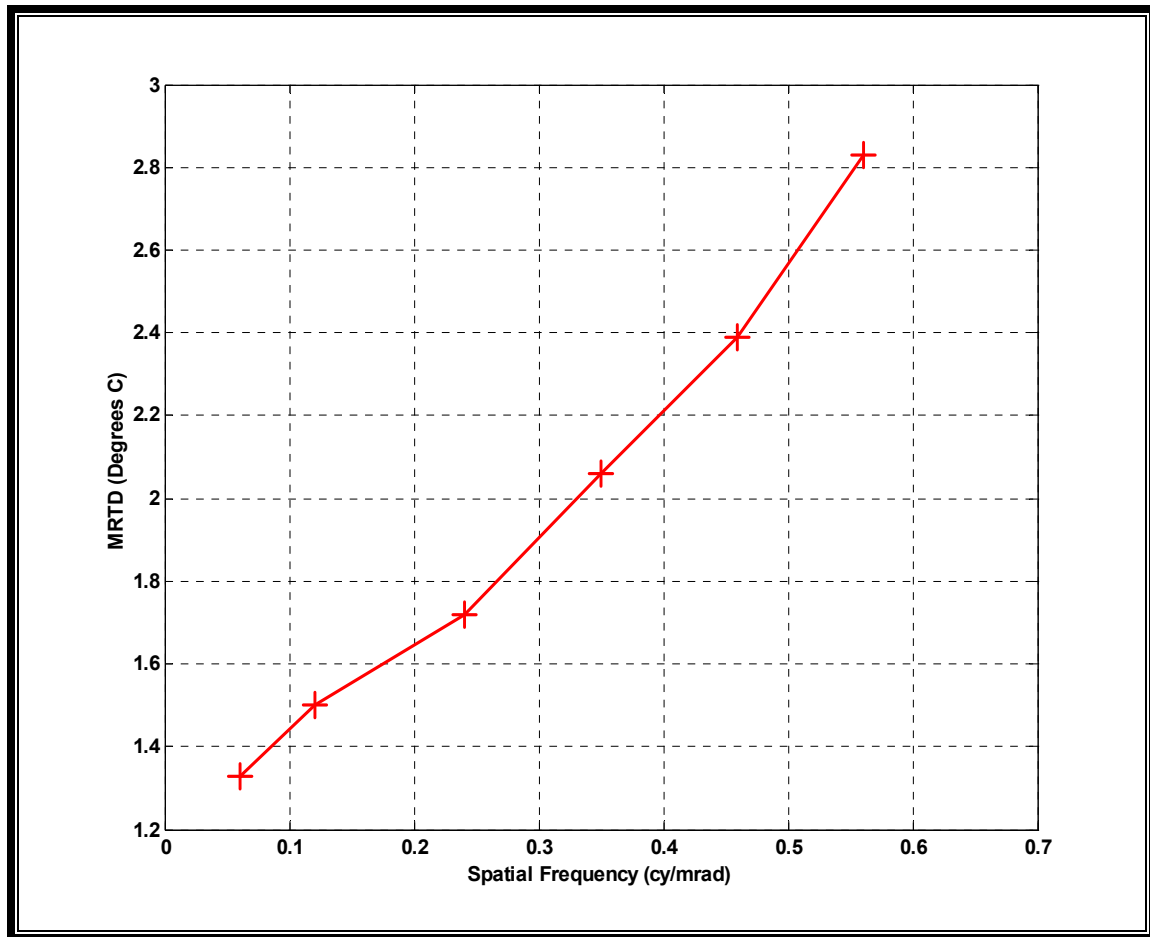
Figure 5.7.   Objective MRTD vs. Spatial Frequency for a SNR of 6.0.
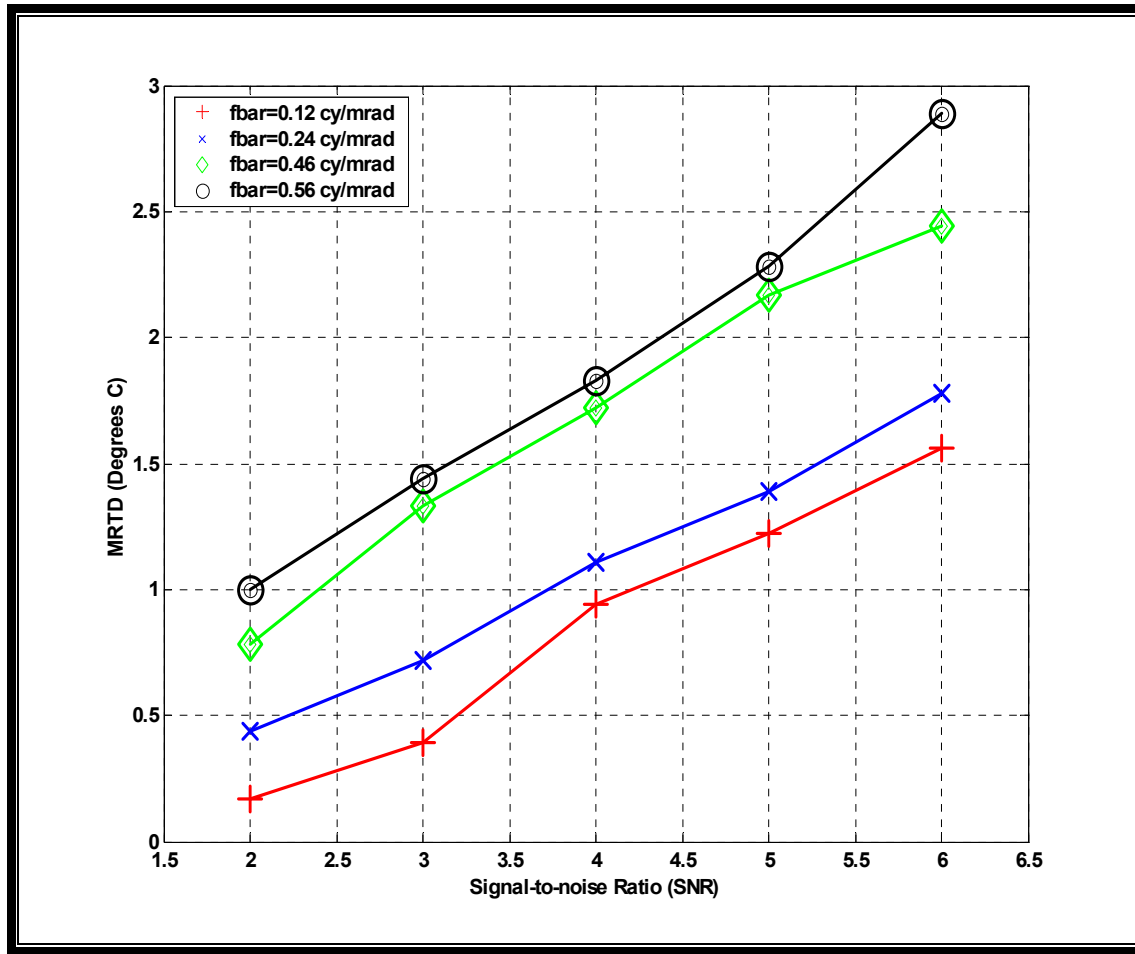
Figure 5.8.   Objective MRTD vs. SNR for Constant Spatial Frequencies.

C.   COMPARATIVE DATA ANALYSIS

The purpose of this subsection is to make a comparative analysis of the Visibility model predictions to the measured data. Furthermore this analysis will validate the applicability of the Visibility concept to staring thermal imagers.

First, the subjective MRTD measurement results will be compared to both the Visibility model and the FLIR-92 model subjective MRTD predictions. Second, the objective MRTD measurement results will be compared to the Visibility model objective predictions. All prediction results of both models are presented graphically in Appendix F.

1.   Comparison of the Subjective MRTD Measurements to the Predictions

In Figures 5.9, 5.10 and 5.11, horizontal, vertical and the 2-D MRTD predictions of the Visibility and the FLIR-92 models are compared to the MRTD measurement results. The 2-D MRTD measurement data is calculated by geometrical averaging of the measured horizontal and vertical MRTD values, in the same manner that the other 2-D MRTD values were obtained.

As seen in Figure 5.9, the horizontal MRTD predictions of both models are observed to be optimistic at low spatial frequencies and pessimistic at high spatial frequencies. On the other hand, both models seem to give optimistic results for the vertical and the 2-D MRTD values as demonstrated in Figures 5.10 and 5.11 respectively.
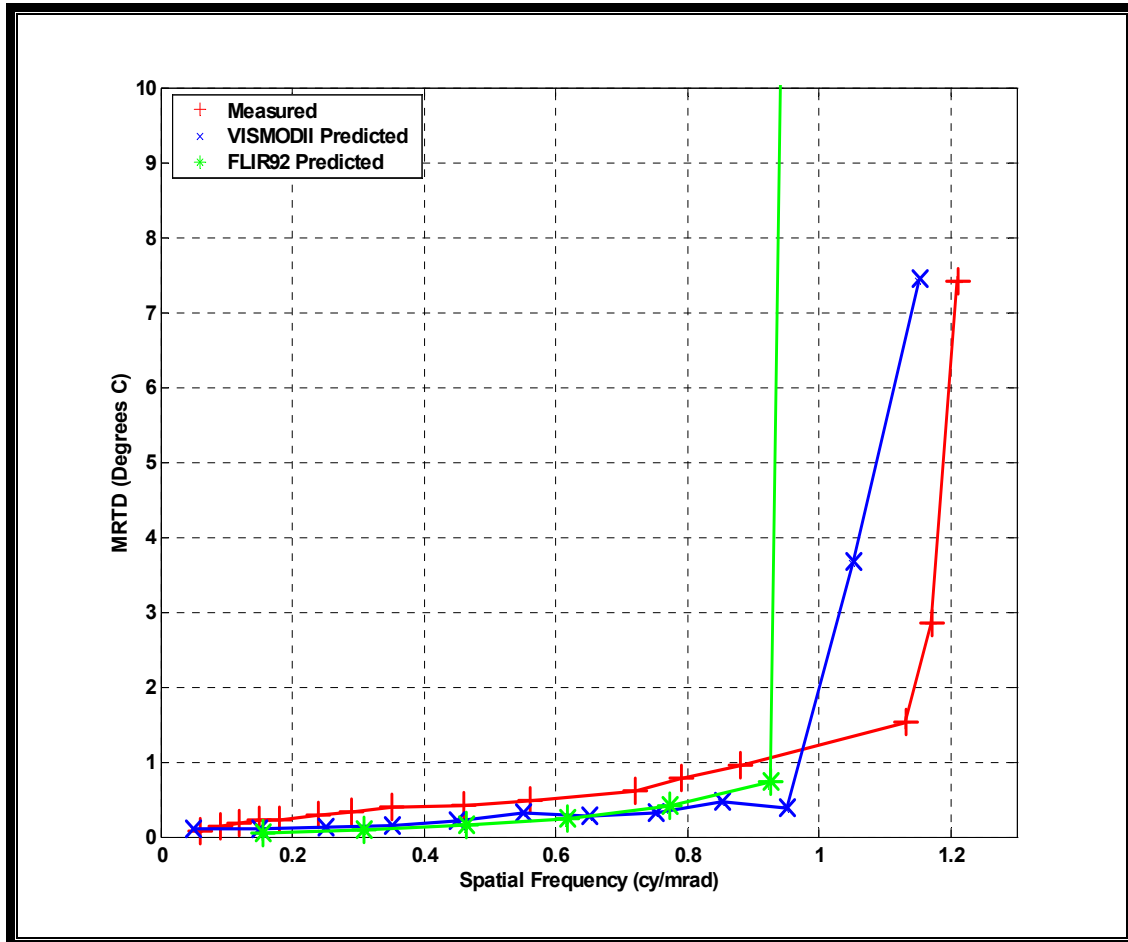
Figure 5.9.   Horizontal MRTD Comparison.
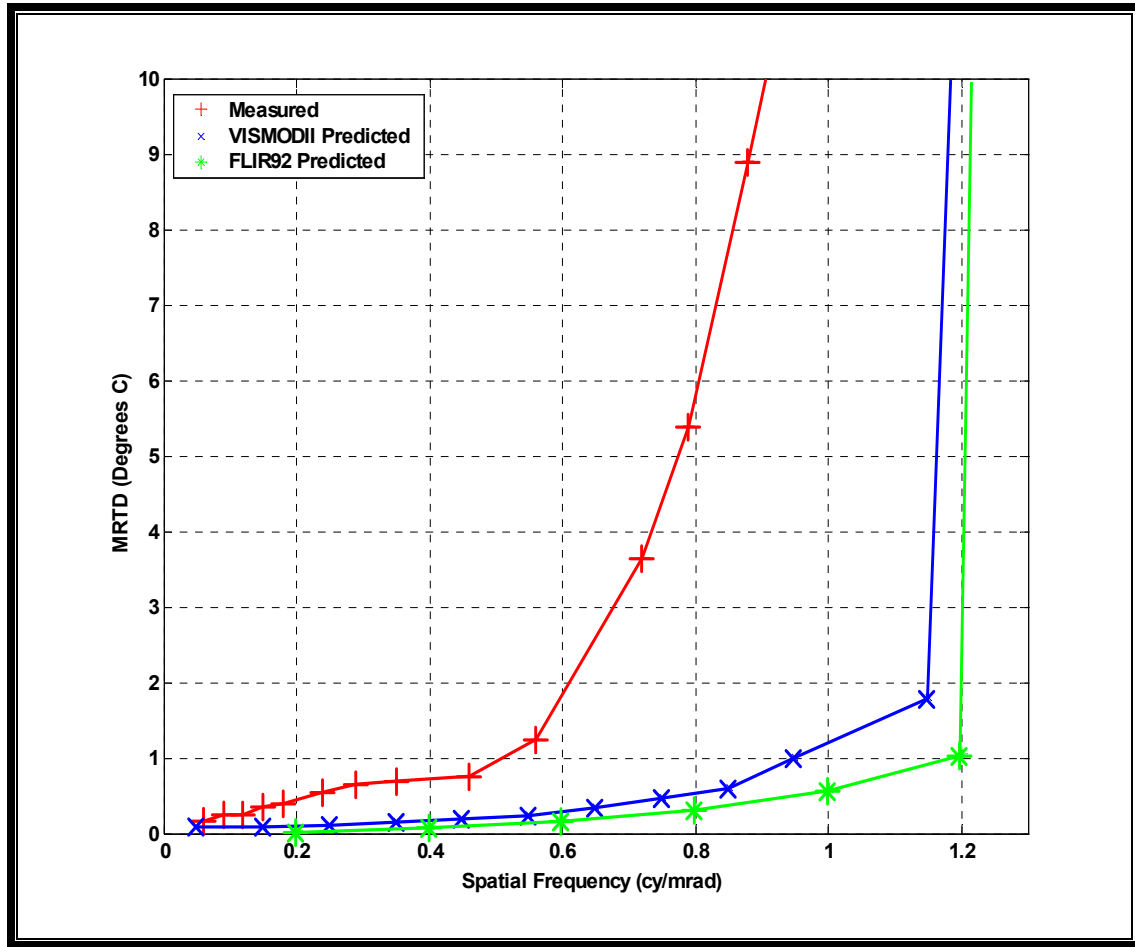
Figure 5.10.   Vertical MRTD Comparison.

In Figures 5.9 and 5.10, it is noticeable that the Visibility and the FLIR-92 models tend to give quite close predictions in the horizontal and vertical directions up to the Nyquist frequency limit. It is also observable that the FLIR-92 predictions are limited to the Nyquist frequency in the corresponding direction. However the Visibility model predictions extend beyond this point, because the actual laboratory measurements suggest that resolution is still possible.
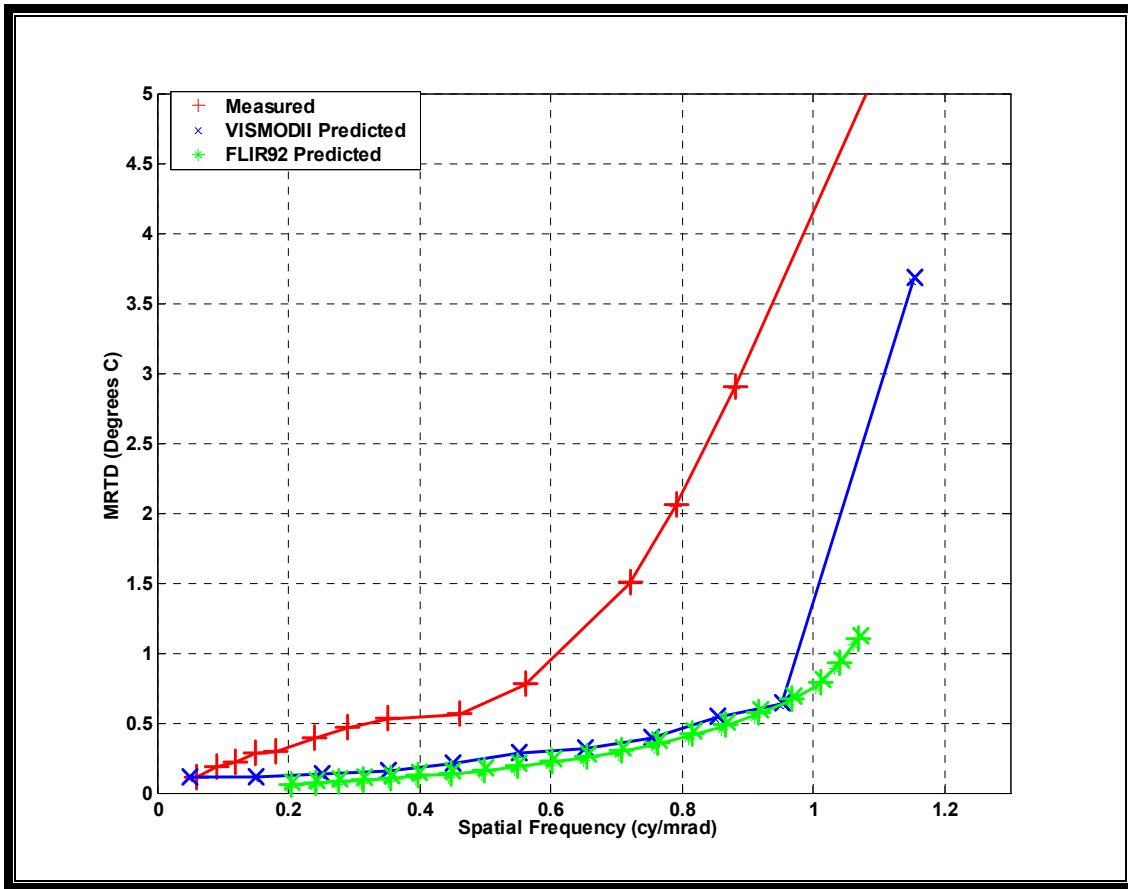
Figure 5.11.   2-D MRTD Comparison.

Figures 5.12, 5.13 and 5.14 are given to show the tendency in MRTD predictions in the low spatial frequency limit. It is clearly observable that the Visibility model calculates the low spatial frequency limit that was originally defined as ΔT_{SC} (threshold input contrast) in the model quite precisely. However the FLIR-92 predictions tend to go to zero in the low spatial frequency region.
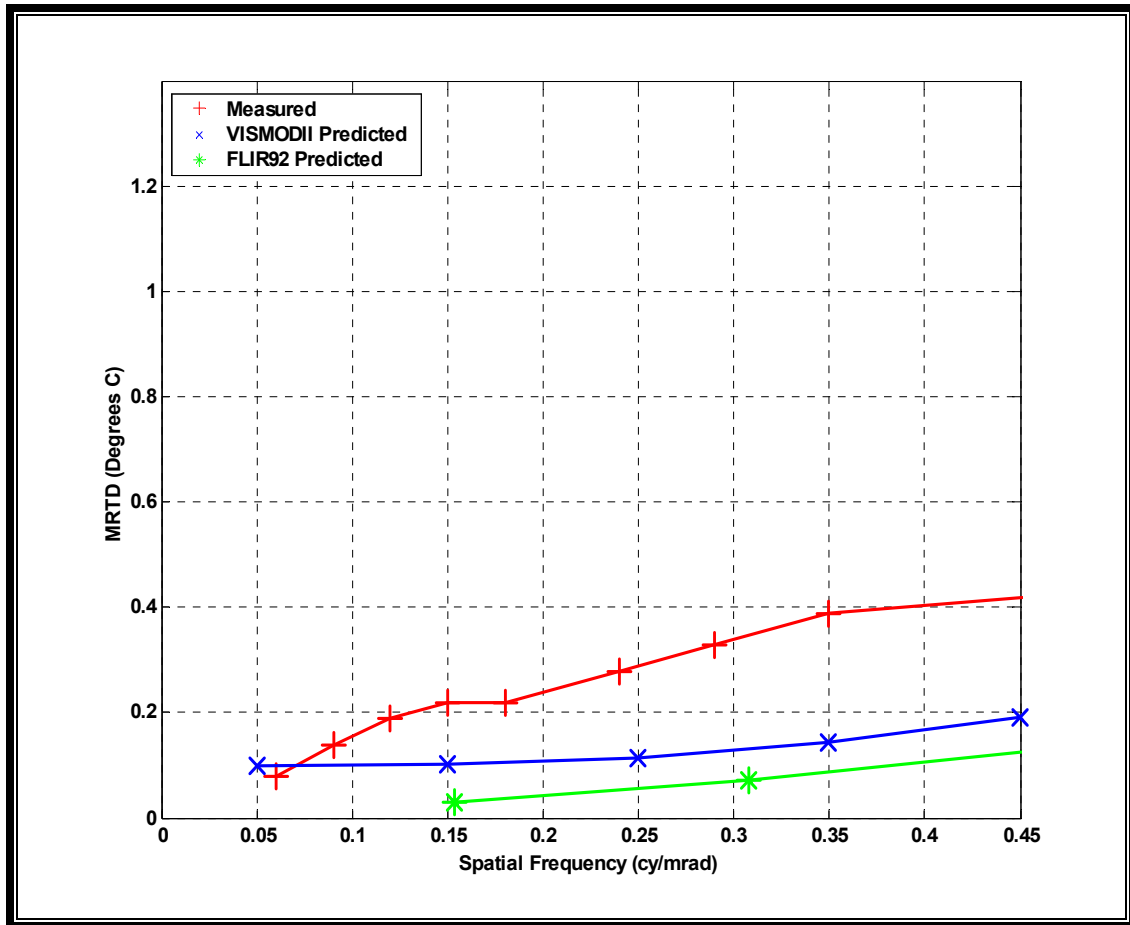
Figure 5.12.   Horizontal MRTD Comparison at Low Spatial Frequencies.
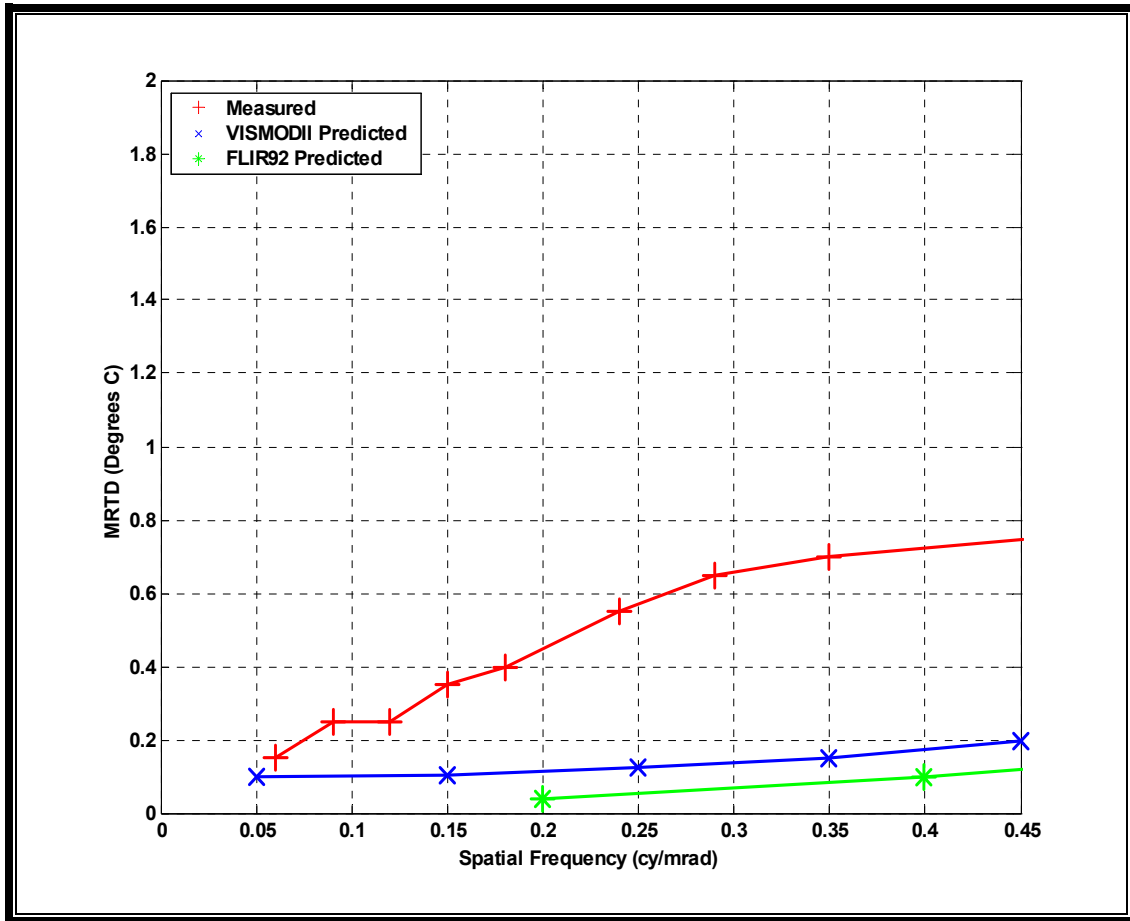
Figure 5.13.   Vertical MRTD Comparison at Low Spatial Frequencies.
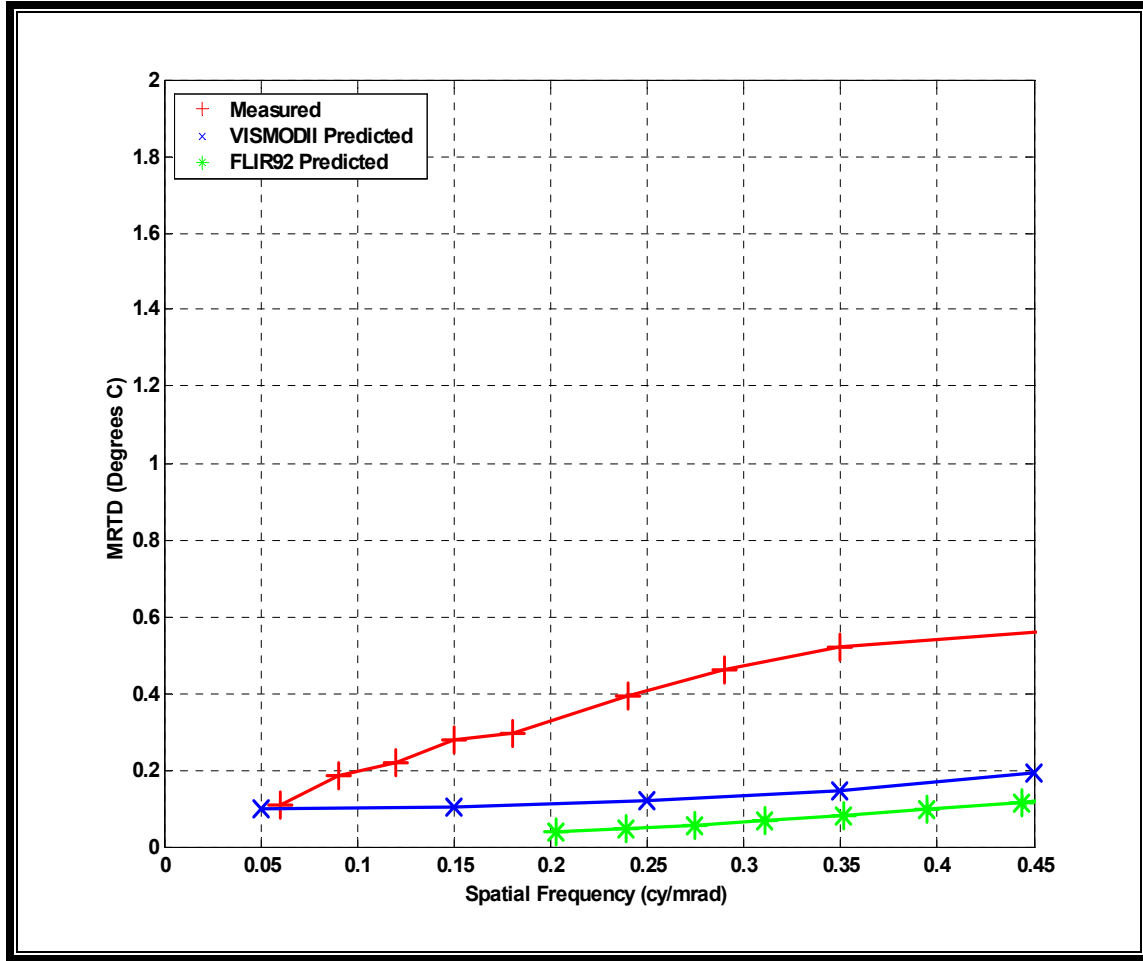
Figure 5.14.   2-D MRTD Comparison at Low Spatial Frequencies.

Finally, it can be said that the Visibility model predictions are in better agreement with the measured results than are the FLIR-92 model predictions, as noticed in the figures given in this section.

2.   Comparison of the Objective MRTD Measurements to the Predictions

Since there is no objective MRTD predictor version of the FLIR-92 model yet, the measurement results are only compared to the Visibility model predictions. First, the measurement results are compared to the predictions when the SNR is held constant (SNR=6.0) as also demonstrated in Figure 5.15. Although the Visibility model predictions seem to be more optimistic than the measured results, there is a reasonable agreement between the two curves. Moreover the measurement and the prediction

nonzero low frequency limits are quite close to each other, indicating that the basic physical reasoning of the Visibility model is correctly constructed.
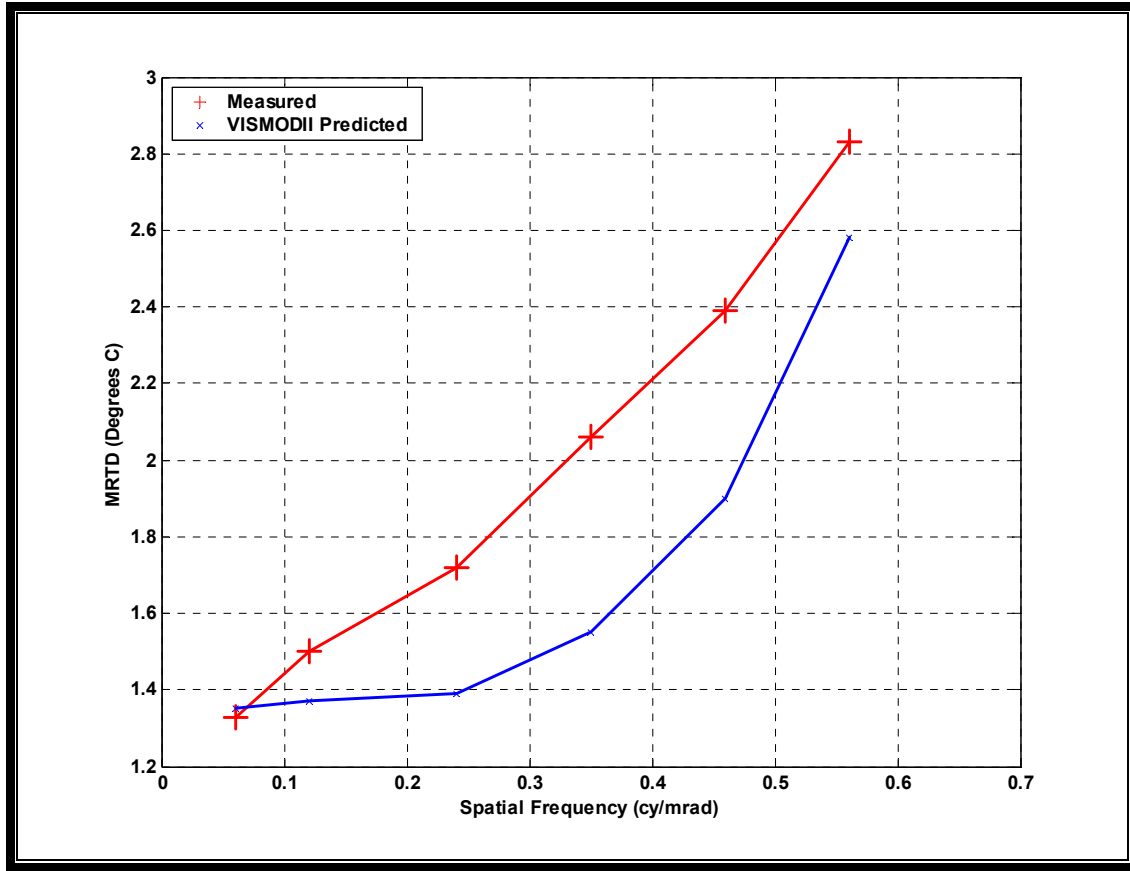
Figure 5.15.   Objective MRTD Comparison (Constant SNR = 6.0).

Second, the measurement results are compared to the predictions as a function of SNR when bar spatial frequency is held constant as demonstrated in Figures 5.16, 5.17, 5.18 and 5.19. The spatial frequencies were chosen to be 0.12, 0.24, 0.46 and 0.56 cycles/mrad. Each figure clearly portrays the agreement between the measured and the predicted results. However the best agreement is observed at 0.56 cycles/mrad bar spatial frequency (Figure 5.19), which was also the maximum bar spatial frequency utilized in these measurements/predictions (Figure 5.15).
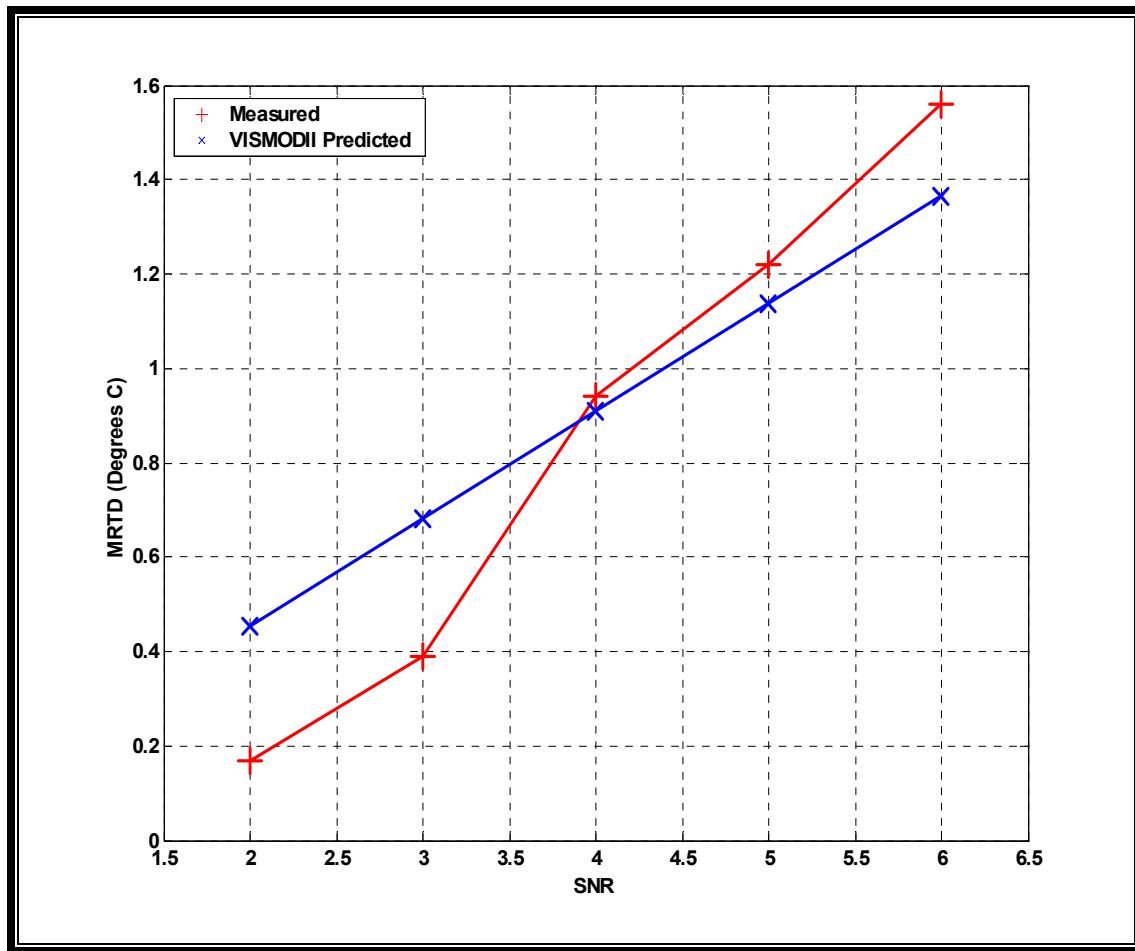
Figure 5.16. Objective MRTD vs. SNR Comparison for Constant Spatial Frequency (0.12 cycles/mrad).
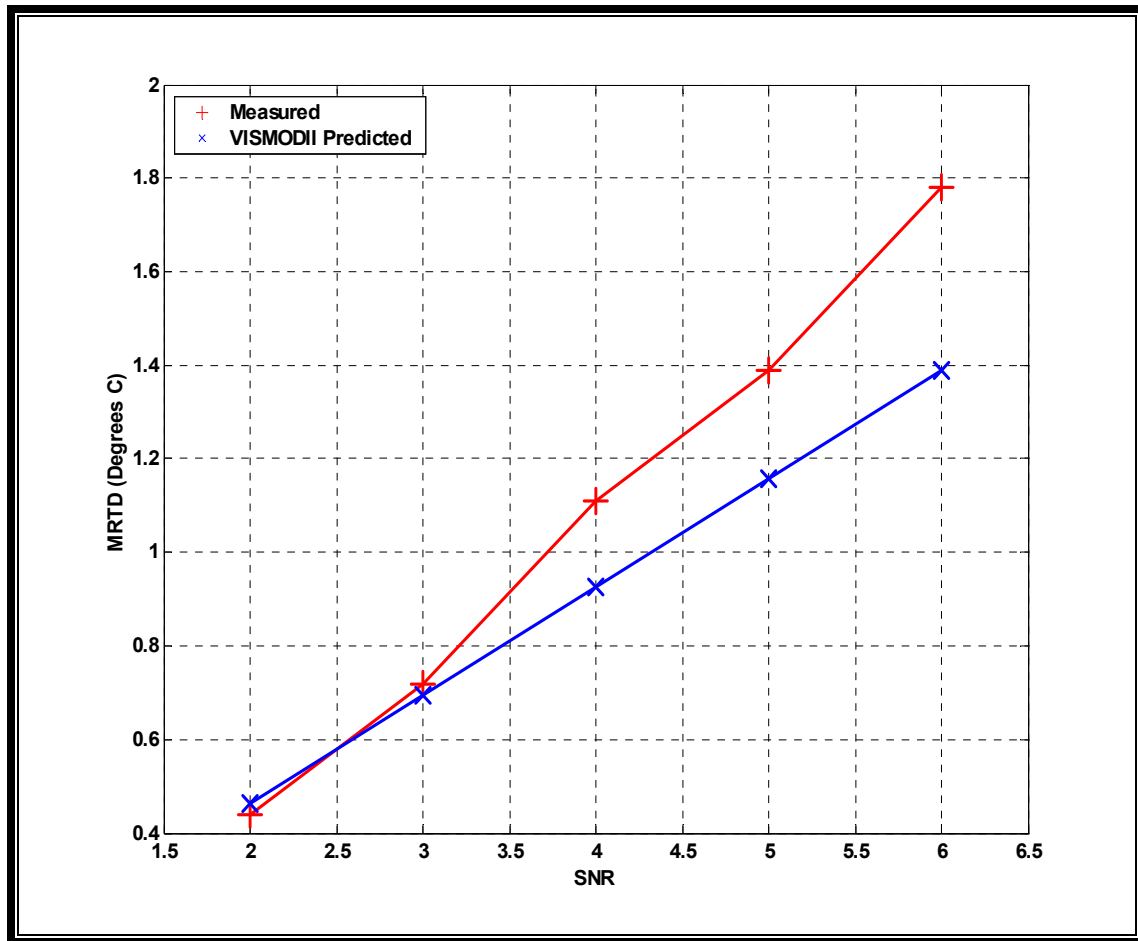
Figure 5.17.   Objective MRTD vs. SNR Comparison for Constant Spatial Frequency (0.24 cycles/mrad).
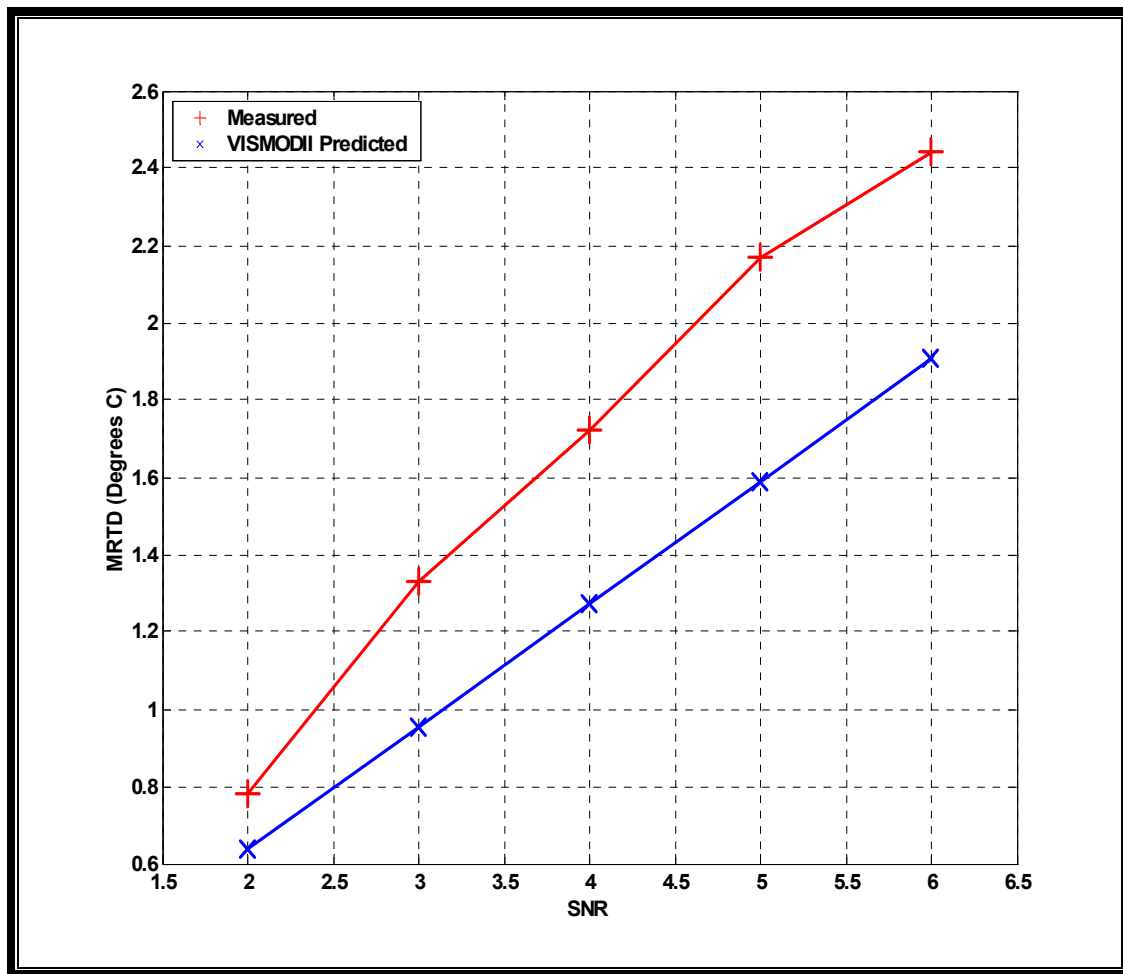
Figure 5.18.   Objective MRTD vs. SNR Comparison for Constant Spatial Frequency (0.46 cycles/mrad).
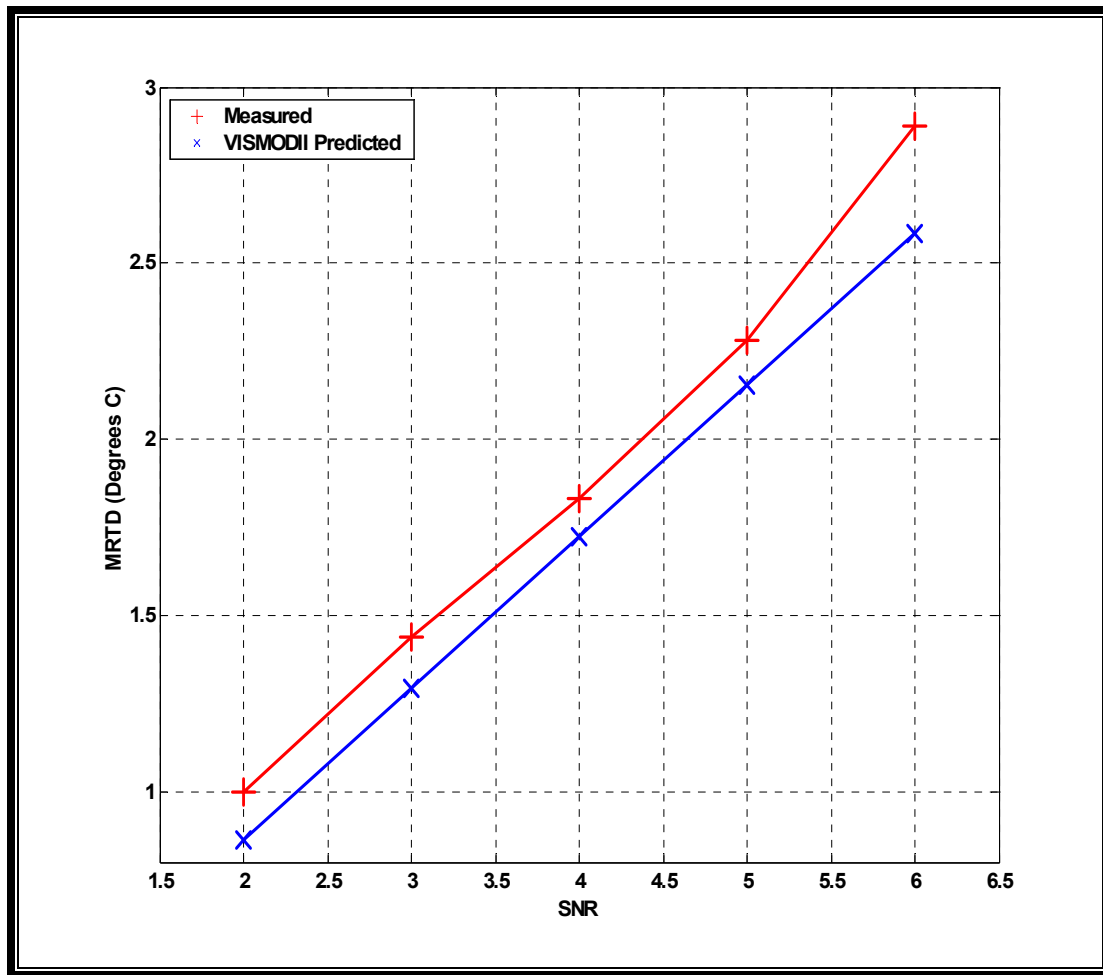
Figure 5.19.   Objective MRTD vs. SNR Comparison for Constant Spatial Frequency (0.56 cycles/mrad).

This analysis, although limited in scope, shows that the Visibility model can provide reasonably accurate performance predictions of thermal imaging systems. Therefore the laboratory confirmation of the model for both subjective and objective MRTD schemes is considered to be successfully accomplished.

VI. VIRTUAL THERMAL IMAGE-PROCESSING MODEL

The purpose of this chapter is to introduce the basics of a new virtual thermal image-processing model, which is proposed in this thesis. This visualization tool is based on an earlier simulation program, the Visibility model.

A. INTRODUCTION

Recently, the U.S. Army Night Vision Electronics Sensors Directorate has begun performing Virtual MRTD experiments pursuing a concept known as simulation based modeling. As a result, a simulation program based on the FLIR-92 model was developed. In the experiments, a scanning thermal imaging system operating in the mid-wave infrared band was simulated and the effects of blurring and noise on the image were reported [Ref. 23].

Inspired by this preceding work, a new Virtual Image-Processing Model that is based on the Visibility model has been developed at the Naval Postgraduate School. Like the Visibility model, the Virtual Thermal Image-Processing model is written using the MATLAB computational software. It takes the current thermal imaging system-modeling concerns such as noise, scene phasing, sampling and aliasing into account and creates visual images comparable to those that can be obtained with the actual system being modeled. This allows the user to analyze and evaluate separately the effects of noise, scene phasing, sampling and aliasing on the final imagery. Moreover the model provides control over the system parameters for the analyst, which might be helpful in performing realistic tests in the design of the systems under evaluation.

B. THE LOGICAL FLOW OF THE MODEL

At the front end of the Virtual Thermal Image-Processing model, the system parameters of a particular thermal imaging device must initially be loaded. For this thesis, the parameters of the Mitsubishi Electronics IR-M500 Thermal Imager, which is also used in the laboratory measurements, are entered as previously given in Appendix D.

To provide a more convenient implementation of the effects of relevant concerns such as sampling and aliasing in the thermal imaging systems, the program primarily

operates in the two-dimensional spatial frequency domain. Hence the two dimensional Fast Fourier Transform (2-D FFT) of the bar pattern is taken to obtain a four-bar target spectrum.
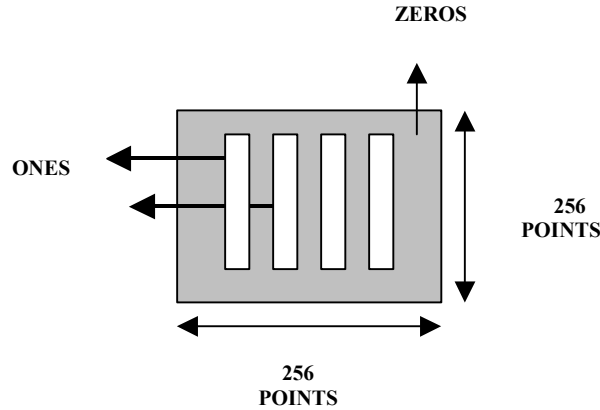
Figure 6.1.   The Input Bar Pattern is Represented by a 256 x 256 Matrix of Values Zero and One.

The Virtual Thermal Image-Processing Model starts with generating a numerical model of the input four-bar pattern by 256 x 256 points of values zero and one as shown in Figure 6.1. As the images at various spatial frequencies are analyzed, the number of points (256x256) representing the input bar pattern stays constant, but the number of points per unit angular subtense (mrad) is varied. Therefore the axes on the output images are properly scaled with respect to the desired bar spatial frequency. Then the model operates for one spatial frequency at a time and loops through all spatial frequencies of interest to provide an output image for each spatial frequency. It works for both horizontal and vertical bar patterns simultaneously.

2-D FFT

Image Formation MTF

MTF_{optics}
MTF_{blur}
$MTF_{detector}$
$MTF_{Scene-Phasing}$ **(optional)**

Σ

2-D FFT

White noise

Sampling and Aliasing

Image Reconstruction MTF

$MTF_{electronics}$
$PTF_{electronics}$
$MTF_{detector}$
$MTF_{display}$

2-D IFFT

Visual four-bar target image
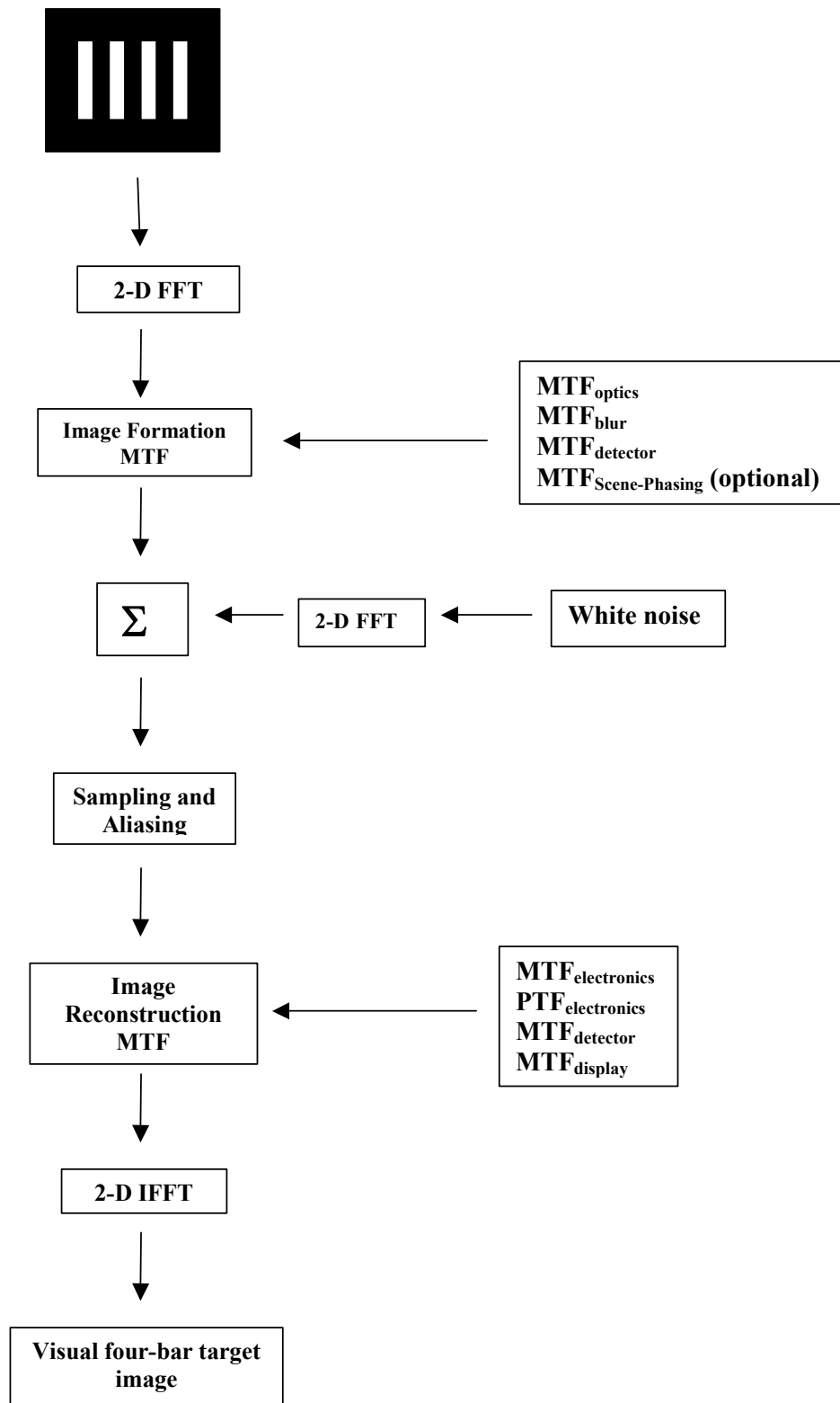
Figure 6.2.   Block Diagram of the Virtual Thermal Image-Processing Model.

In the next stage, the model computes an Image Formation MTF that is multiplied with the four-bar target spectrum in the spatial frequency domain as shown in the block diagram in Figure 6.2. Then white noise is generated to account for the overall system noise. After taking its 2-D FFT, the noise spectrum is obtained and simply added to the filtered target spectrum. Further discussions about the calculation and the generation of white noise will be given in the noise analysis of this chapter.

The sampling process is applied to the pre-filtered, noise added target spectrum in the spatial frequency domain as performed in the Visibility model. The net result of this process is the occurrence of the sampled spectrum replicas at the multiples of the sampling frequency in both horizontal and vertical directions.

Next the Virtual Thermal Image-Processing Model calculates the Image Reconstruction filter frequency response and then multiplies it with the aliased target spectrum in the spatial frequency domain. Finally taking the inverse 2-D FFT of the system output spectrum gives a visual four-bar target representation at that particular spatial frequency.

C. ANALYSIS OF THE SUB-SYSTEM MTFS

Since the Virtual Thermal Image-Processing model is based on the Visibility model, it utilizes the same sub-system MTFs as mentioned before. The model calculates the overall system response by simply multiplying them in the frequency domain.

As shown in Figure 6.2, the sub-system MTFs are categorized into two main groups, the Image Formation MTF and Image Reconstruction MTF. The Image Formation MTF includes the diffraction-limited optical MTF, the geometric blurred optical MTF, the detector spatial MTF and an optional scene phasing MTF, which are given in the following equations.

$$H_{OPTICS}(f) = \frac{2}{\pi}\left[a\cos\left(\frac{f}{f_{OPT}}\right) - \left(\frac{f}{f_{OPT}}\right)\left(1 - \left(\frac{f}{f_{OPT}}\right)\right)^{0.5}\right] \qquad (6.1)$$

$$H_{BLUR}(f) = e^{\left(-2\pi^2 f^2 \sigma_{BLUR}^2\right)} \qquad (6.2)$$

$$H_{DETECTOR}(f_Z) = \left| \frac{\sin(\pi \delta_Z f_Z)}{(\pi \delta_Z f_Z)} \right| \tag{6.3}$$

$$H_{SCENE}(f_Z) = \cos\left(\frac{f_Z}{f_S} \theta_Z \right) \tag{6.4}$$

Where

f   is the two-dimensional spatial frequency in cy/mrad

f_{OPT} is the optical cutoff spatial frequency in cy/mrad

σ_{BLUR} is the standard deviation of the blur spot diameter (σ_{BLUR}=0 in this study)

z   is the direction of interest either horizontal or vertical

δ is the detector angular subtense in mrad

θ is the scene phase angle in rad (θ=0 in this study)

f_S is the detector sampling frequency in cy/mrad

Since the system optics is assumed to have a circular geometry, the diffraction limited and the geometric blurred optical MTFs are symmetric in two dimensions. The detector MTF might also be symmetric depending on its geometry.

Finally, the net Image Formation transfer function is calculated as:

$$H_{IMAGEFORMATION}(f) = H_{OPTICS}(f)H_{BLUR}(f)H_{DETECTOR}(f_X)H_{DETECTOR}(f_Y)$$
$$H_{SCENE}(f_X)H_{SCENE}(f_Y) \tag{6.5}$$

The plot of the Image Formation MTF for the imaging system being modeled is given below in Figure 6.3.
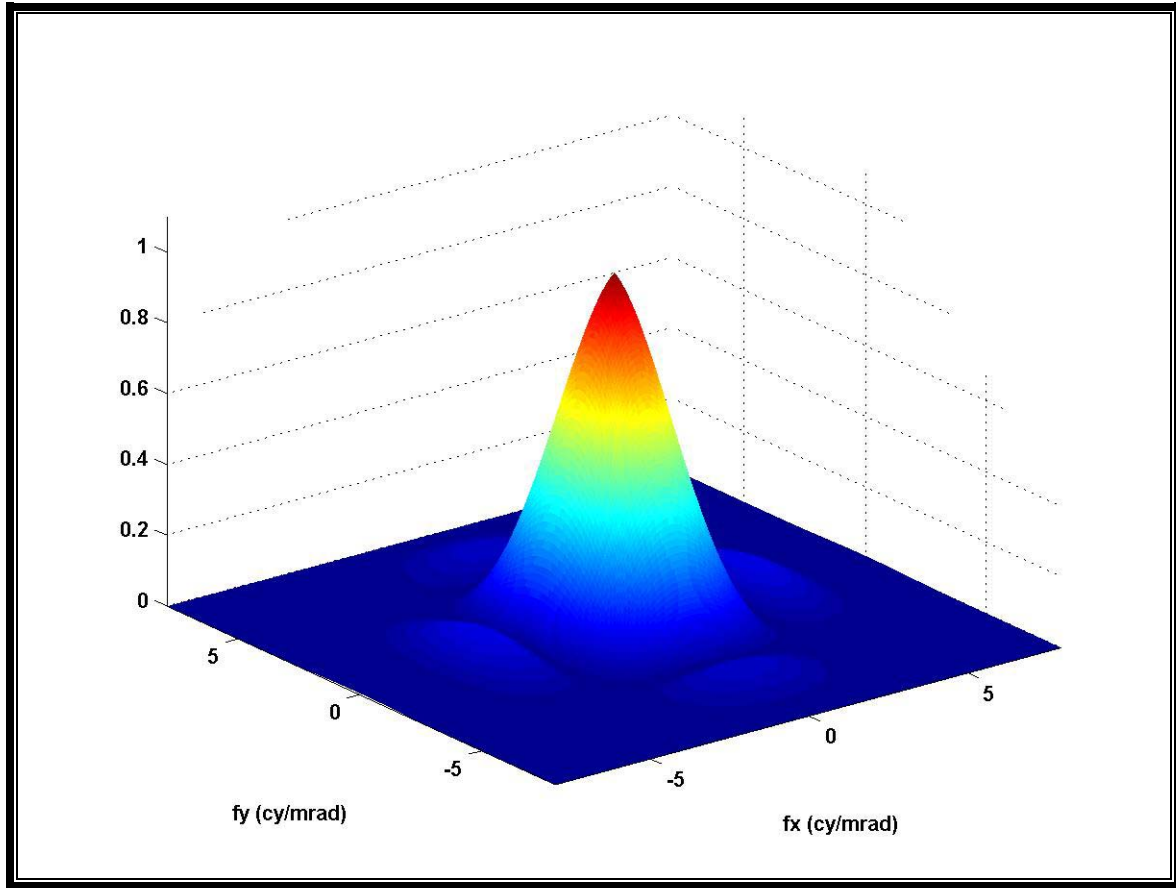
Figure 6.3.   Image Formation MTF of the Modeled Imaging System.

The second group of sub-system MTFs is called the Image Reconstruction MTF, which is obtained from the cascaded form of the electronics OTF, the detector MTF and the display MTF. The electronics OTF is calculated by taking the 2-D FFT of its impulse response function, which is given in Equation 6.6, as discussed previously under the topic of the latest amendments in the Visibility model. The additional detector MTF has the same formulation as given in the image formation process, as suggested by Lloyd. The equations used in the calculation of the Image Reconstruction MTF are given as:

$$h_{ELECTRONICS}(z) = e^{(-2\pi f_C z)} \qquad (6.6)$$

$$H_{DETECTOR}(f_Z) = \left| \frac{\sin(\pi \delta_Z f_Z)}{(\pi \delta_Z f_Z)} \right| \qquad (6.7)$$

$$H_{DISPLAY}(f) = e^{(-2\pi^2 f^2 \sigma^2)} \qquad (6.8)$$

Where

f_C is the electronics cutoff frequency in cy/mrad

Z   is the angular space in mrad

δ   is the detector angular subtense in mrad

f   is the two dimensional spatial frequency in cy/mrad

σ   is the standard deviation of the monitor Gaussian blur spot diameter

It is important to note that with the calculation of the electronics OTF from its impulse response, the non-zero PTF of the electronics is also included into the calculations. The Image Reconstruction transfer function can be written in the cascaded form of:

$$H_{IMAGERECONSTRUCTION}(f) = H_{ELECTRONICS}(f) H_{DETECTOR}(f_X) H_{DETECTOR}(f_Y) H_{DISPLAY}(f)$$

$$(6.9)$$

The plot of the Image Reconstruction MTF for the imaging system being modeled is given in Figure 6.4.
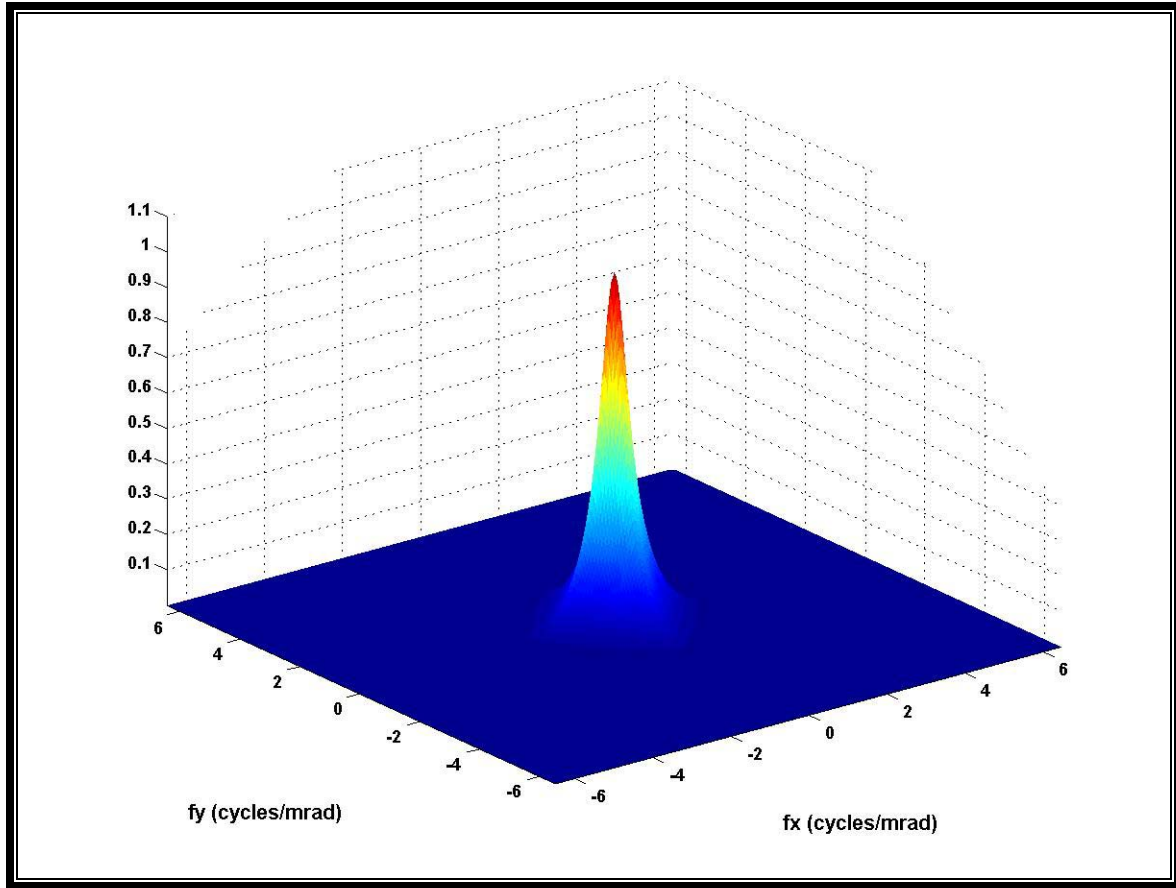
Figure 6.4.   Image Reconstruction MTF of the Modeled Imaging System.

Finally, the overall system MTF can be calculated from Equation 6.10. Figure 6.5 given below shows the plot of the overall system MTF.

$$H_{SYSTEM}\left(f\right) = H_{IMAGEFORMATION}\left(f\right) H_{IMAGERECONSTRUCTION}\left(f\right)$$

(6.10)
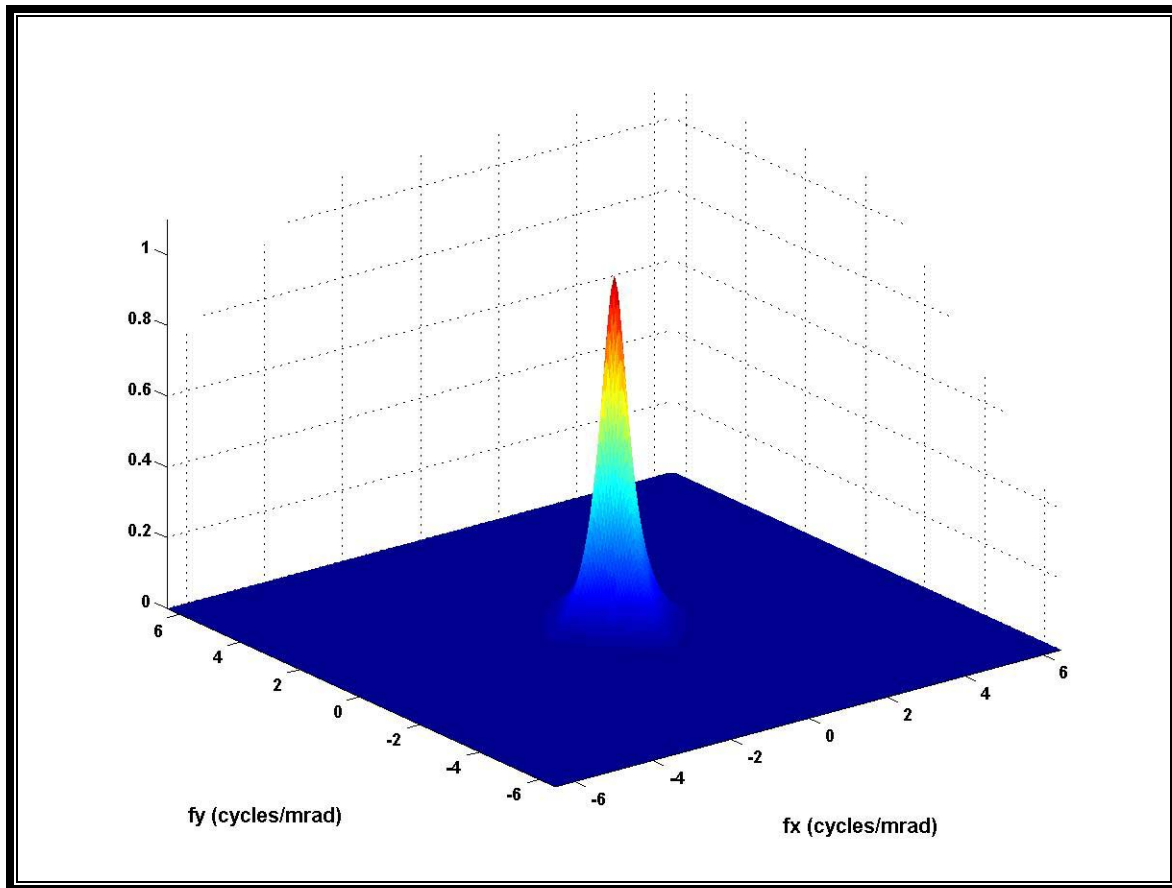
Figure 6.5.   Overall System MTF of the Modeled Imaging System.

D.   NOISE ANALYSIS

The Virtual Thermal Image-Processing model incorporates the updated noise treatment, the 3-D noise concept, in the calculations as the Visibility model does. In both models, only the temporal pixel noise component σ_{TVH} and the spatial noise component σ_{VH} are included in the analysis since they are the dominant noise elements in the staring thermal imaging systems. As discussed previously in Chapter III σ_{TVH} is the only noise component that can be determined either from measurements or from system parameters, while the rest of the noise components can only be determined from measurements. If measurement data is not available σ_{TVH} can be calculated using Equation 3.2 on page 46.

The most significant feature of Equation 3.2 is that it utilizes the actual total bandwidth Δf_P of the system being modeled. The Virtual Thermal Image-Processing model calculates this quantity using the following equation as the Visibility model does.

$$\Delta f_P = \int_0^\infty \left| H_{IMAGERECONSTRUCTION}(f) H_{EYE}(f) \right|^2 df \tag{6.11}$$

Equation 6.11 is the only place where a calculation concerning the observer is included into the model predictions. After the determination of the σ_{TVH} parameter from Equation 3.2, the overall system noise can be calculated using Equation 3.1. Since the noise components other than σ_{TVH} and σ_{VH} are neglected and σ_{VH} is estimated from its default value that is set at $0.40\sigma_{TVH}$ as in the FLIR-92 model, the overall system noise can be calculated from Equation 6.12 given below.

$$\sigma_{TOTAL} = \sigma_{TVH}^2 \left(1 + 0.16\right)^{0.5} \tag{6.12}$$

Once σ_{TOTAL} is calculated, the model generates Gaussian white noise with zero mean and a variance of σ^2_{WHITE} based on the relationship given in the following equation below.

$$\sigma_{WHITE}^2 = \left(\frac{f_{MAX}}{B_{FX} B_{FY}}\right) \sigma_{TOTAL}^2 \tag{6.13}$$

Where

f_{MAX} is the maximum spatial frequency that can be represented using the 2-D FFT in cy/mrad

B_{FX} is the noise equivalent bandwidth in the x direction

B_{FY} is the noise equivalent bandwidth in the y direction

As given in Table 3.2 previously, the detector is the main source of the noise components σ_{TVH} and σ_{VH} in staring thermal imaging systems. Therefore, the white noise spectrum is inserted into the model at the detector to visualize the effect of overall system noise in the output images.

On the other hand, the MATLAB software brings a contrast limitation such that the image contrast values should be in the range of zero to one for a proper visualization. Otherwise the output images of the model may mislead the analyst to erroneous conclusions. Therefore the amplitude of the points forming an image should be kept in the range of zero to one. However addition of Gaussian white noise at the detector produces images such that the condition stated above is violated.

A practical solution to this problem suggests using the function given in Equation 6.14, which appropriately normalizes the amplitude of all points in the image such that they are in the range of interest.

$$F(x) = 0.5\left(\left(\frac{2}{\pi}\right)\tan^{-1}(\alpha(x - 0.5)) + 1\right)$$

(6.14)

Where

x is the input variable

$F(x)$ is the function output

α is a scaling constant set at 5.

To provide a better insight, the plot of this function is given in Figure 6.6. The horizontal axis shows the input values while the vertical axis shows the corresponding output values. Although the input variable x seems to be limited in the range from -1.5 up to $+1.5$, it takes values from $-\infty$ up to $+\infty$ yielding output values between 0 and 1 for a α value of 5.

The effect of noise in the output imagery gets diminished due to the application of the normalization function later in the model. To compensate for this side effect, the

amplitude of the noise spectrum has to be amplified prior to its addition. Therefore the derivative of $F(x)$ is calculated either at $x=0$ or at $x=1$ as function of α, as given in Equation 6.15.

$$\left.\frac{\partial F(x)}{\partial x}\right|_{x\to0\,or\,1} = g(\alpha) = \frac{\alpha}{1+0.25\alpha^2} \qquad (6.15)$$

The transformation will reduce the noise by a factor predicted from Equation 6.15. Finally, the $1/g(\alpha)$ value is multiplied with the noise spectrum as an amplification factor which was calculated to be 1.45 for $\alpha=5$.
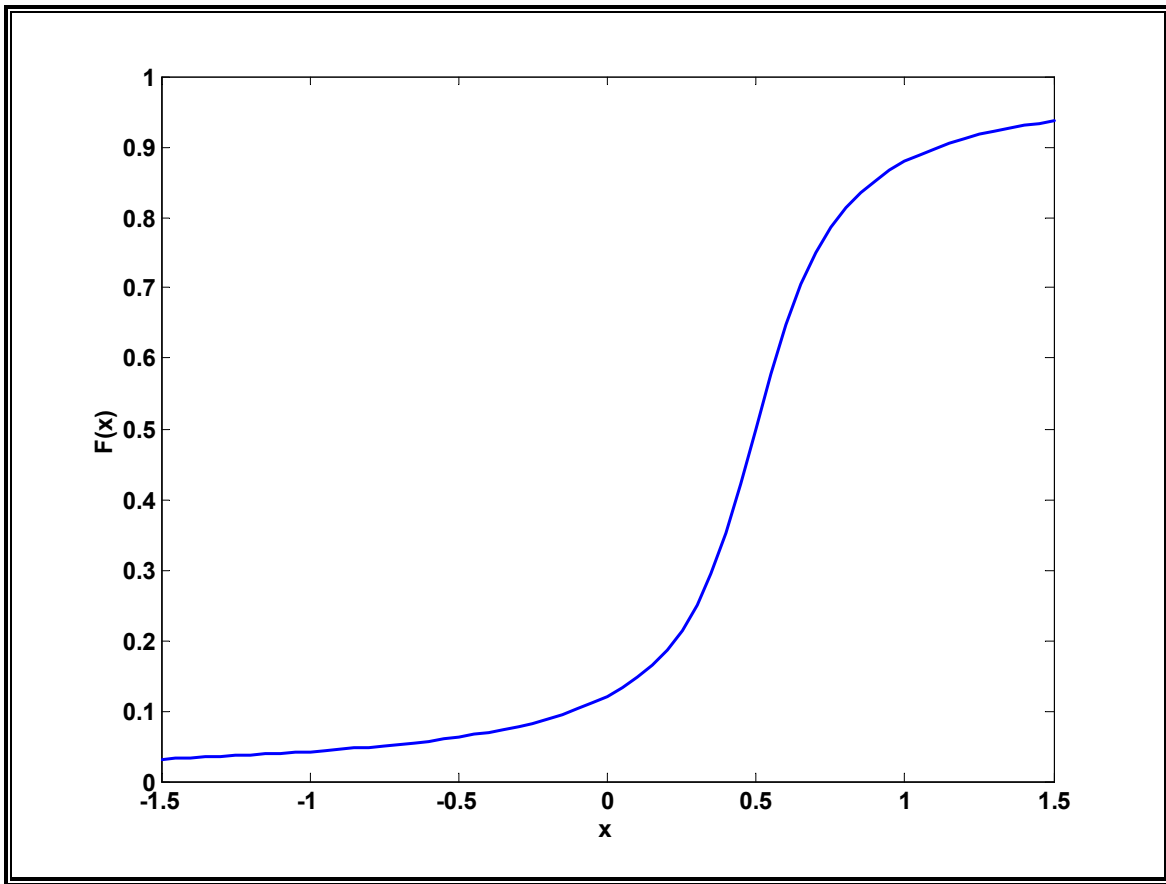
Figure 6.6.   Normalization Function that Keeps the Amplitude of Points in the Image Between Zero and One.

E.   SAMPLE IMAGES

The purpose of this part is to illustrate some sample images using the Virtual Thermal Image-Processing model. The MATLAB code of the model used to create all images presented in this thesis is given in Appendix G.

Figure 6.7 and 6.8 show the horizontal and the vertical four-bar target patterns created as inputs to the modeled thermal imager.

In Figures 6.9 and 6.10, the output images generated for 0.45 cy/mrad bar spatial frequency from the input patterns given in Figures 6.7 and 6.8 are presented respectively. Since the input patterns are generated only once independent of spatial frequency, they remain the same. But all sub-system MTFs, the sampling process and the image axes throughout the model are scaled appropriately for each spatial frequency. Therefore the output images are created with respect to the target bar pattern sizes as seen in the following figures.

A further analysis of the thermal images obtained from the Virtual Thermal Image-Processing model will be made in Chapter VII.

Figure 6.7. **The Horizontal Four-Bar Pattern Created as an Input to the Model.**

Figure 6.8. **The Vertical Four-Bar Pattern Created as an Input to the Model.**
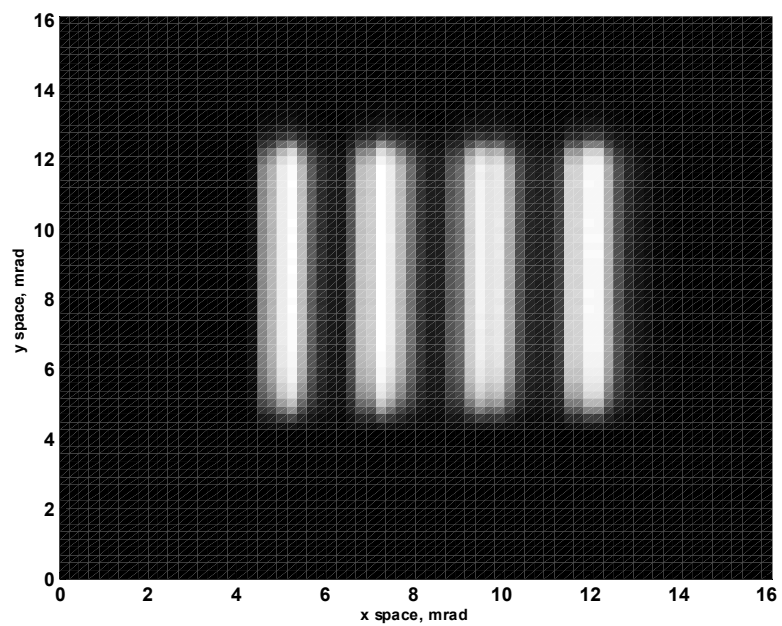
Figure 6.9.   The Horizontal Output Image Created for 0.45 cy/mrad.
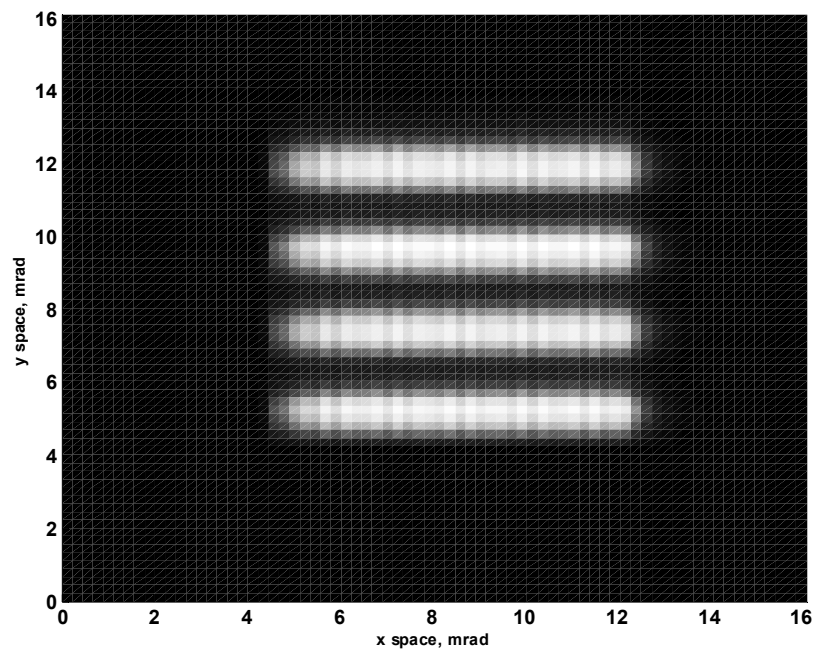
Figure 6.10.   The Vertical Output Image Created for 0.45 cy/mrad.

THIS PAGE INTENTIONALLY LEFT BLANK

VII. THE ANALYSIS OF THE VIRTUAL THERMAL IMAGE-PROCESSING MODEL OUTPUTS AND CONCLUSIONS

The purpose of this chapter is to analyze the output images of the four-bar targets produced by the Virtual Thermal Image-Processing model and to provide useful insights into some of the problems encountered in modeling the TISs such as sampling, aliasing and noise. Moreover the effects of electronics PTF will be examined in the imagery.

The analysis will be made under these sub-topics:

- Aliasing effects below the Nyquist limit
- Aliasing effects above the Nyquist limit
- Exploration of distortion due to aliasing
- Electronics PTF effects

Finally, this chapter will close with some conclusions and suggested directions for future studies.

A. ALIASING EFFECTS BELOW THE NYQUIST LIMIT

As discussed in Chapter II, sampling theory suggests that a frequency component in the original image above the Nyquist limit appears as a lower frequency component after sampling as a result of the phenomenon called 'aliasing'. However, experiments with the Virtual Thermal Image-Processing model showed that aliasing effects were also present in the image of four-bar patterns at spatial frequencies below the Nyquist limit. Figures 7.1 and 7.2 demonstrate the horizontal four-bar target images at 0.65 cycles/mrad including and excluding the effects of aliasing respectively.

The spatial sampling frequencies in the horizontal and vertical directions for the thermal imaging system being modeled were calculated as 1.92 and 2.5 cycles/mrad respectively. Thus, aliasing effects were not expected to appear below 0.96 cycles/mrad bar spatial frequency. However the images in Figures 7.1 and 7.2 revealed the aliasing effects below the Nyquist limit.
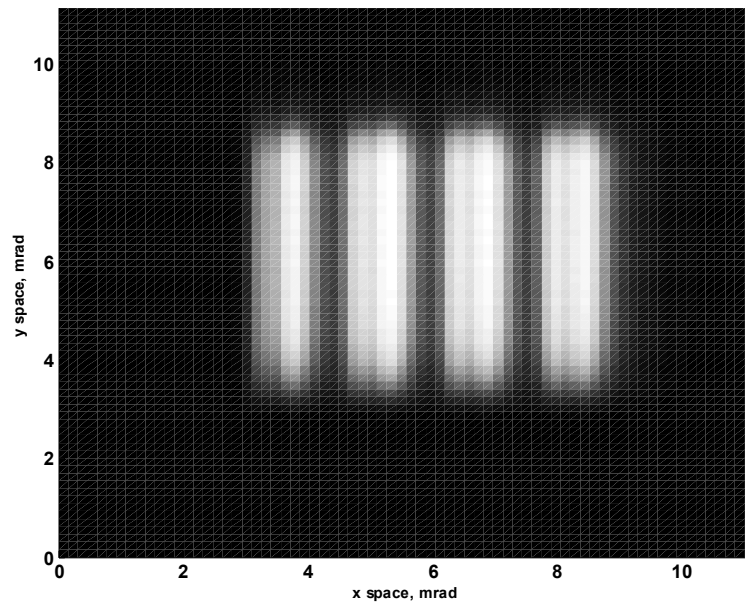
Figure 7.1.   Modeled Four-Bar Target Image with Aliasing At 0.65 Cycles/Mrad. Note the Apparent Broadening of the Slit Images and Appearance of Local Minima.
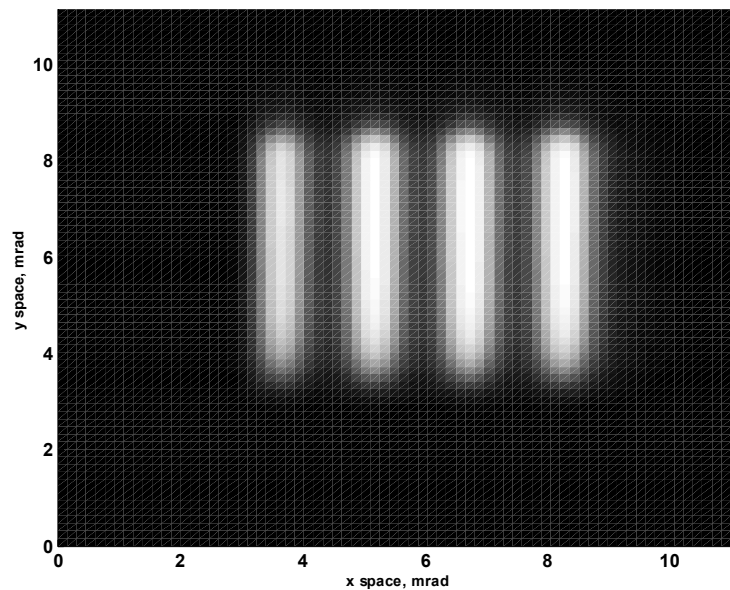
Figure 7.2.   Four-Bar Target Image without Aliasing at 0.65 Cycles/Mrad. Note that there is No Such Broadening Effect in this Image.

An analytic methodology employing a spectrum analysis was developed to support the observed effects of aliasing below the Nyquist limit as presented above [Ref. 31]. Therefore Equation 7.1, which gives the two-dimensional Fourier transform of the four-bar pattern, was used in generating the horizontal bar spectrum. Reference 31 illustrates Equation 7.1 in a different form after letting $k_x=2\pi f_x$ and $k_y=2\pi f_y$.

$$I(f_x, f_y) = \left[\left(\frac{1}{\pi f_x}\right)\left(-\sin\left(\pi f_x W\right) + \sin\left(3\pi f_x W\right) - \sin\left(5\pi f_x W\right) + \sin\left(7\pi f_x W\right)\right)\right]$$

$$\times \left(\frac{1}{\pi f_y W}\right)\sin\left(7\pi f_y W\right) \tag{7.1}$$

Where

f_x is the spatial frequency along the horizontal direction in cycles/mrad

f_y is the spatial frequency along the vertical direction in cycles/mrad

W is the angular width of a bar in mrad

A plot of the horizontal four-bar spectrum along the x-axis ($f_y=0$) at 0.65 cycles/mrad is given in Figure 7.3. The original spectrum, which is centered at zero cycles/mrad, repeats itself at intervals of the sampling frequency. More importantly, the figure reveals the fact that the replicas overlap with the original target spectrum although the four-bar target frequency is below the Nyquist limit. The result of this analysis is in agreement with the previous result obtained from the Virtual Thermal Image-Processing model. Therefore it is important to note that aliasing effects should be considered for bar-targets at four-bar spatial frequencies also below the Nyquist limit.
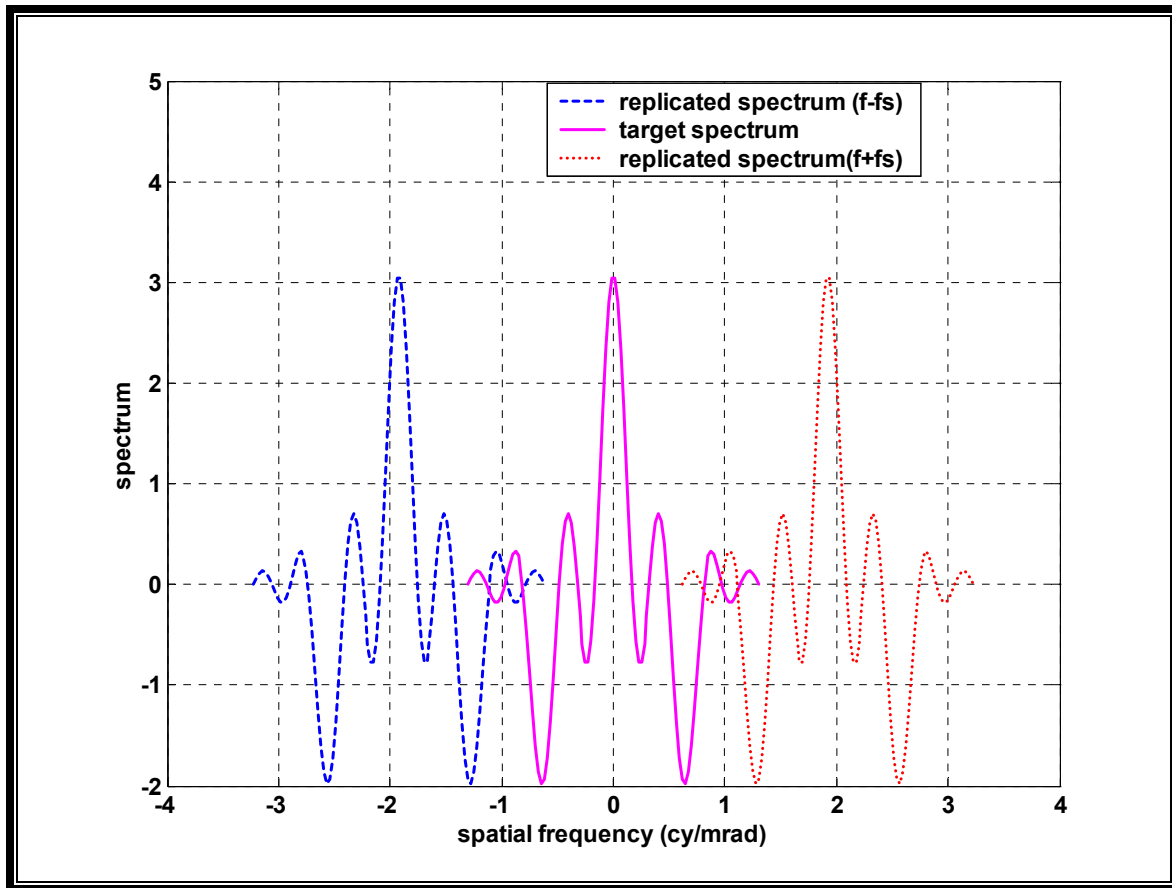
Figure 7.3.   Horizontal Four-Bar Spectrum Along X-Axis (f_Y=0) at 0.65 Cycles/Mrad Showing the Overlap of the Aliased Spectra.

A last observation in the region below the Nyquist frequency concerns the contrast level in the target images generated by the model. Figure 7.4 demonstrates the plot of a profile across the four-bar target and image centers for the 0.65-cycles/mrad target. Although there is a general interpretation that aliasing causes a visual degradation effect in the image, this analysis shows that aliasing may actually cause noticeable contrast enhancements in the four-bar target imagery for the bar-target spatial frequencies below the Nyquist limit.
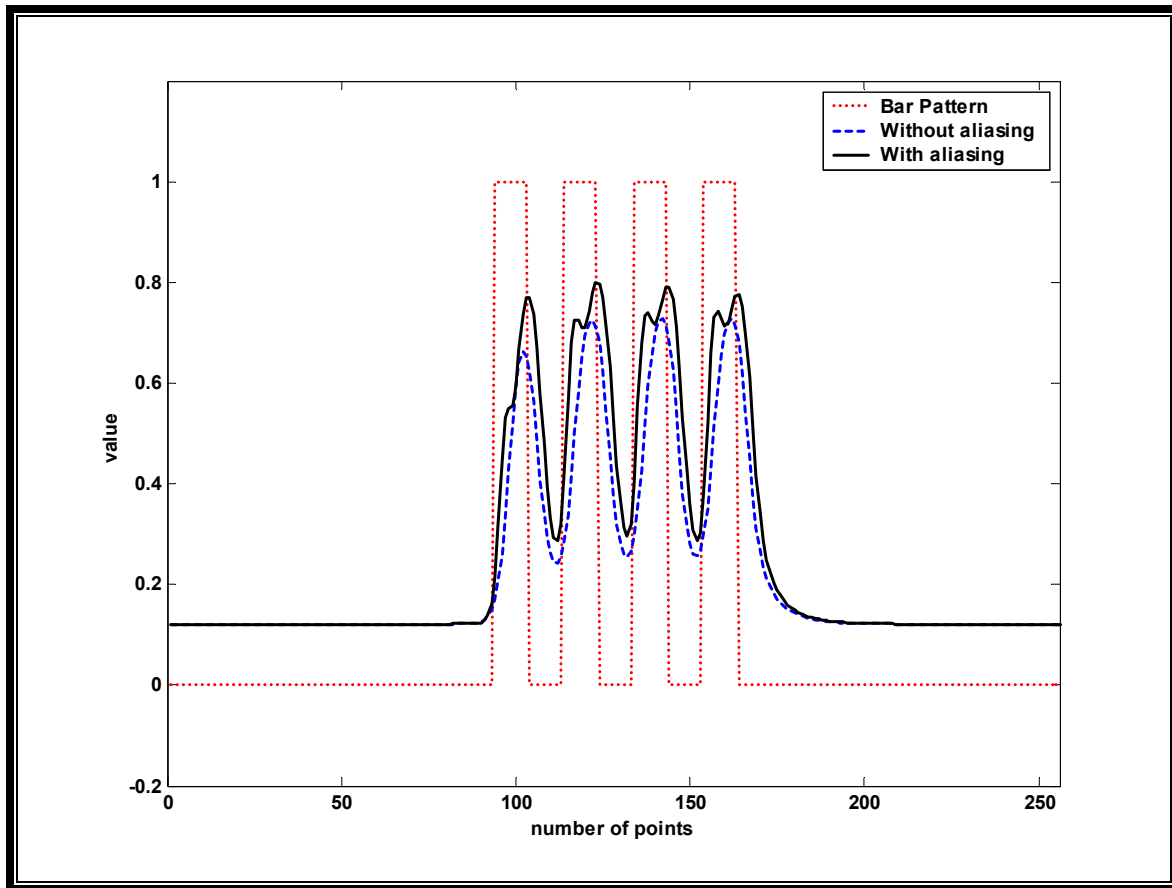
**Figure 7.4.   A Profile across the Target and the Image Centers at 0.65
Cycles/Mrad. Note the Enhancement of Contrast (between 8%-20%) due to
Aliasing.**

B.   ALIASING EFFECTS ABOVE THE NYQUIST LIMIT

To account for aliasing in

modeling thermal imagers, a number of approaches have been proposed up to
now. S.K. Park and R. Hazra accomplished one of the notable works in that area
presenting a quantitative and a qualitative assessment of aliasing as noise. They made a
theoretical and an experimental argument suggesting that aliasing should be treated as
signal-dependant, additive noise [Ref. 26].

91
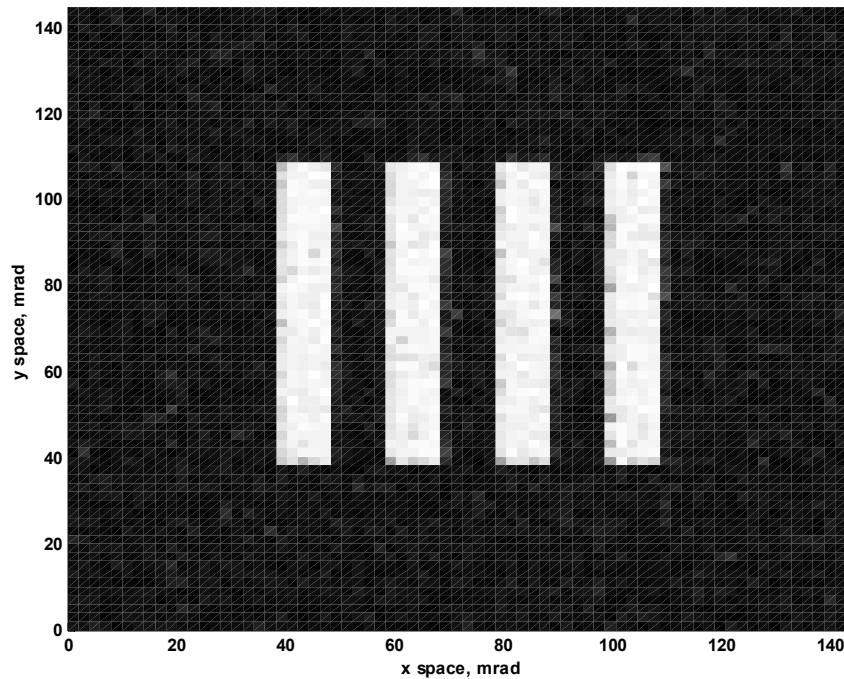
Figure 7.5.   Four-Bar Target Image with Noise and Aliasing At 0.05 Cycles/Mrad: Noise is Dominant at Low Spatial Frequency.

However, observations made in the experiments with the NPS Virtual Thermal Image-Processing model show that aliasing effects manifest themselves in much different manner from noise in the generated images. Figure 7.5 above demonstrates the effects of noise that were observed to be dominant at low four-bar spatial frequencies (0.05 cycles/mrad). The tendency of masking the four-bar pattern was the most notable characteristic of noise as also observed from the figure.

On the other hand, aliasing effects, which become more severe at four-bar spatial frequencies above the Nyquist limit, created distortions in the imagery. Figure 7.6 shows a significant distortion in the imagery for a four-bar spatial frequency of 1.10 cycles/mrad. Therefore the four-bar pattern appears as a three-bar pattern. However, noise alone does not distort the image at the same four-bar spatial frequency; all bars are resolvable as given below in Figure 7.7.

92
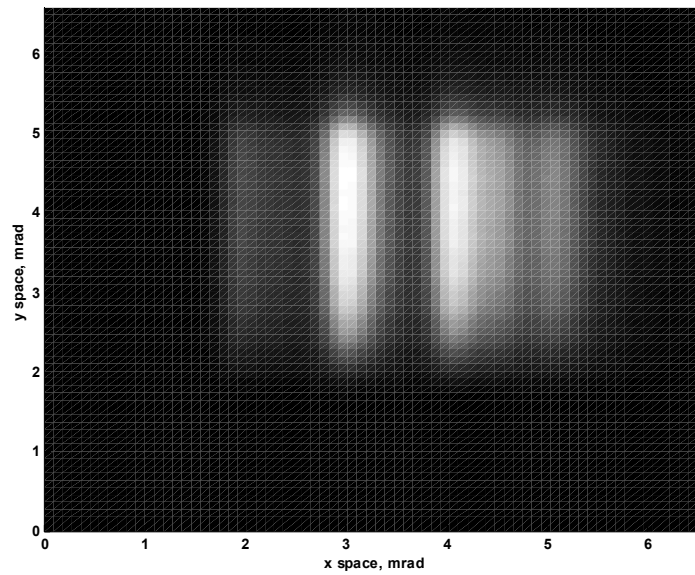
Figure 7.6.   Four-Bar Target Image with Noise and Aliasing At 1.10 Cycles/Mrad: Aliasing is Dominant above the Nyquist Frequency: Note the Distortion.
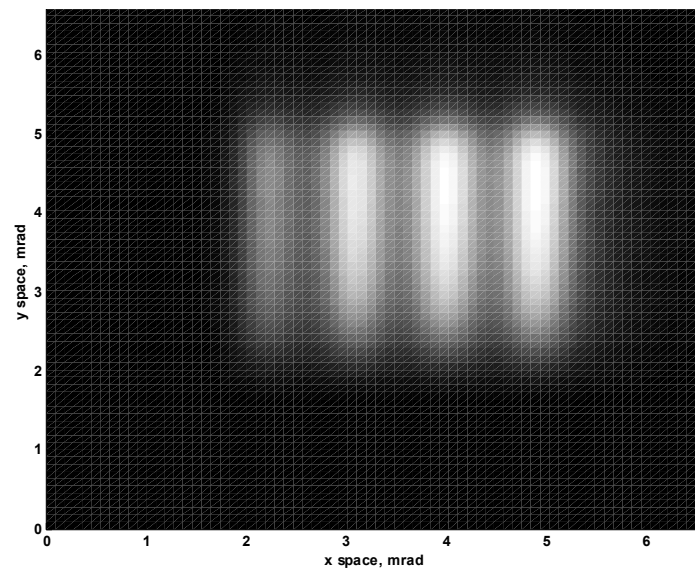
Figure 7.7.   Four-Bar Target Image with Only Noise (No Aliasing) at 1.10 Cycles/Mrad: Noise Alone Does Not Distort the Image.

This analysis indicates that aliasing effects cannot be adequately represented as noise alone.

C.   EXPLORATION OF DISTORTION DUE TO ALIASING

Experiments with the Virtual Thermal Image-Processing model showed that there is a noticeable difference in terms of distortion due to aliasing between the horizontal and the vertical bar pattern images for the same spatial frequency. Figures 7.8 and 7.9 depict the images of the horizontal and the vertical bar patterns at 1.15 cycles/mrad respectively (Nyquist frequency is 0.96 cycles/mrad). The vertical bar pattern image seems to be much more distorted due to aliasing when compared to the horizontal bar pattern image.

Further analysis showed that different sampling frequencies in the horizontal and vertical directions lead to the differences in the level of distortion in the corresponding directions. From the Mitsubishi system parameters, the sampling frequencies were calculated as 1.92 and 2.5 cycles/mrad in the horizontal and the vertical directions respectively. Therefore the replicas of the target spectrum are expected to overlap with the original target spectrum to a greater extend in the horizontal direction because the sampling frequency in that direction is much smaller. At this point, it will be more appropriate to make a spectrum analysis to explain this phenomenon.
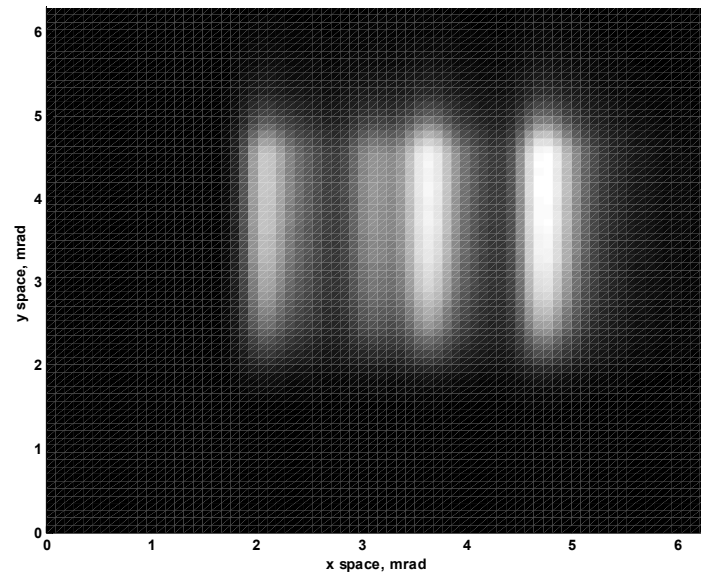
Figure 7.8. **Horizontal Four-Bar Pattern at 1.15 Cycles/Mrad (above Nyquist): Including Aliasing.**
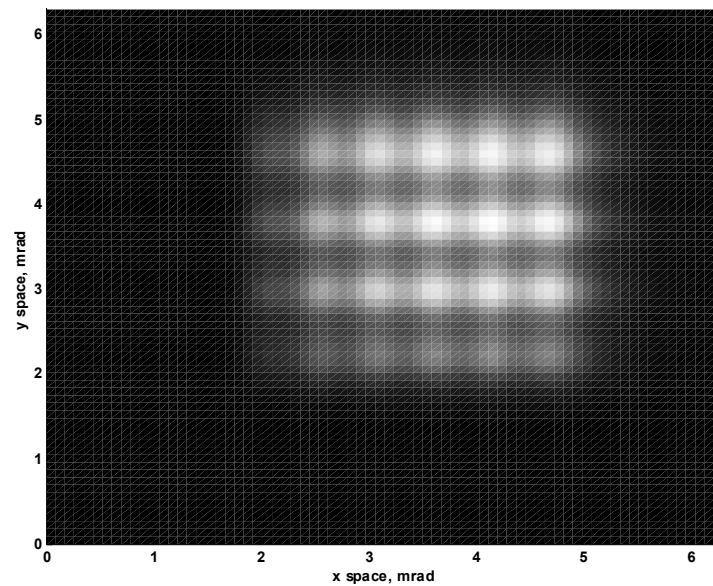
Figure 7.9. **Vertical Four-Bar Pattern at 1.15 Cycles/Mrad: Clear and Even Pattern of Horizontal Bars.**

95

The horizontal four-bar spectra along the x and y directions are given in Figures 7.10 and 7.11 respectively. In both figures, the original target spectrum centered at the origin between the replicas on two sides, demonstrate the degree of overlap due to aliasing. It is significant that the overlap of the spectra along the x-axis is much more when compared to the overlap of the spectra along the y-axis. Since the sampling frequency in each direction is independent of target pattern rotation, stronger aliasing effects still apply along the x-axis for the vertical bar pattern.
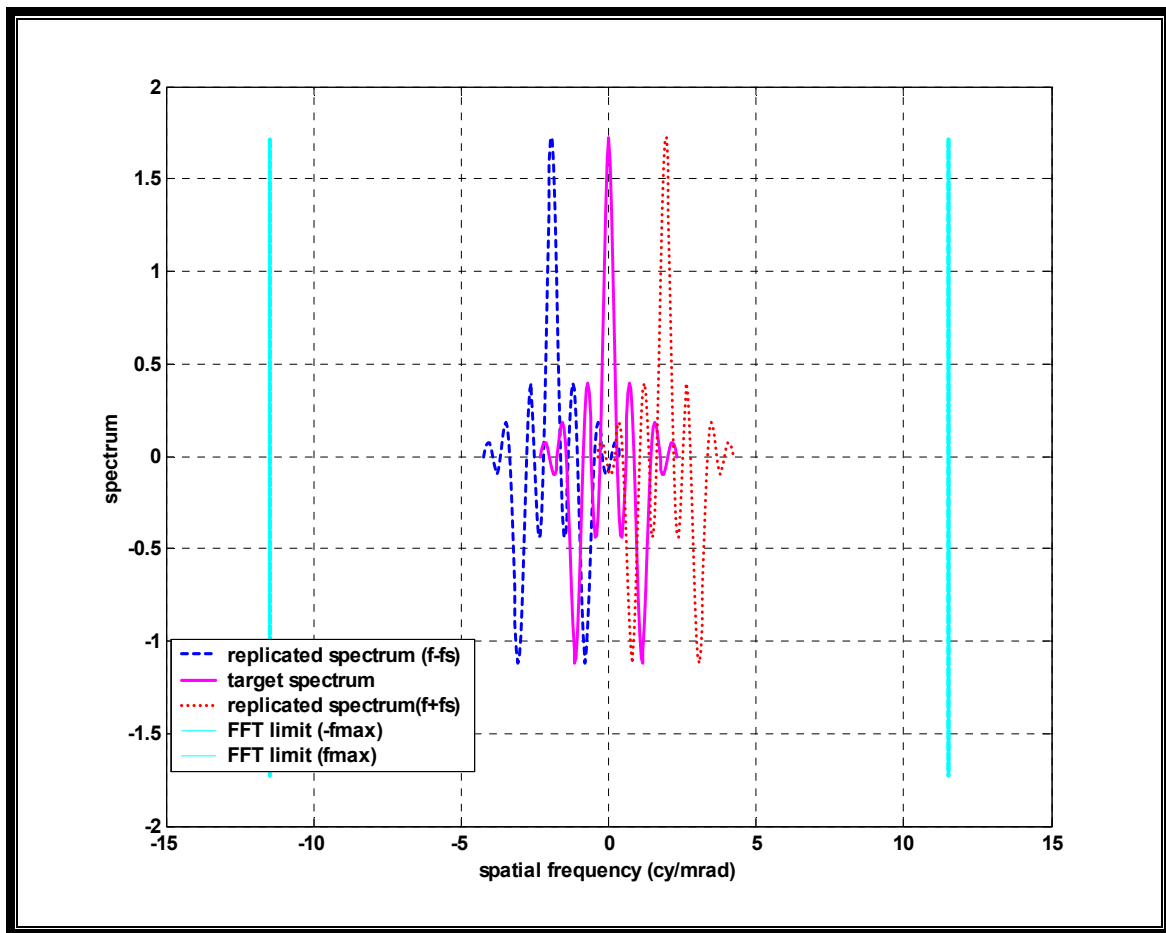
Figure 7.10. Horizontal Four-Bar Spectrum Along X-Axis at 1.15 Cycles/Mrad.

Hence, strong aliasing effects in the horizontal direction make the two bars in the middle appear to merge as in Figure 7.8, while causing the vertical bar pattern appear to be perpendicularly dissected as in Figure 7.9.
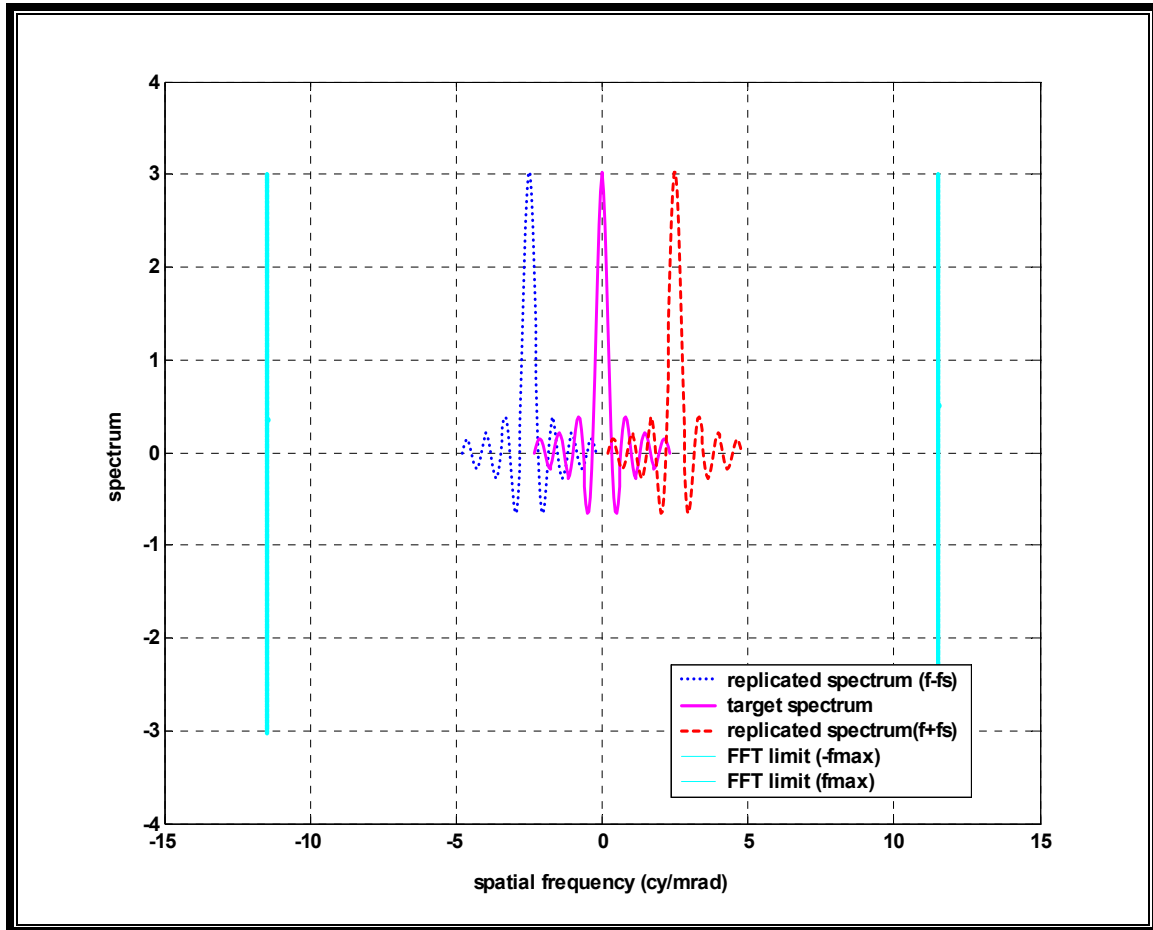
Figure 7.11.   Horizontal Four-Bar Spectrum Along Y-Axis at 1.15 Cycles/Mrad.

The experiments with the Virtual Thermal Image-Processing model also showed the presence of an aliasing pattern that manifests itself as ripples in the produced images. Figure 7.12 below obviously demonstrates this horizontal ripple effect brought about by aliasing in a vertical four-bar image.
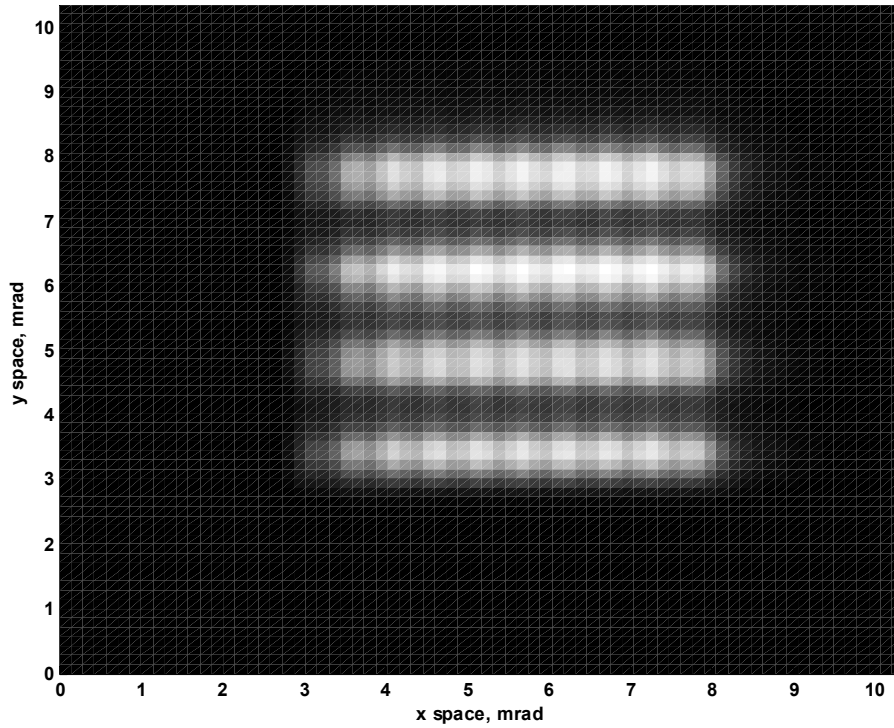
Figure 7.12.   Vertical Four-Bar Image at 0.70 Cycles/Mrad.

In a further analysis the number of ripples present in the patterns brought about by aliasing was counted for all spatial frequencies in the vertical four-bar images. Since the image-reconstruction detector MTF diminishes the ripple effects from the horizontal bar pattern images, only the vertical bar pattern images are used for analysis purposes. A detailed discussion of the image reconstruction detector MTF filtering effects is provided in Appendix H.

The data obtained from the ripple counting process in the aliasing pattern is presented in a tabular form in Appendix I. Figure 7.13 demonstrates two different curves plotted from this data. The upper curve in the figure illustrates the number of ripples versus bar spatial frequency relationship, while the lower curve confirms that the aliasing pattern stays almost steady independent of the bar spatial frequency in all produced images.
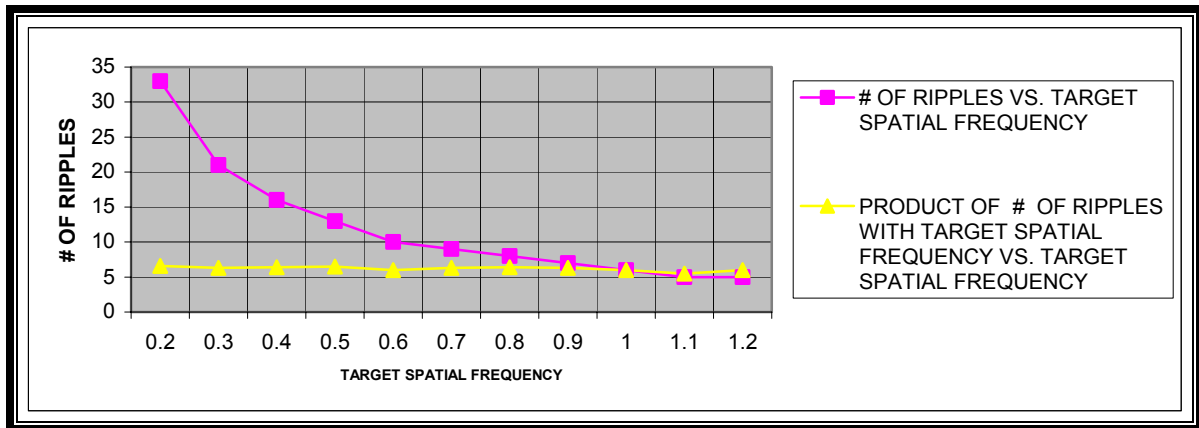
Figure 7.13.   Aliasing Pattern Analysis Results.

At this point a similar analysis showed that there is a reasonable correlation between the modeled system's (Mitsubishi) sampling frequency and the number of ripples in the aliasing pattern images. Figure 7.14 graphically illustrates the data obtained from this analysis. The complete set of data is provided in Appendix J. This figure verifies how close the sampling frequency can be derived from the aliasing pattern present in all virtual images utilizing a ripple analysis. In other words, the ripple effect brought by aliasing into the thermal images is a function of the spatial sampling frequency due to the detector array.
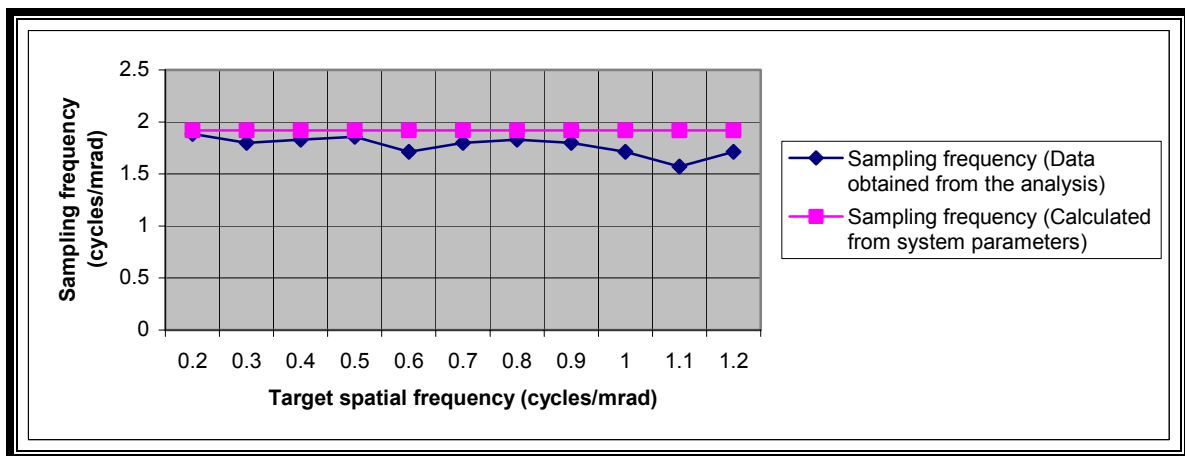
Figure 7.14.   Comparison of the Sampling Frequency Results Obtained from the Analysis to the Sampling Frequency of the Modeled System.

D. ELECTRONICS PTF EFFECTS

In this subsection the electronics PTF effects will be examined and compared to the aliasing effects in the generated images. Figures 7.15 and 7.16 show the horizontal four-bar images without the electronics PTF effects at 1.15 cycles/mrad including and excluding aliasing effects respectively. The net result of aliasing as visually observed is that the two bars in the middle seem to merge into a wider bar. The two bars are no longer present at their expected locations in the image and the four-bar pattern appears as a three-bar pattern. Figure 7.17 gives the plot of a profile passed across the image and shows the deterioration of the symmetry and also the shift in the locations of the two bars in the middle due to aliasing effects.
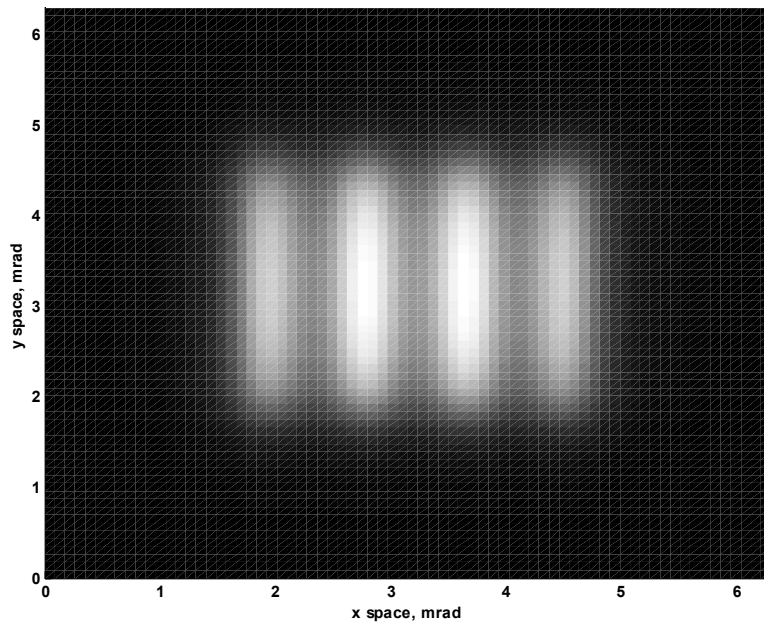
Figure 7.15.   Horizontal Four-Bar Image without Aliasing and without Electronics PTF at 1.15 Cycles/mrad.
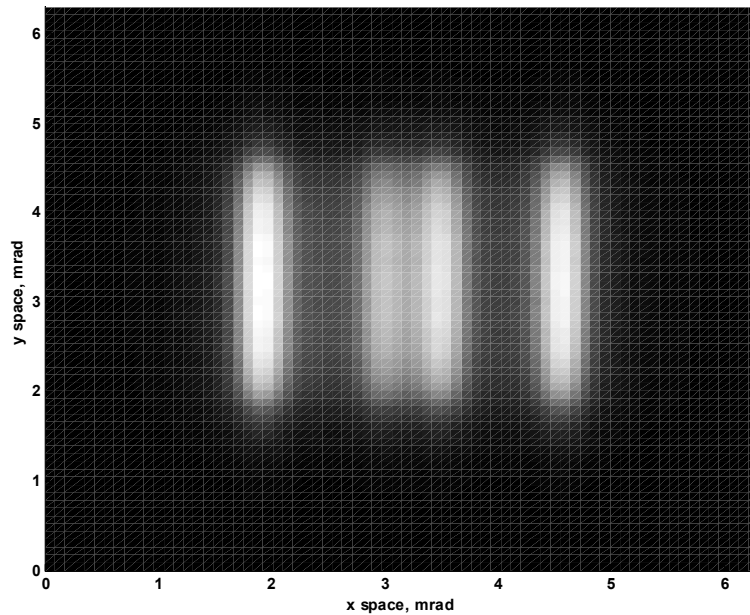
Figure 7.16   Horizontal Four-Bar Image with Aliasing and without Electronics PTF at 1.15 Cycles/mrad. Aliasing Distorts the Symmetry of the Image.
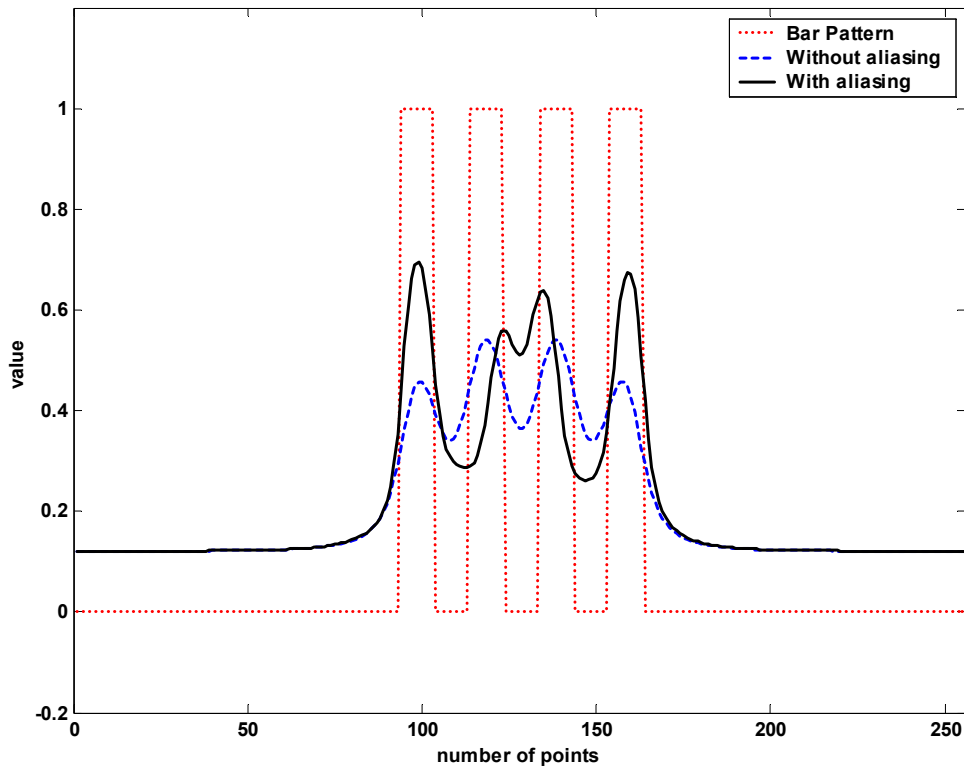
Figure 7.17. A Profile across the Horizontal Four-Bar Pattern without Electronics PTF at 1.15 Cycles/mrad. Compare with Figures 7.15 and 7.16.

The following Figures 7.18 and 7.19 illustrate the horizontal four-bar images with the electronics PTF effects at 1.15 cycles/mrad including and excluding aliasing effects respectively. The net result of electronics PTF is noticeable as degradation in contrast on the leftmost bar. Figure 7.20 gives the plot of a profile passed across the image and shows the contrast degradation on the leftmost bar and the deterioration of the symmetry in the four-bar pattern due to electronics PTF effects. The entire pattern is shifted in the "down-scan", or later time direction.
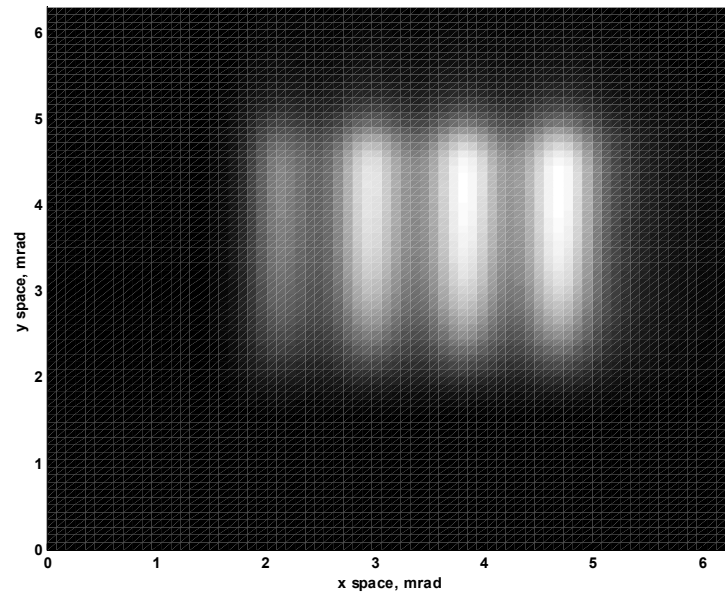
Figure 7.18.   Horizontal Four-Bar Image without Aliasing and with Electronics PTF at 1.15 Cycles/mrad.
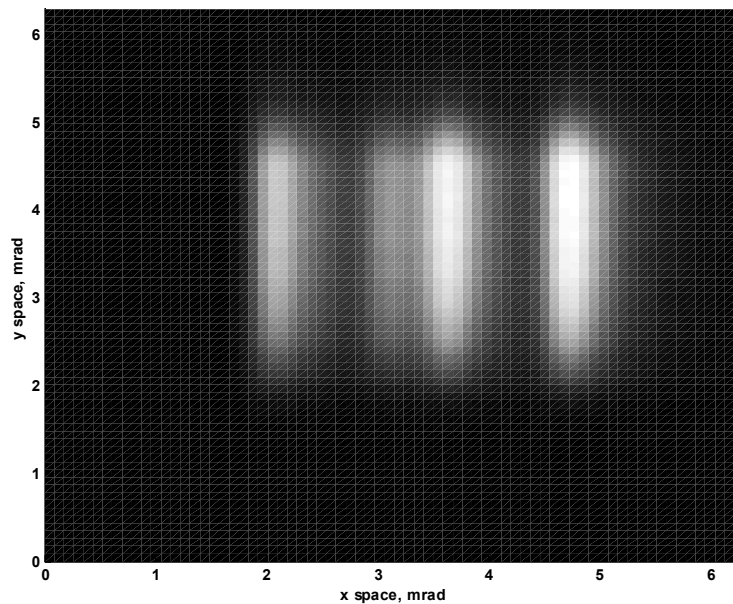
Figure 7.19.   Horizontal Four-Bar Image with Aliasing and with Electronics PTF at 1.15 Cycles/mrad. Compare with 7.16. PTF Introduces no Apparent Change in the Symmetry.
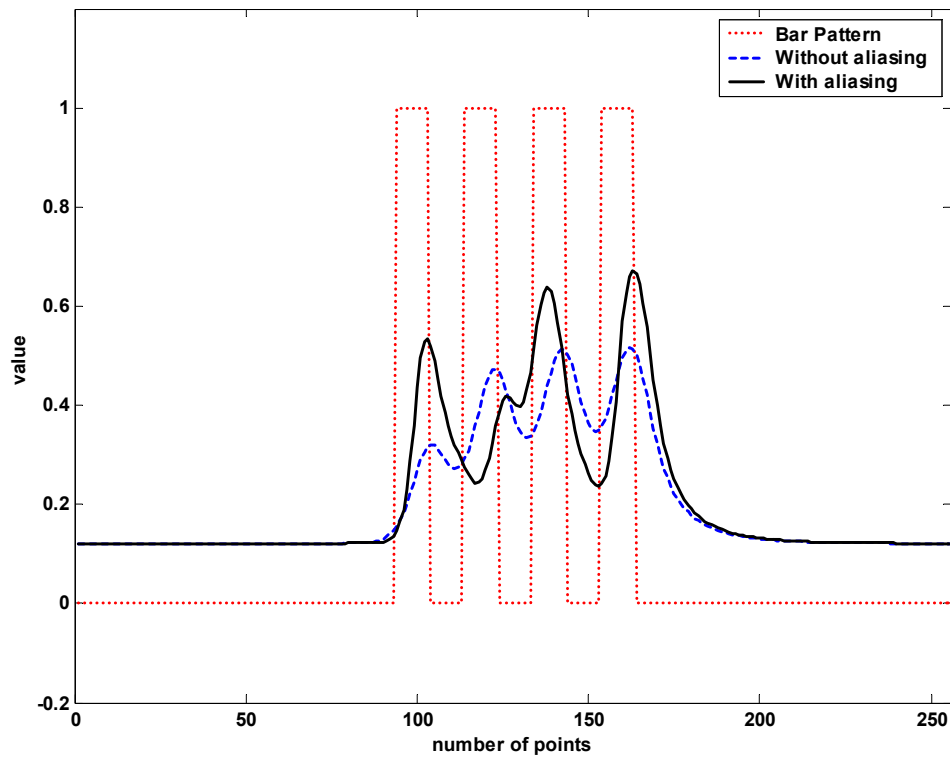
Figure 7.20.   A Profile across the Horizontal Four-Bar Pattern with Electronics PTF at 1.15 Cycles/mrad. Compare with Figure 7.17.

E.   CONCLUSIONS

The results obtained from the experiments with the Virtual Thermal Image-Processing model indicated several important conclusions.

- Aliasing effects are present in the four-bar pattern images at spatial frequencies below the Nyquist limit. Thus modeling aliasing effects should be reconsidered for this frequency region as well as above Nyquist.

- Aliasing can have a significant visual enhancing effect at bar spatial frequencies less than the Nyquist limit

- Aliasing effects cannot be adequately represented as noise alone

- Thermal imaging devices employing different sampling frequencies in horizontal and vertical directions experience stronger distortion effects due to aliasing in the direction where sampling frequency is much smaller

- Aliasing pattern manifesting itself as ripples stays steady independent of the bar spatial frequency in all output images

- The ripple effect introduced by aliasing into the thermal imagery is a function of spatial sampling frequency

- System electronics PTF shows its effect as contrast degradation and deterioration of symmetry that results in the shift of the bar locations

This work and its conclusions are also summarized in a paper. The preprint of this paper, which is accepted for presentation at the 35th Asilomar Conference on Signals, Systems, and Computers on November 4 – November 7, 2001 is provided in Appendix K.

F.   DIRECTIONS FOR FURTHER RESEARCH

Experiments with the Virtual Thermal Image-Processing model have revealed several advantages of its operation while bringing almost endless further research opportunities. From these, a few significant topics will be pointed out as directions for future studies.

First, the Virtual Thermal Image-Processing model can be improved in several ways. The current version produces four-bar thermal images without taking into account the MRTD predictions. The model should be applied in the future to predict subjective MRTD from the virtual images.

Second, the model currently creates thermal images of only horizontal and vertical bar patterns. In the future it should be able to produce the images of rotated bar patterns at any angles.

Third, the Virtual Thermal Image-Processing model simulates thermal imaging systems based on the subjective MRTD measurement scheme. Ultimately, the observer decides whether the bars are resolved or not in the model created images. However the model could have a version based on the objective MRTD measurement scheme that leaves the observer and the display out of the loop. Therefore the model could be used to simulate an ATR device.

Fourth, the model could include a more complete display MTF employing separate MTFs in the horizontal and vertical dimensions for a more accurate simulation of the thermal imaging systems.

Fifth, the current model creates the input target pattern only once and then appropriately scales it for various bar spatial frequencies. However, all four-bar patterns in the output images seem to have the same physical size although they show different scales. To correctly present the bar patterns to the observer with respect to their actual sizes, the model could create an individual input target pattern for each single bar spatial frequency.

Finally, the Virtual Thermal Image-Processing model could take advantage of a more user-friendly interface and more efficient program coding.

APPENDIX A. FLIR-92 SUB-SYSTEM MTF EQUATIONS [REF. 2]

A. PRE-FILTER MTFS

(a) Optics MTFs:

(1) Diffraction-limited MTF

$$H_{ODL}(f_S) = \left(\frac{2}{\pi}\right)\left[a\cos(\frac{\lambda f_S}{D_O}) - (\frac{\lambda f_S}{D_O})\left[1 - (\frac{\lambda f_S}{D_O})^2\right]^{0.5}\right] \quad \text{(A.1)}$$

(2) Geometric Blur MTF

$$H_{OGB}(f_S) = e^{(-2\pi^2\sigma^2 f_S^2)} \quad \text{(A.2)}$$

(b) Detector Spatial MTF:

$$H_{DS}(f_S) = \frac{\sin(\pi\delta_z f_S)}{(\pi\delta_z f_S)} \quad \text{(A.3)}$$

(c) Focal Plane Array Integration MTF:

$$H_{DI}(f_S) = \frac{\sin(\pi f_T v_S t_I)}{(\pi f_T v_S t_I)} \quad \text{(A.4)}$$

(d) Sample-scene Phase MTF:

$$H_{SSP}(f_S) = [\cos\left(\frac{f_S}{r_N}\right)\Theta_Z] \quad \text{(A.5)}$$

(e) Image Motion MTFs:

(1) Linear Image Motion MTF

$$H_{ML}(f_S) = \frac{\sin(\pi f_S v_R t_I)}{(\pi f_S v_R t_I)}$$

(A.6)

(2) Random Image Motion MTF

$$H_{MR}(f_S) = e^{(-2\pi^2 \sigma^2 f_S^2)}$$

(A.7)

(3) Sinusoidal Image Motion MTF

$$H_{MS}(f_S) = J_0(2\pi A f_S)$$

(A.8)

B.   TEMPORAL POST-FILTER MTFS

(a)   Detector Temporal MTFs:

$$H_{DT}(f_T) = \left(1 + \left(\frac{f_T}{f_{DT}}\right)^2\right)^{-1/2}$$

(A.9)

(b)   Electronics Low Frequency Response:

$$H_{ELP}(f_T) = \left(1 + \left(\frac{f_T}{f_{ELP}}\right)^{2n}\right)^{-1/2}$$

(A.10)

(c)   Electronics High Frequency Response:

$$H_{EHP}(f_T) = \left(\left(\frac{f_T}{f_{EHP}}\right)^n \bigg/ \left(1 + \left(\frac{f_T}{f_{EHP}}\right)^{2n}\right)\right)^{0.5}$$

(A.11)

(d)   Boosting MTF:

$$H_{EB}(f_T) = 1 + \left[\frac{(B_A - 1)}{2\left(1 - \cos\left(\frac{\pi f_T}{f_B}\right)\right)}\right]$$

(A.12)

C. SPATIAL POST-FILTER MTFS

(a)   Electro-optical Multiplexor MTF:

$$H_{MUX}(f_S) = \frac{\sin(\pi \delta_{led} f_S)}{(\pi \delta_{led} f_S)} \tag{A.13}$$

(b)   Digital Filter MTF:

$$H_{DIG}(f_S) = \sum_{i=0}^{(N-1)/2} a_i \cos\left(\frac{2\pi i f_S}{f_{CO}}\right) \tag{A.14}$$

$$H_{DIG}(f_S) = \sum_{i=1}^{N/2} a_i \cos\left(\frac{2\pi(i-\frac{1}{2})f_S}{f_{CO}}\right) \tag{A.15}$$

(c)   CRT Display MTF:

$$H_{CRT}(f_S) = e^{(-2\pi^2\sigma^2 f_S^2)} \tag{A.16}$$

$$\sigma = \left[\frac{-\log 0.025}{2\pi^2\left(\frac{N_r}{\beta}\right)^2}\right]^{0.5} \tag{A.17}$$

(1)   CCD Charge Transfer Efficiency MTF:

$$H_{ccd}(f_S) = e^{[-N(1-\varepsilon)(1-\cos(2\pi f_S/r_N))]} \tag{A.18}$$

(2)   Display Sample and Hold MTF:

$$H_{DSH}(f_S) = \frac{\sin(\pi \delta_S f_S)}{(\pi \delta_S f_S)} \tag{A.19}$$

(d)   Eye MTF:

      (1) Non-limiting Eye MTF

$$H_{EYE}(f_S) = 1.0 \tag{A.20}$$

      (2) Limiting Eye MTF

$$H_{EYE}(f_S) = e^{\left(\frac{\Gamma f_S}{2M}\right)} \tag{A.21}$$

APPENDIX B. DIRECTIONAL AVERAGING OPERATOR [REF. 2]

The 3-D noise concept utilizes an averaging process to isolate the noise components in the desired directions using the directional averaging operators: D_T, D_H and D_V. Subscripts of these operators refer to the directions in which the averaging operation is applied. Each D operator has the classical simple averaging effect in the calculations. The original three-dimensional image data set, which contains the complex noise components, is represented by U(T,V,H).

The three important properties of the D operators are:

a.   Commutative Property:
      $D_V D_H \{U(T,V,H)\} = D_H D_V \{U(T,V,H)\}$
b.   Distributive Property:
      $D_V \{U(T,V,H) + V(T,V,H)\} = D_V \{U(T,V,H)\} + D_V \{V(T,V,H)\}$
c.   Idem-potent Property:
      $D_V D_V \{U(T,V,H)\} = D_V \{U(T,V,H)\}$

In order to extract the desired noise component from the composite noise data set U (T, V, H), the appropriate directional averaging operators should be used as shown in the table below.

NOISE TERM	CORRESPONDING DIRECTIONAL OPERATION REQUIRED
N_{TVH}	$[(1-D_T)(1-D_V)(1-D_H)] \{U(T,V,H)\}$
N_{VH}	$[(D_T)(1-D_V)(1-D_H)] \{U(T,V,H)\}$
N_{TV}	$[(1-D_T)(1-D_V)(D_H)] \{U(T,V,H)\}$
N_V	$[(D_T)(1-D_V)(D_H)] \{U(T,V,H)\}$
N_{TH}	$[(1-D_T)(D_V)(1-D_H)] \{U(T,V,H)\}$
N_H	$[(D_T)(D_V)(1-D_H)] \{U(T,V,H)\}$
N_T	$[(1-D_T)(D_V)(D_H)] \{U(T,V,H)\}$
S	$[(D_T)(D_V)(D_H)] \{U(T,V,H)\}$

Table B.1.   The Use of D Operators [Ref. 2].

The D operator has the effect of deleting the selected data types from the original composite set. On the other hand the operations $(1-D_T)$, $(1-D_V)$, and $(1-D_H)$ have the opposite effect. They extract the desired noise components from the original composite data. For example, the operation $[(D_T)(1-D_V)(D_H)]\{U(T,V,H)\}$ indicates that the desired component to be extracted from the composite data is the vertical noise component because the D_T and D_H operators remove the components in the horizontal and temporal directions while the $(1-D_V)$ operation extracts the desired vertical noise component. The applications of each directional operator are also presented in the following table.

APPLIED OPERATION	DELETES	EXTRACTS
(D_T)	$N_T , N_{TVH} , N_{TH} , N_{TV}$	S , N_H , N_{VH} , N_V
$(1-D_T)$	S , N_H , N_{VH} , N_V	$N_T , N_{TVH} , N_{TH} , N_{TV}$
(D_H)	$N_{TH} , N_H , N_{VH} , N_{TVH}$	S , N_T , N_V , N_{TV}
$(1-D_H)$	S , N_T , N_V , N_{TV}	$N_{TH} , N_H , N_{VH} , N_{TVH}$
(D_V)	$N_{TVH} , N_V , N_{HV} , N_{TV}$	S , N_H , N_T , N_{TH}
$(1-D_v)$	S , N_H , N_T , N_{TH}	$N_{TVH} , N_V , N_{HV} , N_{TV}$

Table B.2.   The Applications of Directional Averaging Operations.

APPENDIX C. EYE-BRAIN SPATIAL INTEGRATION FACTORS FOR MRTD PREDICTIONS [REF. 2]

A.   SCANNING SYSTEMS

■ The horizontal eye-brain integration function in the horizontal direction is calculated as:

$$E_{H_H}(f_S) = \frac{v_S}{\Delta f_P}\left[\int_0^\alpha S(v)H_{NF_H}^2(v)\left[\frac{\sin\left(\frac{\pi v}{2f_S}\right)}{\frac{\pi v}{2f_S}}\right]^2 dv\right] \qquad (C.1)$$

■ The vertical eye-brain integration function in the horizontal direction is calculated as:

$$E_{V_H}(f_S) = \frac{\delta_V}{s_V}\left[\int_{-\alpha}^\alpha H_{NF_V}^2(v)\left[\frac{\sin\left(\frac{7\pi v}{2f_S}\right)}{\frac{7\pi v}{2f_S}}\right]^2 dv\right] \qquad (C.2)$$

■ The horizontal eye-brain integration function in the vertical direction is calculated as:

$$E_{H_V}(f_S) = \frac{v_S}{\Delta f_P}\left[\int_0^\alpha S(v)H_{NF_H}^2(v)\left[\frac{\sin\left(\frac{7\pi v}{2f_S}\right)}{\frac{7\pi v}{2f_S}}\right]^2 dv\right] \qquad (C.3)$$

■ The vertical eye-brain integration function in the vertical direction is calculated as:

$$E_{V_V}(f_S) = \frac{\delta_V}{s_V}\left[\int_{-\alpha}^\alpha H_{NF_V}^2(v)\left[\frac{\sin\left(\frac{\pi v}{2f_S}\right)}{\frac{\pi v}{2f_S}}\right]^2 dv\right] \qquad (C.4)$$

■ The parameters used in Equation (C.1) through Equation (C.4) are described in the table below.

PARAMETER	DESCRIPTION	UNITS
V_S	Scan velocity	mrad/s
Δf_P	System noise bandwidth	Hz
$S(v)$	Detector noise power spectrum	--
δ_V	Detector vertical instantaneous field of view (IFOV)	mrad
s_V	Samples per detector vertical IFOV	--
$H_{NFH}(v)$	Horizontal system noise filter MTF	--
$H_{NFV}(v)$	Vertical system noise filter MTF	--

Table C.1.   Eye-Brain Integration Factor Parameters for Scanning Systems.

B.   STARING SYSTEMS

■ The horizontal eye-brain integration function in the horizontal direction is calculated as:

$$E_{H_H}(f_S) = \frac{\delta_H}{S_H}\left[\int_{-\alpha}^{\alpha} H_{NF_H}^2(v)\left[\frac{\sin\left(\frac{\pi v}{2f_S}\right)}{\frac{\pi v}{2f_S}}\right]^2 dv\right] \tag{C.5}$$

■ The vertical eye-brain integration function in the horizontal direction is calculated as:

$$E_{V_H}(f_S) = \frac{\delta_V}{s_V}\left[\int_{-\alpha}^{\alpha} H_{NF_V}^2(v)\left[\frac{\sin\left(\frac{7\pi v}{2f_S}\right)}{\frac{7\pi v}{2f_S}}\right]^2 dv\right] \tag{C.6}$$

114

■ The horizontal eye-brain integration function in the vertical direction is calculated as:

$$E_{H_V}(f_S) = \frac{\delta_H}{s_H} \left[\int_{-\alpha}^{\alpha} H_{NF_H}^2(v) \left[\frac{\sin\left(\frac{7\pi v}{2f_S}\right)}{\frac{7\pi v}{2f_S}} \right]^2 dv \right] \tag{C.7}$$

■ The vertical eye-brain integration function in the vertical direction is calculated as:

$$E_{V_V}(f_S) = \frac{\delta_V}{s_V} \left[\int_{-\alpha}^{\alpha} H_{NF_V}^2(v) \left[\frac{\sin\left(\frac{\pi v}{2f_S}\right)}{\frac{\pi v}{2f_S}} \right]^2 dv \right] \tag{C.8}$$

■ The parameters used in Equation (C.5) through Equation (C.8) are described in the table below.

PARAMETER	DESCRIPTION	UNITS
δ_H	Detector horizontal instantaneous field of view (IFOV)	mrad/sec
s_H	Samples per detector horizontal IFOV	--
δ_V	Detector vertical instantaneous field of view (IFOV)	mrad
s_V	Samples per detector vertical IFOV	--
$H_{NFH}(v)$	Horizontal system noise filter MTF	--
$H_{NFV}(v)$	Vertical system noise filter MTF	--

Table C.2.   Eye-Brain Integration Factor Parameters for Staring Systems.

THIS PAGE INTENTIONALLY LEFT BLANK

APPENDIX D. THE MITSUBISHI ELECTRONICS IR-M500 THERMAL IMAGING SYSTEM PARAMETERS

In the subjective and objective MRTD laboratory measurements only the Mitsubishi Electronics IR-M500 thermal imager was used. Therefore the same thermal imaging system was simulated in the Visibility, the FLIR-92 and the Virtual Thermal Image-Processing models utilizing the system parameters as given below in Table D.1.

Number of horizontal detectors	512
Number of vertical detectors	512
Detector horizontal dimension	26μm
Detector vertical dimension	20μm
Detector horizontal active dimension	16.24μm
Detector vertical active dimension	12.49μm
D^*	$5 \times 10^{10} cmHz^{0.5}/watt$
Frame rate	60Hz
Spectral cut-on	3μm
Spectral cut-off	5μm
F/number	1.4
Focal length (optics)	5cm
Transmittance of optics	0.95
Active CRT lines	480
3-D noise level	Moderate
Display brightness	10mL
Schottky barrier height	22eV
PtSi emission coefficient	$0.16\ eV^{-1}$
Integration time	16145.833
BLIP performance	Yes

Table D.1.   Mitsubishi Electronics IR-M500 Thermal Imager System Parameters [Refs .19 and 24].

THIS PAGE INTENTIONALLY LEFT BLANK

APPENDIX E. MRTD MEASUREMENT RESULTS

A.   SUBJECTIVE MRTD MEASUREMENT RESULTS

Spatial frequency (cycles/mrad)	Heat-up MRTD results (degrees C)	Cool-down MRTD results (degrees C)	Average MRTD results (degrees C)
0.06	0.11	0.06	0.08
0.09	0.22	0.06	0.14
0.12	0.28	0.11	0.19
0.15	0.28	0.17	0.22
0.18	0.28	0.17	0.22
0.24	0.33	0.22	0.28
0.29	0.39	0.28	0.33
0.35	0.44	0.33	0.39
0.46	0.50	0.33	0.42
0.56	0.56	0.39	0.47
0.72	0.72	0.50	0.61
0.79	0.83	0.72	0.78
0.88	1.06	0.83	0.94
1.13	2.06	1.00	1.53
1.17	2.83	2.83	2.83
1.21	8.00	6.78	7.39

Table E.1.   Horizontal MRTD Measurement Results.

Spatial frequency (cycles/mrad)	Heat-up MRTD results (degrees C)	Cool-down MRTD results (degrees C)	Average MRTD results (degrees C)
0.06	0.21	0.09	0.15
0.09	0.29	0.21	0.25
0.12	0.29	0.21	0.25
0.15	0.40	0.30	0.35
0.18	0.42	0.38	0.40
0.24	0.61	0.50	0.55
0.29	0.68	0.53	0.65
0.35	0.74	0.66	0.70
0.46	0.76	0.75	0.75
0.56	1.40	1.10	1.25
0.72	4.25	3.05	3.65
0.79	6.20	4.60	5.40
0.88	10.40	7.40	8.90
1.13	24.00	16.00	20.00

Table E.2.   Vertical MRTD Measurement Results.
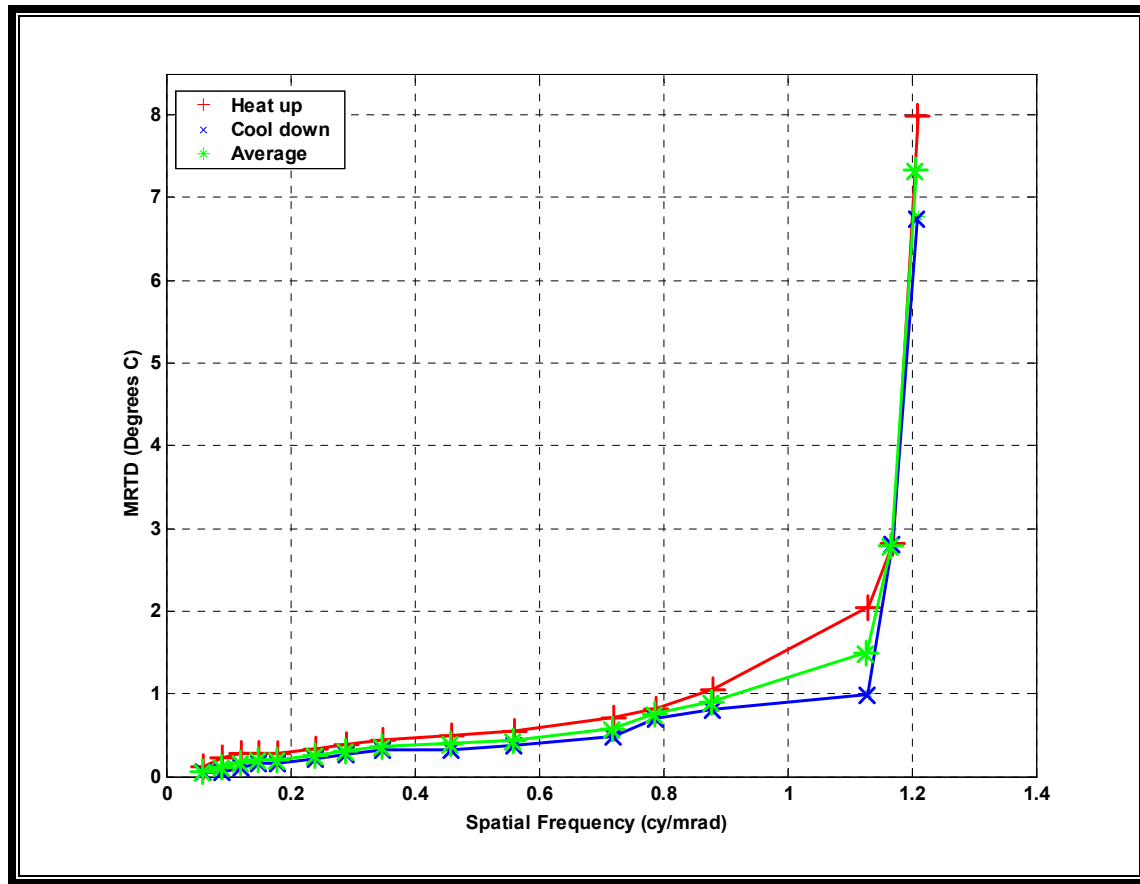
Figure E.1.   Horizontal MRTD Measurement Results.
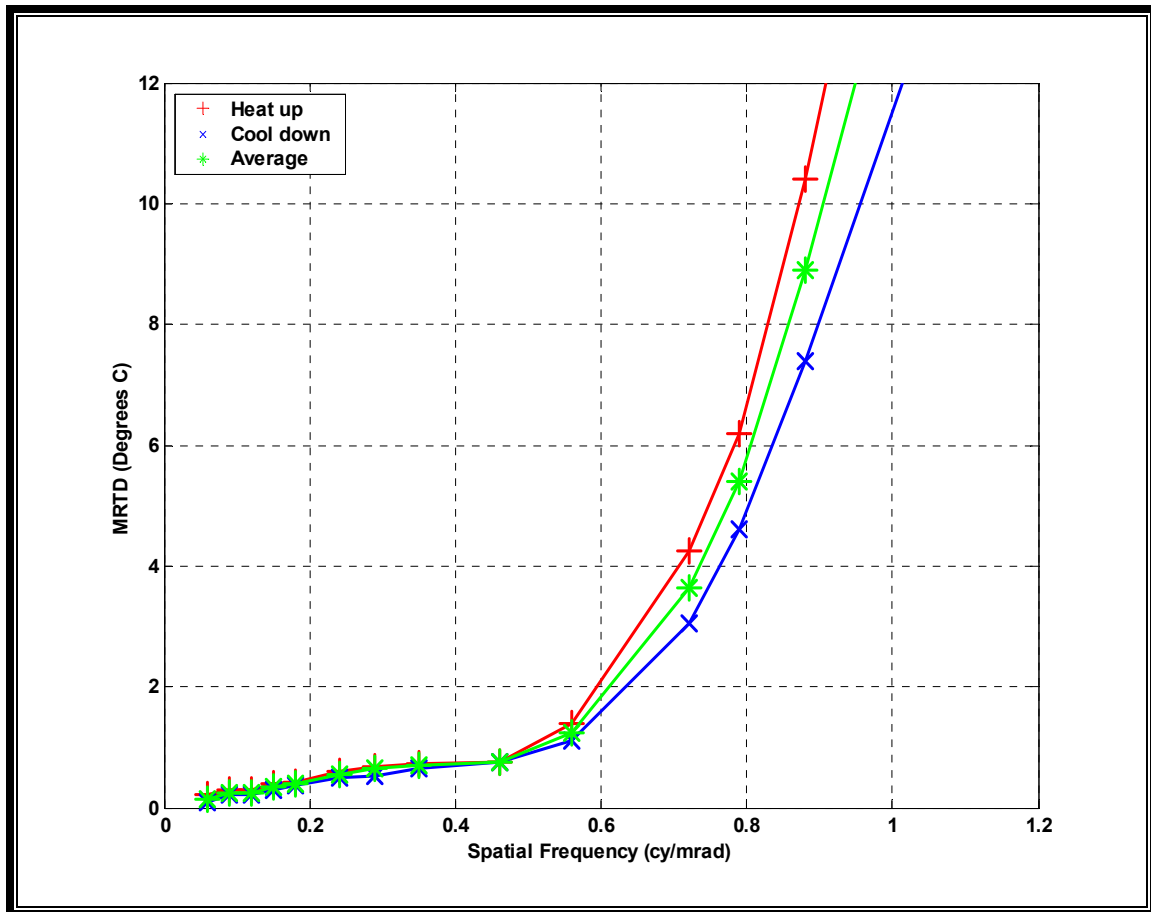
Figure E.2.   Vertical MRTD Measurement Results.

Spatial Frequency (cycles/mrad)	Horizontal MRTD (degrees C)	Vertical MRTD (degrees C)	2-D MRTD (degrees C)
0.06	0.08	0.15	0.1095
0.09	0.14	0.25	0.1871
0.12	0.19	0.25	0.2179
0.15	0.22	0.35	0.2775
0.18	0.22	0.40	0.2966
0.24	0.28	0.55	0.3924
0.29	0.33	0.65	0.4631
0.35	0.39	0.70	0.5225
0.46	0.42	0.75	0.5612
0.56	0.47	1.25	0.7665
0.72	0.61	3.65	1.4921
0.79	0.78	5.40	2.0523
0.88	0.94	8.90	2.8924
1.13	1.53	20.00	5.5317

Table E.3.   Average of the MRTD Measurement Results.

B.   OBJECTIVE MRTD MEASUREMENT RESULTS

Spatial frequency (cycles/mrad)	MRTD (degrees C)
0.06	1.33
0.12	1.50
0.24	1.72
0.35	2.06
0.46	2.39
0.56	2.83

Table E.4.   MRTD Results for SNR of 6.0 (Constant SNR Case).

SNR	Constant spatial frequency (cycles/mrad)			
	0.12	0.24	0.46	0.56
2.0	0.17	0.44	0.78	1.00
3.0	0.39	0.72	1.33	1.44
4.0	0.94	1.11	1.72	1.83
5.0	1.22	1.39	2.17	2.28
6.0	1.56	1.78	2.44	2.89

Table E.5.   MRTD Results for Constant Spatial Frequency Case.

THIS PAGE INTENTIONALLY LEFT BLANK

APPENDIX F. VISIBILITY AND FLIR-92 MODEL MRTD PREDICTIONS
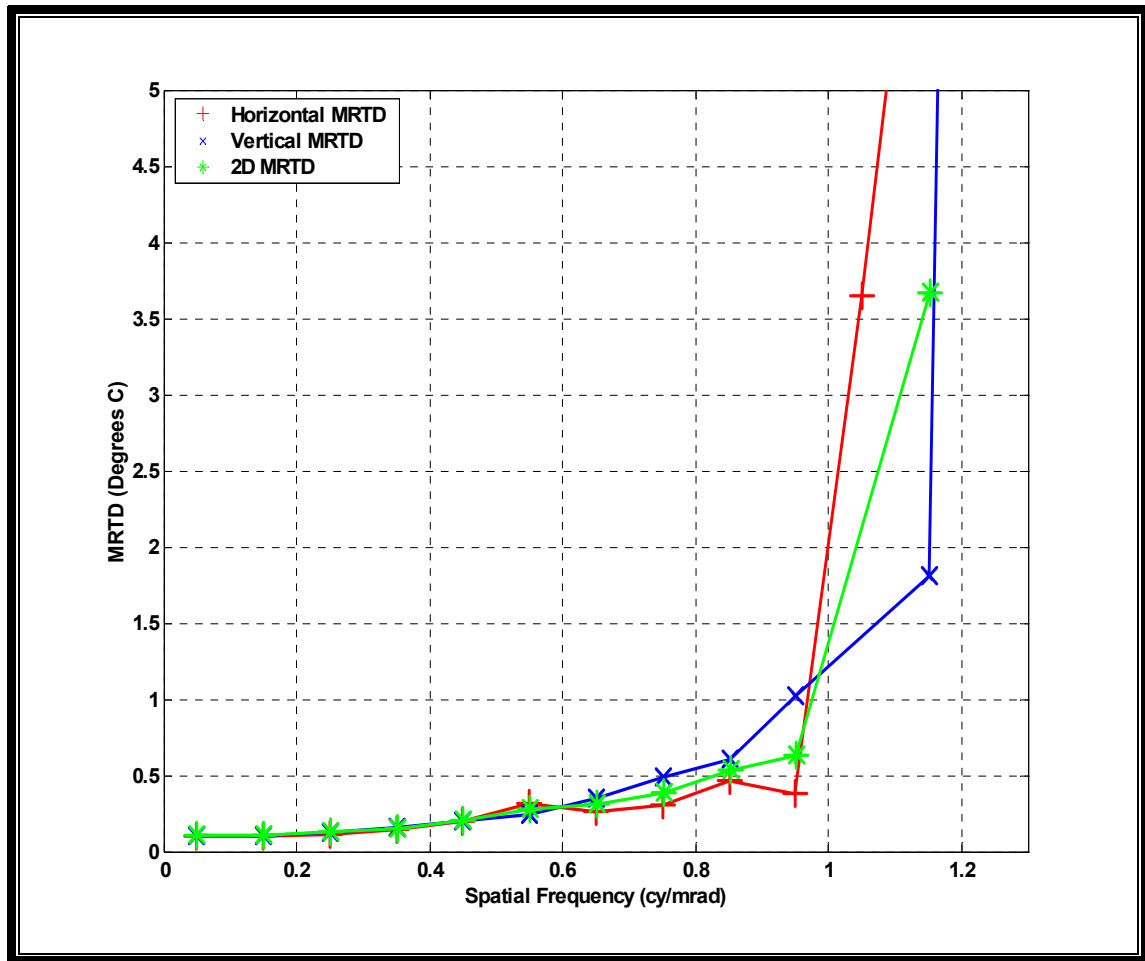
Figure F.1.   Visibility Model Subjective MRTD Predictions.
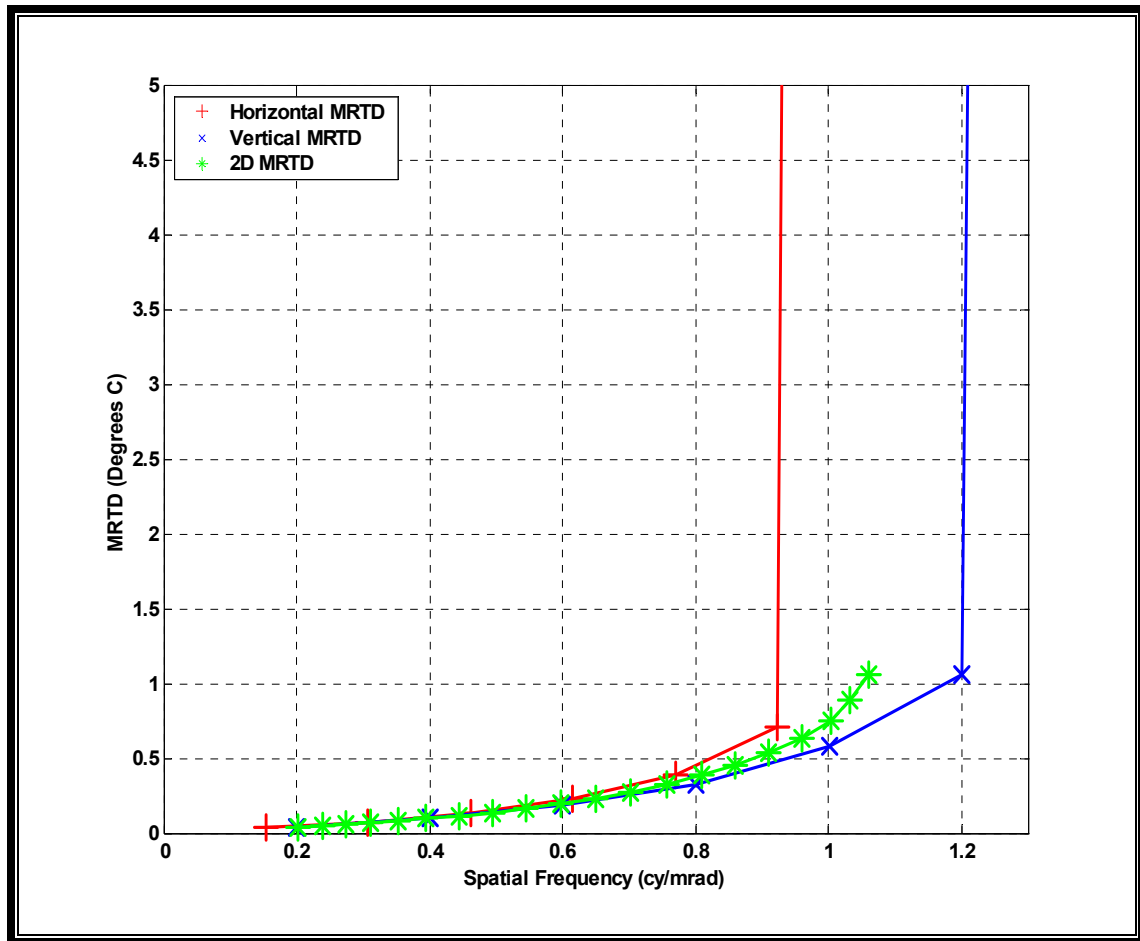
Figure F.2.   FLIR-92 Model MRTD Predictions.
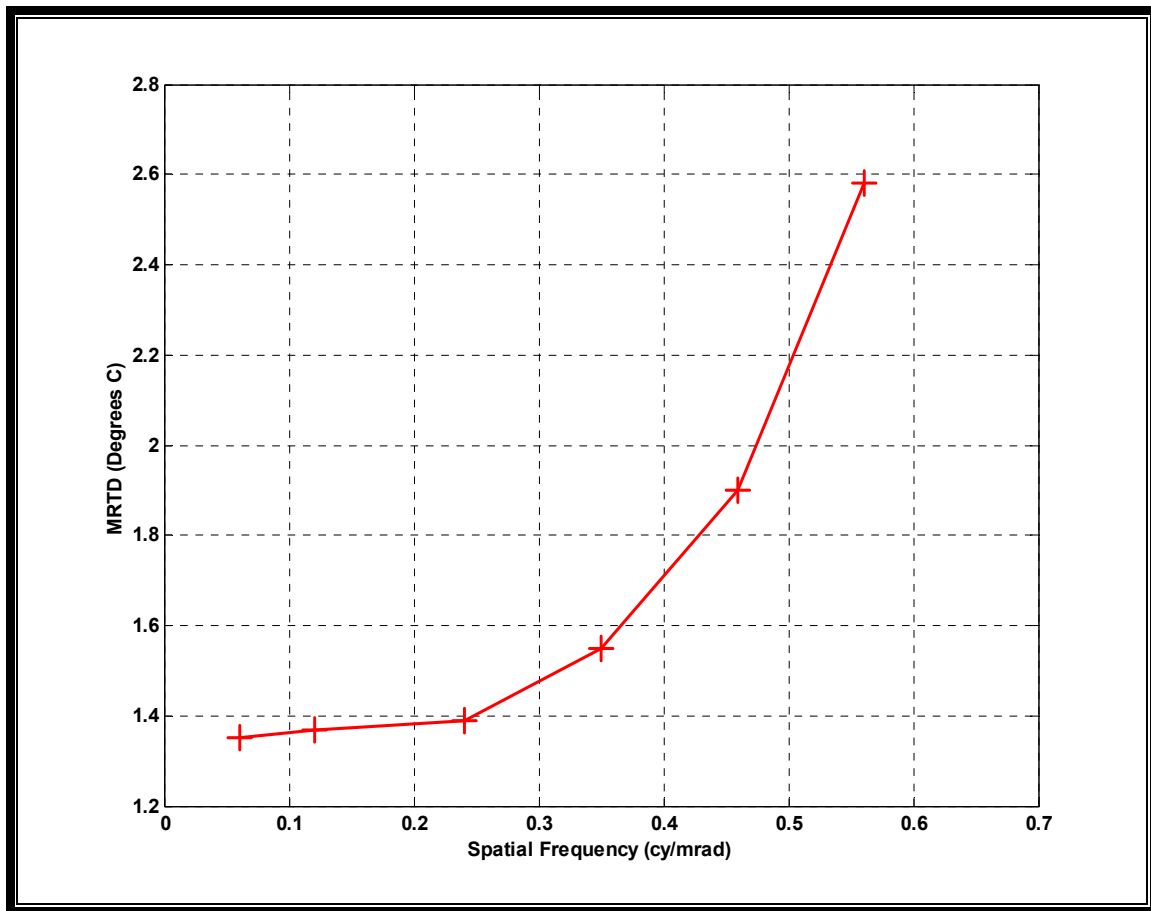
Figure F.3.   Visibility Model Objective MRTD Predictions for SNR of 6.0 (Constant SNR Case).
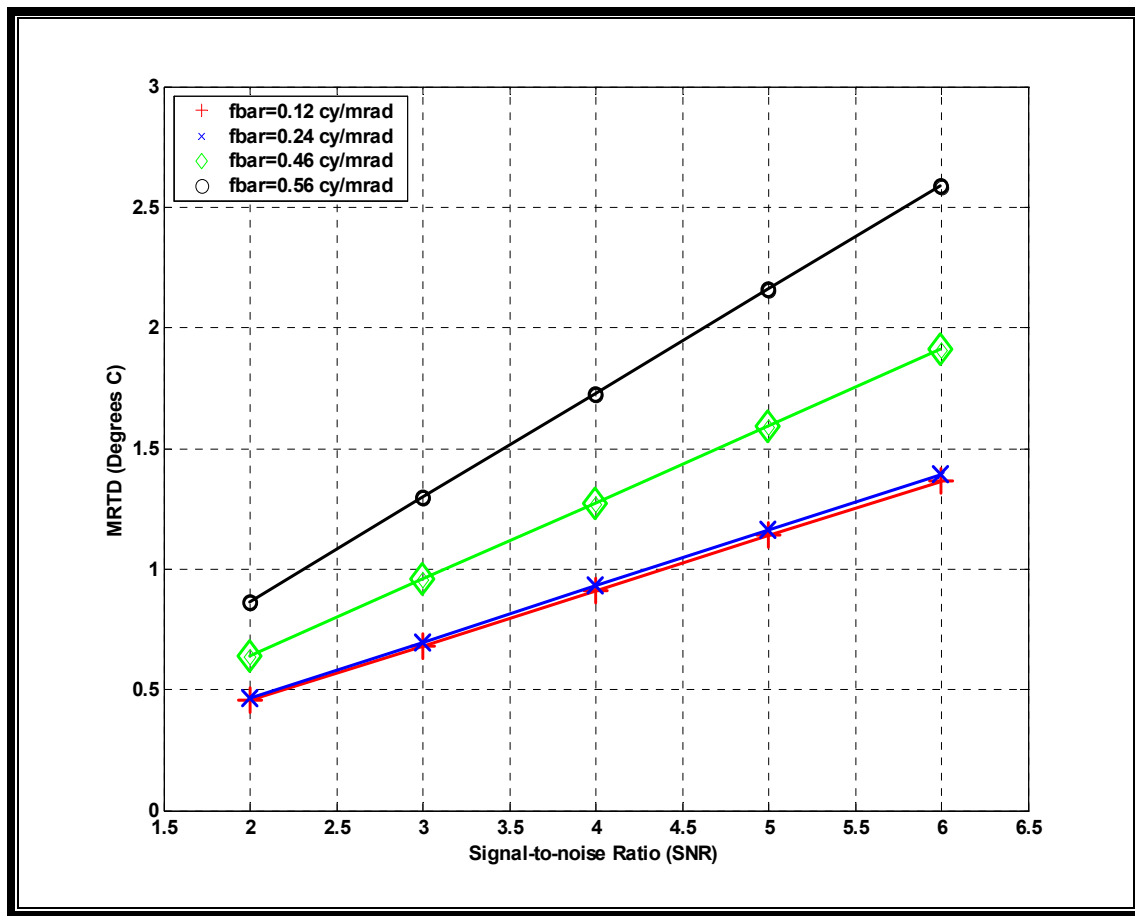
Figure F.4.   Visibility Model Objective Predictions MRTD vs. SNR (Constant Spatial Frequency Case).

APPENDIX G. THE VIRTUAL THERMAL IMAGE-PROCESSING MODEL CODE

The original MATLAB code files that are used in generating the virtual thermal images are contained in this appendix. "Virtual" is the core program that contains the input parameters of the thermal imager system being modeled and calculates the total system noise variance. Then it calls a second program "Vitualmtf" to calculate the subsystem MTFs and to introduce the white noise into he system. At this point, the white noise is generated according to the noise variance value calculated in "Virtual". "Vitualmtf" then calls a third program "alias" to include the aliasing effects into the calculations.

A.   VIRTUAL

```
%%%%%%%%%%%%%%%%%%%%%%%%%%%%%%%%%%%%%%%%%%%%%%%%%%%
%      THE VIRTUAL THERMAL IMAGE-PROCESSING MODEL
%      Yucel Kenter
%      7/25/2001
%      Given system parameters (Mitsubishi for this thesis),
%       this Matlab file will calculate the total system noise
%      variance that will be used to generate the white noise
%      Required m-files:
%      Virtual.m, Virtualmtf.m, alias.m, Qs2var.m,
%      Quad2var.m, Sre.m
%%%%%%%%%%%%%%%%%%%%%%%%%%%%%%%%%%%%%%%%%%%%%%%%%%%
clear;
clf;
%%%%%%%%%%%%%%%%%%%%%%%%%%%%%%%%%%%%%%%%%%%%%%%%%%%%%
%%% Spatial frequencies of interest (cy/mrad)%%%%%%%%%%%%%%%%
fbar = [.05:.05:1.4];
%%%%%%%%%%%%%%%%%%%%%%%%%%%%%%%%%%%%%%%%%%%%%%%%%%%%%%
```

```matlab
%%%%%%%%%%%%%%%%%%%% System Parameters %%%%%%%%%%%%%%%%%%%%%%
nh=512;          % number of horizontal detector elements
nv=512;          % number of vertical detector elements
a=16.24;         % detector active horizonal dimension (um)
b=12.49;         % detector active vertical dimension (um)
hpitch=26;       % detector pitch, horizontal (um)
vpitch=20;       % detector pitch, vertical (um)
fnumber=1.4;    % system f-number
focal=50;        % effective focal length (mm)
Fdot=60;         % frame rate (Hz)
clock=.97;       % clock-out factor (for integration time)
Dstarp=5e10;   % peak D-star (cm-Hz^1/2/Watt)
lambdap=5.0;    % peak wavelength (um)
lambda1=3.0;    % wavelength band lower limit (um)
lambda2=5.0;    % wavelength band upper limit (um)
fxec=2.3e6;      % electronic cut off (Hz)
monfac=.25;     % monitor Gaussian rms factor normalized by alpha
poles=1;         % number of poles for electronic filter
blurspot=0;      % standard deviation of blur spot diameter
theh=0;          % sample scene phase angle, horizontal (rad)
thev=0;          % sample scene phase angle, vertical (rad)
lloydc2 = 1.4388e4;
% c2 constant in Planck's blackbody equation (used in delta Tsc calculation)
Tbg=300;         % background temperature (Kelvin)
To=.95;          % optical transmission
delTsc=0;        % minimum threshold input contrast
sigmavh=.4;     % fixed pattern noise (percent of sigma tvh)
SNRthr=6.0;     % threshold signal-to-noise ratio
te=.2;            % eye integration time
```

```matlab
fpeye =0.4;          % eye peak response frequency
Deye =3.3;           % diameter of the eye pupil (mm)
monwave=0.55;        % monitor wavelength (microns)
%%%%%%%%%%%%%%%%%%%%%%%%%%%%%%%%%%%%%%%%%%%%%%%%%%%%%%%%
%%%%%%%%%%%%%%%%%%%% Preliminary Calculations %%%%%%%%%%%%%%%%
%%%%%%%%%%%%%%%%%%%%%%%%%%%%%%%%%%%%%%%%%%%%%%%%%%%%%%%%
avglambda=0.5*(lambda1+lambda2);   % average wavelength
opdia=focal/fnumber;               % optical diameter(mm)
alpha=a/focal;                     % horizontal DAS in mrad
beta=b/focal;                      % vertical DAS in mrad
sih=hpitch/focal;                  % horizontal sampling interval in mrad
siv=vpitch/focal;                  % vertical sampling interval in mrad
ao=pi*(opdia/2)^2;                 % area of collecting lens (mm^ 2)
td=clock/Fdot;                     % detector dwell time (sec)
fopt=opdia/avglambda;              % optical cut off in cy/mr
fsh=focal/hpitch;                  % horizontal sampling frequency (cy/mr)
fsv=focal/vpitch;                  % vertical sampling frequency (cy/mr)
tclock=nh*nv*Fdot;                 % in-clock direction, clock-out frequency (in Hz)
fth=sih*tclock;                    % clock-out frequency conversion factor, in-clock direction
ftv=siv*tclock/nh;                 % clock-out frequency conversion factor, out-of- clock direction
fehis=fxec/fth;                    % in-clock direction, electronic cutoff in (cy/mrad)
fevos=fxec/ftv;                    % out-of-clock direction, electronic cutoff in (cy/mrad)
sspmaxh=0                          % sample scene phase error, horizontal
sspmaxv=0;                         % sample scene phase error, horizontal
feyec=Deye /monwave;               % eye cut off in cy/mrad
```

```
%%%%%%%%%%%%%%%%%%%%%%%%%%%%%%%%%%%%%%%%%%%%%%%%%%%%%%%%%
%%%%%%%%%%%%%%%%%%%%% Total system noise calculations %%%%%%%%%%%%
%%%%%%%%%%%%%%%%%%%%%%%%%%%%%%%%%%%%%%%%%%%%%%%%%%%%%%%%%%
[MTFrf,fmax]=
meffcnt(fbar,fxec,fsh,fsv,sih,siv,fth,ftv,fopt,alpha,beta,blurspot,theh,thev,fehis,fevos,pole
s,monfac,sspmaxh,sspmaxv,feyec,fpeye);

%%%%%%%%%%% NETD calculation %%%%%%%%%%%%%%%%%%%%%%%%%%%%
refbw = (pi/4)*(1/td);           % reference bandwidth calculation
n1 = pi*sqrt(a*1e-4*b*1e-4*refbw);
d1 = (alpha*beta*1e-6*To*ao*1e-2*Dstarp);
d2 = lloydc2/(lambdap*Tbg^2)*(quad2var('sre', lambda1, lambda2, Tbg));
NETD = n1/(d1*d2)
%%%%%%%%%%% SNR improvement calculation %%%%%%%%%%%%%%%%%%%%%
tn2 = sqrt(1+sigmavh^2/(te*Fdot))*(pi^2*SNRthr/(8*sqrt(te*Fdot)))
%%%%%%%%%%%%%  Total system noise calculation  %%%%%%%%%%%%%%%%%%%%
MTFsys = (abs(MTFrf)).^2;         % overall system MTF
totbw = sum(sum(MTFsys)).*(alpha/td).*(fmax/128)
bwcorr = sqrt(totbw/refbw)          % bandwidth correction factor
sigmatvh=NETD*bwcorr;
sigmatotal=(sigmatvh^2+(0.4*sigmatvh)^2)^.5;
vartotal = sigmatotal^2            % Total noise variance (as in FLIR-92)
 %%%% Correction to noise variance for compensation  %%%%%%%%%%%%%%%%
varcorrected = vartotal*(fmax^2/totbw)
%Same value is used in meffcnt.m for the generation of white noise
%%%%%%%%%%%%%%%%%%%%%%%%%%%%%%%%%%%%%%%%%%%%%%%%%%%%%%%%%
```

B.   VIRTUALMTF

```
%%%%%%%%%%%%%%%%%%%%%%%%%%%%%%%%%%%%%%%%%%%%%%%%%%%%%%%
%   Yucel Kenter
%   This program creates virtual standard four-bar patterns
```

```
%   as input to the simulated TIS (Mitsubishi).
%   It then calculates the subsystem MTFs and applies them to
%   the input and finally produces the four-bar pattern
%   images at the output for the spatial frequencies
%   specified by the user. Overall system (Gaussian white)
%   noise is also created and added here at the detector.
%%%%%%%%%%%%%%%%%%%%%%%%%%%%%%%%%%%%%%%%%%%%%%%%%%
function
[MTFrf,fmax]=meffcnt(fbar,fxec,fsh,fsv,sih,siv,fth,ftv,fopt,alpha,beta,blurspot,theh,thev,
fehis,fevos,poles,monfac,sspmaxh,sspmaxv,feyec,fpeye);
d2=length(fbar);
%%%%%%%%%%%%%%%%%%%%%%%%%%%%%%%%%%%%%%%%%%%%%%%%%%%%
%%%%%%%%%%% Create bar pattern (Input contrast=1) %%%%%%%%%%%%%%%%%%
col1 = zeros(130,10);
col2 = [zeros(30,10);ones(70,10);zeros(30,10)];
col3 = zeros(130,93);
row1 = zeros(63,256);
%Horizontal MRTD bar pattern (A)
A=[row1;col3,col2,col1,col2,col1,col2,col1,col2,col3;row1];
%Vertical MRTD bar pattern (V)
V=A';
%%%%%%%%%%%%%%%%%%%%%%%%%%%%%%%%%%%%%%%%%%%%%%%%%%%%
%%%%%%%%%%%%% Plot bar pattern at the input %%%%%%%%%%%%%%%%%%%%%
%%%%%%%%%%%%%%%%%%%%%%%%%%%%%%%%%%%%%%%%%%%%%%%%%%%%
xside=linspace(0,12,73);
yside=xside;
%HORIZONTAL
figure(1)
surf(xside,yside,abs(A(56:2:200,56:2:200)))
```

```matlab
shading interp;
axis([0 12 0 12 0 2])
axis off
xlabel('x space, mrad')
ylabel('y space, mrad')
colormap(gray)
view(2)
%VERTICAL
figure(2)
surf(xside,yside,abs(V(56:2:200,56:2:200)))
shading interp;
axis([0 12 0 12 0 2])
axis off
xlabel('x space, mrad')
ylabel('y space, mrad')
colormap(gray)
view(2)
%%%%%%%%%%%%%%%%%%%%%%%%%%%%%%%%%%%%%%%%%%%%%%%%%%%%%%%%%%
%%%%%%%%%%% Transform into spatial freq. domain %%%%%%%%%%%%%%%%%
%%%%%%%%% and apply scaling to represent the appropriate %%%%%%%%%%%%%%
%%%%%%%%%%%%%%%%% spatial frequency  %%%%%%%%%%%%%%%%%%%%%%%%%
B= fft2(A);w=fft2(V);
b=abs(B);x=abs(w);
%%%%%%%%%%%%%%%%%%%%%%%%%%%%%%%%%%%%%%%%%%%%%%%%%%%%%%%%%
%%%%%%%%%%%%%%%%%%%%%% Create Gaussian white noise %%%%%%%%%%%%%
%%%%%%%%%%%%%%%%%%%%%%%%%%%%%%%%%%%%%%%%%%%%%%%%%%%%%%%%%
                        vartotal = 0.0022;        % This value is the calculated total
                        noise value for delTsc=0.0981 (vartotal=sigmatvh^2 +
                        sigmavh^2)
```

```matlab
varcorrected = 0.0087;      % This value is the corrected total noise value
noise = sqrt(varcorrected).*randn(size(B));   % Noise matrix in space
N = fftshift(1.45.*fft2(noise));            %        Noise
                                            spectrum (1.45 is the compensation factor for the
                                            contrast    manipulation    accomplished    after
                                            reconstruction filtering)
%%%%%%%%%%%%%%%%%%%%% Now loop through frequencies %%%%%%%%%%%
for counter = 1:d2;
fx = fbar(counter);
%%%%%%%%%%%%%%%%%%%%%%%%%%%%%%%%%%%%%%%%%%%%%%%%%%%%%%%%
%%%%%%%% W refers to the actual width of one bar in mrad %%%%%%%%%%%%%%%%
%%%%%%%% 'del' terms are used to find the appropriate %%%%%%%%%%%%%%%%%%
%%%%%%%%%%%%% frequency and space scales %%%%%%%%%%%%%%%%%%%%%%%%
W=1/(2*fx);
Nw = 10;       % number of elements in one bar (x)
Nt = 256;      % number of elements in vector (m x m)
delt = W/Nw;
DELt = Nt*W/Nw;
delf = 1/DELt;
DELf = 1/delt;
fmax = DELf/2;
fscale = linspace(-fmax,fmax,256);
xscale = linspace(-DELt/2,DELt/2,256);
yscale = linspace(-DELt/2,DELt/2,256);
%%%%%%%%%%%%%%%%%%%%%%%%%%%%%%%%%%%%%%%%%%%%%%%%%%%%%
%%%%%%%%%%% Create a spatial freq. matrix to be used in %%%%%%%%%%%%
%%%%%%%%%%%%%%%%  MTF calculations %%%%%%%%%%%%%%%%%%%%%%%%%
uux=1:256;
uuy=1:256;
```

```matlab
Matfx=uux*uuy';
Matfx=ones(size((Matfx)));
Matfy=Matfx;
for k=-128 : 127;
  for  n=-128:127;
    k2=k+129;
    n2=n+129;
    Matfx(k2,n2)=k*fmax/128;
    Matfy(k2,n2)=n*fmax/128;
  end;
end;
fr=((Matfx).^2+(Matfy).^2).^(0.5);
%%%%%%%%%%%%%%%%%%%%%%%%%%%%%%%%%%%%%%%%%%%%%%%%%%%%%%%%%
%%%%%%%%%%%%%%%%%%%%%% Create image formation MTF %%%%%%%%%%%%%%
%%%%%%%%%%%%%%%%%%%%%%%%%%%%%%%%%%%%%%%%%%%%%%%%%%%%%%%%%
 % DIFFRACTION LIMITED OPTICAL MTF.
(Circular aperture)
c1=fr/fopt;
for  ii=1:256;
  for jj=1:256;
    if  c1(ii,jj)>1.0;
      c1(ii,jj)=1.0;
    end;
  end;
end;
c2=sqrt(1-c1 .^2);
ro=2/pi .*(acos(c1)-(c1 .*c2));
% GEOMETRIC BLUR OPTICAL MTF
f1 = (fr.^2).*pi^2.*(-2).*blurspot^2;
```

```matlab
rb = exp(f1);


% HORIZONTAL AND VERTICAL SAMPLE SCENE PHASE MTF
rsh = (2*Matfx/fsh)*theh;
rsh2 = cos(rsh);
rsv = (2*Matfy/fsv)*thev;
rsv2 = cos(rsv);
rs = rsh2.*rsv2;
% DETECTOR HORIZONTAL MTF.   (For rectangular detector)
c3fx=pi.*alpha.*Matfx;
% DETECTOR VERTICAL MTF.     (For rectangular detector)
c3fy =pi.*beta.*Matfy;
  for m=1 :256;
    for  p=1:256;
      if c3fx(m,p)==0
        c3fx(m,p)=0.01;
        end;
      if c3fy(m,p)==0
        c3fy(m,p)=0.01;
      end;
    end;
  end;
rdh=abs(sin(c3fx)./c3fx) ;
rdv=abs(sin(c3fy)./c3fy) ;


% DETECTOR 2D MTF
rd=rdv.*rdh;
% Cascade MTFs
```

```matlab
u=ro.*rd.*rb.*rs;


%%%%%%%%%%%%%%%%%%%%%%%%%%%%%%%%%%%%%%%%%%%%%%%%%%%%%%%
%%%%%% Add white noise and multiply image spectrum by image %%% %%%%%%
%%%%%%%%%%%%%%%%%%%%formation MTF %%%%%%%%%%%%%%%%%%%%%%%%
%%%%%%%%%%%%%%%%%%%%%%%%%%%%%%%%%%%%%%%%%%%%%%%%%%%%%%%
d=fftshift(B);dv= fftshift(w);display('showing noise term');fbar(counter)
mess = d.*u+N;mes2 = dv.*u+N; % noise is added here
%%%%%%%%%%%%%%%%%%%%%%%%%%%%%%%%%%%%%%%%%%%%%%%%%%%%%%%
%%%%%%%%%%%%%%%%%%%% Calculate aliasing terms %%%%%%%%%%%%%%%
%%%%%%%%%%%%%%%%%%%%%%%%%%%%%%%%%%%%%%%%%%%%%%%%%%%%%%%
aliasterm = zeros(size(mess));
valiasterm = aliasterm;
[aliasterm,aliasx]                                                                  =
alias(Matfx,Matfy,fscale,fsh,fsv,mess,sspmaxh,sspmaxv,fbar,counter);
[valiasterm,aliasx]                                                                 =
alias(Matfx,Matfy,fscale,fsh,fsv,mes2,sspmaxh,sspmaxv,fbar,counter);
%%%%%%%%%%%%%%%%%%%%%%%%%%%%%%%%%%%%%%%%%%%%%%%%%%%%%%%
%%%%%%%%%%%%%% Add alias term to pre-filtered scene %%%%%%%%%%%%%%
%%%%%%%%%%%%%%%%%%%%%%%%%%%%%%%%%%%%%%%%%%%%%%%%%%%%%%%
withalias= mess + aliasterm;
vertalias = mes2 + valiasterm;
%%%%%%%%%%%%%%%%%%%%%%%%%%%%%%%%%%%%%%%%%%%%%%%%%%%%%%%
%%%%%%%%% Create image reconstruction MTF %%%%%%%%%%%%%%%%%%%%
%%%%%%%%%%%%%%%%%%%%%%%%%%%%%%%%%%%%%%%%%%%%%%%%%%%%%%%
% ELECTRONICS OTF.  (Multi-pole low pass filter)
% OTF from impulse response function)
N=256;
dx=1/(2*fmax);
```

```
dy=dx;
uux2=(0:(N-1))*dx;
uuy2=(0:(N-1))*dy;
respx=exp(-uux2*fehis*(2*pi));
respy=exp(-uuy2*fehis*(2*pi));
respxy=respx'*respy;
sgnflip=((-1)*ones(size(1:N))).^(0:(N-1));
uuxy=sgnflip'*sgnflip;
respxy2=respxy.*uuxy;
eloTF=FFT2(respxy2);
mag=abs(eloTF);
eloTF=eloTF/(max(max(mag)));
% Normalization is done here
elMTF=abs(eloTF);
 %  CRT MONITOR SPATIAL MTF.
c7=(fr/(1/sih)) .^2;
c8=(monfac)^2;        % sigma/sih = .25
rm=exp(-2 *pi^2 .*c7 .*c8);
% CASCADE ELECTRONICS OTF AND DISPLAY MTF
recon=rm.*eloTF.*rd;
%%%%%%%%%%%%%%%%%%%%%%%%%%%%%%%%%%%%%%%%%%%%%%%%%%%%
%%% Calculate system MTF (for noise bandwidth calculations)
%%%%%%%%%%%%%%%%%%%%%%%%%%%%%%%%%%%%%%%%%%%%%%%%%%%%
% Calculate eye MTF
c11=fr/feyec;
for  iii=1:256;
  for jjj=1:256;
    if  c11(iii,jjj)>1.0;
      c11(iii,jjj)=1.0;
```

```matlab
        end;
      end;
   end;
c22=sqrt(1-c11.^2);
const1=0.4/feyec;
const2=sqrt(1-const1^2);
norm= 1/(2/pi *(acos(const1)-(const1*const2)));
c33=2*norm/pi .*(acos(c11)-(c11 .*c22));
clear c11 c22;
c44=fr./fpeye;
reye=min(c44,c33);
clear c11 c22 c33 c44;
% Multiply Eye MTF with the Reconstruction OTF
MTFrf = reye.*recon;
%%%%%%%%%%%%%%%%%%%%%%%%%%%%%%%%%%%%%%%%%%%%%%%%%%%%
%%%% Multiply pre-filtered and aliased image spectrum %%%%%%%%%%%%%%%%%%
%%%%%%%% with the aliased, filtered, scene %%%%%%%%%%%%%%%%%%%%%%%%%%
%%%%%%%%%%%%%%%%%%%%%%%%%%%%%%%%%%%%%%%%%%%%%%%%%%%%
outalias = withalias.*recon;    % Output spectrum WITH aliasing (Horizontal)
noalias = mess.*recon;          % Output spectrum WITHOUT aliasing (Horizontal)
veral2  = vertalias.*recon;     % Output spectrum WITH aliasing (Vertical)
veral3  = mes2.*recon;          % Output spectrum WITHOUT aliasing (Vertical)
%%%%%%%%%%%%%%%%%%%%%%%%%%%%%%%%%%%%%%%%%%%%%%%%%%%
%%%%%%%%%% Transform back to spatial domain %%%%%%%%%%%%%%%%%%%%
%%%%%%%%%% A normalization function is used %%%%%%%%%%%%%%%%%%%%
%%%%%%%%%%   for a better visualization    %%%%%%%%%%%%%%%%%%%%
%%%%%%%%%% normfunc = ((2/pi).*atan(5.*(x-0.5))+1)./2; %%%%%%%%%%%%%%
%%%%%%%%%%%%%%%%%%%%%%%%%%%%%%%%%%%%%%%%%%%%%%%%%%%
messy = fftshift(outalias);
```

```matlab
messy2 = fftshift(noalias);

gigo = fftshift(veral2);

gigo2 = fftshift(veral3);

C=ifft2(messy);                  % Output image WITH aliasing (Horizontal)

C=((2/pi).*atan(5.*(C-0.5))+1)./2;   % Normalization is applied here

D=ifft2(messy2);                 % Output image WITHOUT aliasing (Horizontal)

D=((2/pi).*atan(5.*(D-0.5))+1)./2;   % Normalization is applied here

E=ifft2(gigo);                   % Output image WITH aliasing (Vertical)

E=((2/pi).*atan(5.*(E-0.5))+1)./2;   % Normalization is applied here

F=ifft2(gigo2);                  % Output image WITHOUT aliasing (Vertical)

F=((2/pi).*atan(5.*(F-0.5))+1)./2;   % Normalization is applied here

%%%%%%%%%%%%%%%%%%%%%%%%%%%%%%%%%%%%%%%%%%%%%%%%%%%%%

%%%%%%%%%%%%%%%%%%% Virtual images are created here %%%%%%%%%%%%%%%

%%%%%%%%%%%%%%%%%%%%%%%%%%%%%%%%%%%%%%%%%%%%%%%%%%%%%

%HORIZONTAL

figure(3)

xside=linspace(0,(145/(fx*20)),73);yside=xside;

% Modified for the scaling on the axis

surf(xside,yside,abs(C(56:2:200,56:2:200)))

shading interp;

axis([0 (145/(fx*20)) 0 (145/(fx*20)) 0 2])

% Modified for the scaling on the axis

xlabel('x space, mrad')

ylabel('y space, mrad')

colormap(gray)

grid off

view(2)

%VERTICAL

figure(4)
```

xside=linspace(0,(145/(fx*20)),73);

yside=xside;

surf(xside,yside,abs(E(56:2:200,56:2:200)))

shading interp;

axis([0 (145/(fx*20)) 0 (145/(fx*20)) 0 2])

xlabel('x space, mrad')

ylabel('y space, mrad')

colormap(gray)

grid off

view(2)

%%%

C.   ALIAS

%%%

%   This program calculates the alias terms and turns them

%   back to "virtualmtf"

%%%

function [aliasterm,aliasx] = alias(Matfx,Matfy,fscale,fsh,fsv,mess,b,c,fbar,counter)

%%%

%%%%%%% Represent aliasing by repeating the filtered %%%%%%%%%%%%%%%%

%%%%%%% spectrum at sampling freq. intervals %%%%%%%%%%%%%%%%%%%%%

%%%

%%%%%%%%%%% Alias terms (other than cross aliases) %%%%%%%%%%

where = find(fscale/fsh >1);

if isempty(where);

  cent = 256;multiple=0;

else

```matlab
    fbar(counter)
    cent = where(1)
    multiple=1;
end
start = cent-128;unused = 256-start;
%%%%% Alias terms due to sampling in x direction %%%%%
%First positive side
aliastxp = circshift(mess,[0 (start-1)]);
aliastxp = aliastxp.*exp(j*2*pi*b*fsh);
%Now negative side
aliastxn = circshift(mess,[0 -(start-1)]);
aliastxn = aliastxn.*exp(-j*2*pi*b*fsh);
%Combine the two
aliasx = aliastxp+aliastxn;
wherev = find(fscale/fsv >1);
if isempty(wherev);
        centv = 256;
        multiplev = 0;
else
        fbar(counter)
        centv = wherev(1)
        multiplev = 1;
end
startv = centv-128;
unusedv = 256-startv;
%%%%% Alias terms due to sampling in y direction %%%%%
%First positive side
aliastyp = circshift(mess,[(startv-1) 0]);
aliastyp = aliastyp.*exp(j*2*pi*c*fsv);
```

```matlab
%Now negative side
aliastyn = circshift(mess,[-(startv-1) 0]);
aliastyn = aliastyn.*exp(-j*2*pi*c*fsv);
%Combine the two
aliasy = aliastyp+aliastyn;
%%%%%%%%%%%% Cross alias terms %%%%%%%%%%%%%%%%%%%%%%%%%%%%%
aliasxpyp=circshift(mess,[(startv-1) (start-1)]);
aliasxpyp=aliasxpyp.*exp(j*2*pi*b*fsh).*exp(j*2*pi*c*fsv);

aliasxpyn=circshift(mess,[-(startv-1) (start-1)]);
aliasxpyn=aliasxpyn.*exp(j*2*pi*b*fsh).*exp(-j*2*pi*c*fsv);

aliasxnyp = circshift(mess,[(startv-1) -(start-1)]);
aliasxnyp=aliasxnyp.*exp(-j*2*pi*b*fsh).*exp(j*2*pi*c*fsv);

aliasxnyn=circshift(mess,[-(startv-1) -(start-1)]);
aliasxnyn=aliasxnyn.*exp(-j*2*pi*b*fsh).*exp(-j*2*pi*c*fsv);

crossterm=multiple*multiplev*(aliasxpyp+aliasxpyn+aliasxnyp+aliasxnyn);
%%%%%%%%%%%%%% Total alias term %%%%%%%%%%%%%%%%%%%%%%%%%%%%%%
aliasterm = multiple*aliasx + multiplev*aliasy +crossterm;
%%%%%%%%%%%%%%%%%%%%%%%%%%%%%%%%%%%%%%%%%%%%%%%%%%%%%%%%%%%%%%%
```

APPENDIX H. THE IMAGE RECONSTRUCTION DETECTOR MTF ANALYSIS

As mentioned in Chapter IV, both the Visibility model and the Virtual Thermal Image-Processing model include a detector MTF into the image reconstruction process as treated by Lloyd in Reference 10. In this appendix, the analysis of the detector MTF in the backend filtering process will be made in the images generated by Virtual Thermal Image-Processing model.

The experiments conducted with the Virtual Thermal Image-Processing model showed that some of the distortion appearing as patterns of ripples due to aliasing was smoothed out from the image with the introduction of the detector MTF into the reconstruction process. Figures H.1 and H.2 demonstrate the patterns of distortion on the horizontal and the vertical four-bar targets at 1.15 cycles/mrad respectively when the detector MTF is excluded. Following Figures H.3 and H.4 show how the detector MTF filters out some of these aliasing effects from the image when it is included into the reconstruction MTF.

Figure H.1. Horizontal Four-Bar Pattern Image Generated wthout the Additional Detector MTF at 1.15 Cycles/Mrad. Note Ripple Detail in the Vertical Direction.

Figure H.2. Vertical Four-Bar Pattern Image Generated without the Additional Detector MTF at 1.15 Cycles/Mrad.
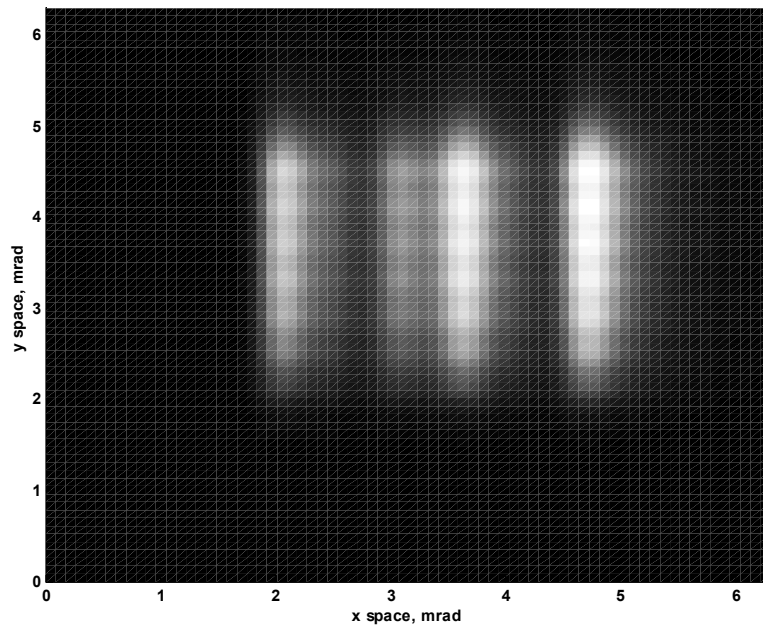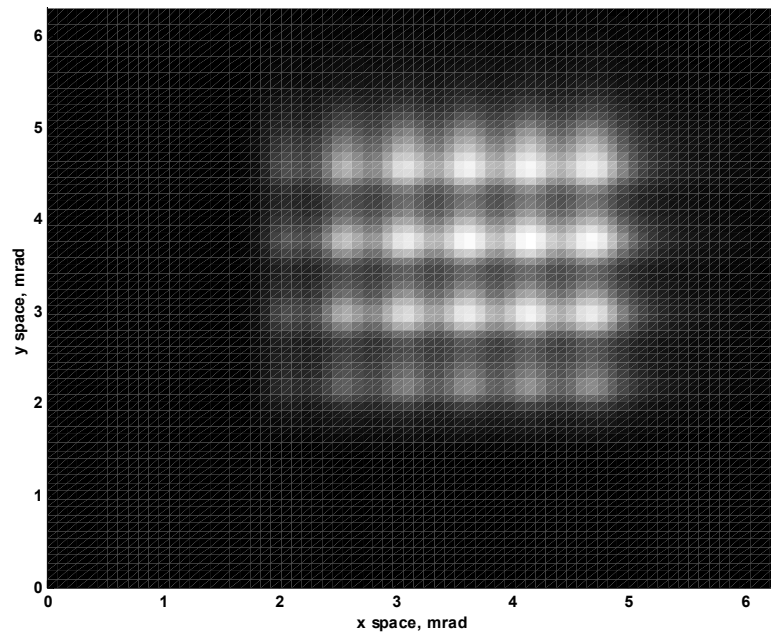
146
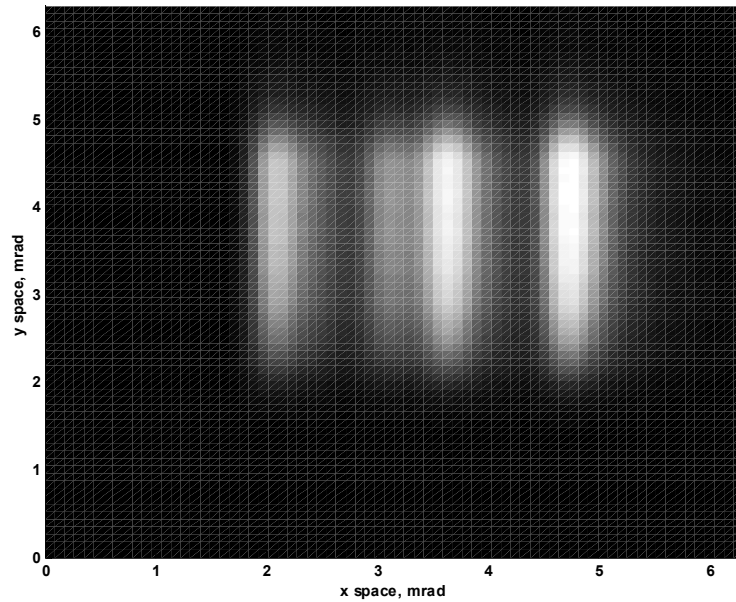
Figure H.3.   Horizontal Four-Bar Pattern Image Generated with the Additional Detector MTF at 1.15 Cycles/Mrad. Note Suppression of Vertical Ripple Modulation.
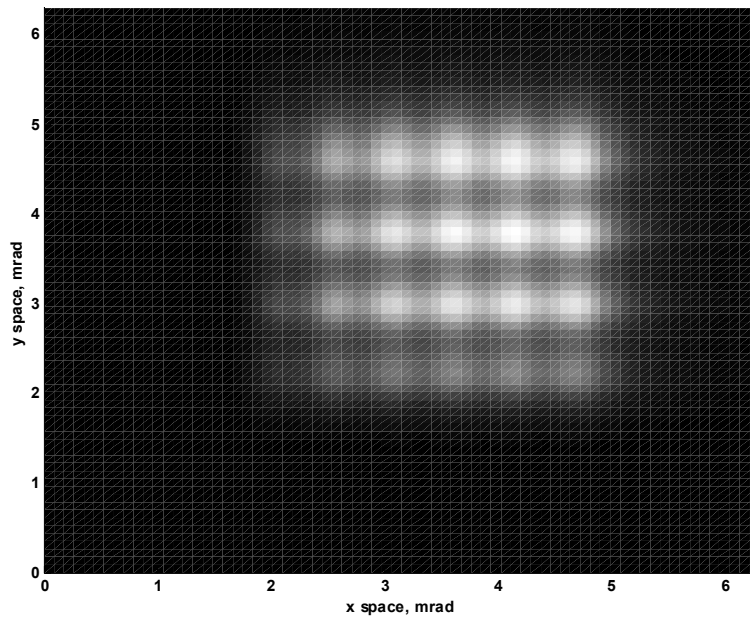
Figure H.4.   Vertical Four-Bar Pattern Image Generated with the Additional Detector MTF at 1.15 Cycles/Mrad.

147

The most significant observation to be made from these figures is the visual difference of the filtering process employed by the image reconstruction detector MTF in the output images. Although the same MTF is used for both the horizontal and vertical bar patterns the detector MTF filtering effect in the horizontal bar pattern image is much more apparent because the filtered ripples were brought about by the aliasing in the vertical direction that was previously confirmed to have weaker effects. This explanation still applies for the vertical bar pattern image, however the net effect is not as easily observable because the vertical bar pattern is strongly distorted by aliasing in the horizontal direction such that the bars appear to be dissected.

APPENDIX I. RESULTS OBTAINED FROM THE ANALYSIS OF RIPPLE EFFECTS BROUGHT ABOUT BY ALIASING

f_S (cycles/mrad)	n	(n. f_S)
0.2	33	6.6
0.3	21	6.3
0.4	16	6.4
0.5	13	6.5
0.6	10	6
0.7	9	6.3
0.8	8	6.4
0.9	7	6.3
1	6	6
1.1	5	5.5
1.2	5	6

Table I.1.   Ripple Effect Analysis Results.

Where

f_S is the bar spatial frequency in cycles/mrad

n   is the number of ripples observed along a bar

The multiplication of number of ripples with the bar spatial frequency stays at an approximately constant value as seen in the rightmost column in Table I.1. This is an indication of the fact that the pattern introduced by aliasing into the thermal images is stationary for all bar spatial frequencies. An example illustrating the number of ripples along a bar from a vertical bar pattern for a spatial frequency of 0.90 cycles/mrad is given below in Figure I.1.
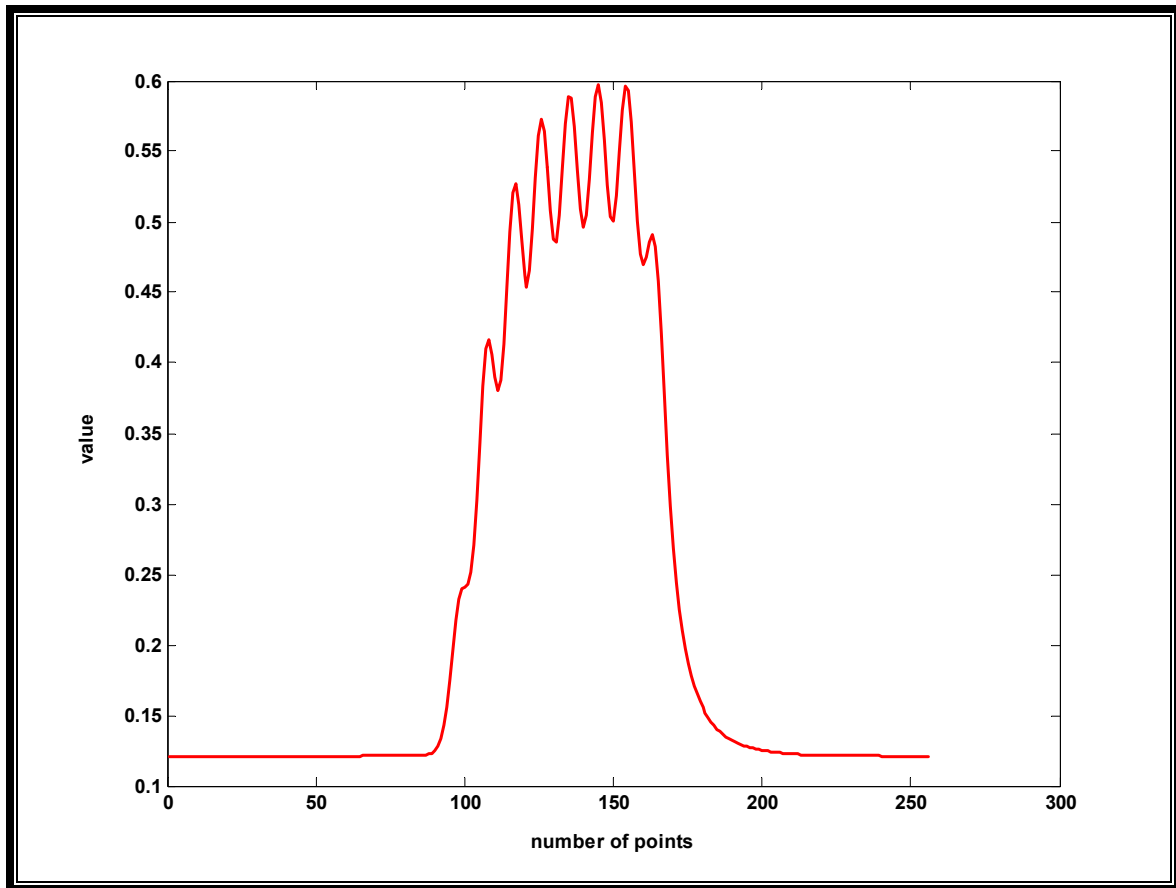
Figure I.1.   An Example Illustrating the Ripple Effect Along a Vertical Bar at 0.90 Cycles/Mrad. This Pattern Remains Constant as the Spatial Frequency of the Bar Pattern Changes.

150

APPENDIX J. THE RESULTS OBTAINED FROM THE ANALYSIS FOR DERIVING SAMPLING FRQUENCY FROM THE RIPPLE EFFECTS BROUGHT BY ALIASING

f_S (cycles/mrad)	W=1/(2.f_S)	L=7.W	n	Ripple frequency =(n/L)
0.2	2.5	17.5	33	1.885
0.3	1.667	11.667	21	1.8
0.4	1.25	8.75	16	1.828
0.5	1	7	13	1.857
0.6	0.833	5.833	10	1.714
0.7	0.714	5	9	1.8
0.8	0.625	4.375	8	1.828
0.9	0.556	3.889	7	1.8
1	0.5	3.5	6	1.714
1.1	0.454	3.181	5	1.571
1.2	0.4167	2.9167	6.6	1.714
Sampling frequency (calculated from system parameters) = 1.92 cycles/mrad				

Table J.1.   Derivation of Sampling Frequency from Ripple Effects Brought by Aliasing.

Where

f_S is the bar spatial frequency in cycles/mrad

W   is the angular subtense on a single bar in mrad

L   is the length of one bar in mrad

n   is the number of ripples observed along a bar at the corresponding bar spatial frequency

(n/L)   gives the ripple frequency in ripples/mrad

151

As seen in the rightmost column in Table J.1, the ripple frequencies derived for each bar spatial frequency from the ripple pattern produced by aliasing agrees within a reasonable range of error with the sampling frequency calculated from the Mitsubishi system parameters.

APPENDIX K. PRE-PRINT OF THE PAPER ACCEPTED FOR PRESENTATION AT THE THIRTY-FIFTH ASILOMAR CONFERENCE

Aliasing Effects in Thermal Images of Four-bar Patterns below and above the Nyquist Limit

M.Celik, Y. Kenter, A.Cooper[a], R. Pieper[b]

Naval Postgraduate School

Monterey CA 93943

[a]Department of Physics

[b]Department of Electrical and Computer Engineering

Abstract

A new virtual thermal image-processing model is introduced in this paper. This visualization program is based on earlier modeling work focused on predicting the minimum resolvable temperature (MRTD), which is a standard performance measure for forward looking infrared radar (FLIR) imaging systems. Relevant filtering, noise and sampling processes are included in the visualization model.   In this paper it will be demonstrated and explained that aliasing effects in thermal images of four-bar patterns cannot in general be adequately modeled as noise. In particular, the simulation experiments demonstrate that aliasing can have a noticeable visual enhancing effect at spatial bar frequencies less than the Nyquist limit.

1.   Introduction

Minimum resolvable temperature difference (MRTD) is a standard performance measure for FLIR thermal imaging systems.[Ref 1]   It is defined as the temperature difference between a four-bar target and its uniform background, which is required by a trained observer to just resolve all four bars. MRTD is a function of four-bar target spatial frequency as demonstrated in Figure K.1. Spatial frequency is defined as:

$$f_o = \frac{R}{2W} \quad cy/mrad \tag{1}$$

where W is bar width in millimeters and R is target range in meters.

2. Sampling and Aliasing

Current state-of-the art thermal imaging systems incorporate staring focal plane arrays (FPA) which sample the scene spatially. Figure K.2 demonstrates two-dimensional spatial sampling by detector elements in a staring FPA. Horizontal spatial sampling frequency is calculated as:

$$f_s = \frac{f_{optics}}{\Delta x} \qquad cy/mrad \qquad (2)$$

where f_{optics} is optical focal length in mm and Δx is pixel pitch in μm.

Sampling and aliasing effects are more easily appreciated when examined in the spatial frequency domain. Multiplication in the space domain corresponds to convolution in the frequency domain. Therefore, the sampling effect produces replication of the object spectrum at integer multiples of the sampling frequency.

Sampling theory suggests that a frequency component in the original image above the Nyquist limit appears as a lower frequency component after sampling due to the effect called 'aliasing'. Equation 3 defines the Nyquist frequency limit. The effects of aliasing and the degree to which it interferes with recognition depend on the scene that is viewed. Aliasing tends to be apparent as image distortion and degradation when viewing periodic targets such as a four bar pattern.

$$f_N = \frac{f_S}{2} \qquad cy/mrad \qquad (3)$$

Different models have been proposed to predict the performance of staring thermal imaging systems. The infrared community standard FLIR92 model predicts MRTD results below the Nyquist limit and ignores aliasing effects. A visibility model, proposed by R.J.Pieper and A.W. Cooper of the Naval Postgraduate School in 1994, also predicts the MRTD of staring thermal imaging systems. The model is based on a minimum threshold input contrast parameter and a contrast reduction factor due to aliasing and blurring effects [Ref. 2]. It provides MRTD predictions beyond the Nyquist frequency limit. MRTD predictions from the visibility model have been shown to be in better agreement with the laboratory measurements [Ref. 3].

3. Virtual thermal image processing model

Virtual MRTD experiments have been performed at the U.S. Army Night Vision Electronics Sensors Directorate using simulations based on the FLIR92 model. In the experiments, effects of blurring and noise on the image have been reported [Ref. 4].

A new Virtual thermal image processing model (or virtual thermal image processing model) is introduced in this paper. The model is based on the Visibility MRTD model and has been developed at the Naval Postgraduate School. It takes the

current thermal imaging system modeling concerns such as sampling and aliasing into account. From the basic staring imaging system parameters, the model creates the system response and applies it to the input four-bar target. The model provides visual images that can be obtained with the actual imaging system being modeled. This allows the user to virtually evaluate the effects of noise, sampling and aliasing on the imagery. The virtual thermal image processing model is written using MATLAB computational software. The model block diagram is presented in Figure K.3.

First, a two-dimensional four-bar target is generated. The model works with both horizontal and vertical bar patterns. Taking the two-dimensional Fast Fourier Transform (2-D FFT) of the bar pattern, a four-bar target spatial frequency spectrum is obtained. The target spectrum is then multiplied by the Image Formation Modulation Transfer Function (MTF). At this stage, white noise is generated and added to the spectrum. Following the application of sampling and aliasing effects, the filtered and aliased spectrum is multiplied by the image reconstruction MTF. Finally, taking the inverse 2-D FFT gives the visual four-bar target representation.

## 4.	Aliasing Effects Below the Nyquist Limit

Experiments with the virtual thermal image-processing model have provided some useful insights into the problems encountered in modeling aliasing effects. Aliasing effects are shown to be present in the image of four-bar targets at spatial frequencies below the Nyquist limit. The spatial sampling frequency from the system parameters is 1.92 cycles/mrad. Profiles across a four-bar target at 0.65 cycles/mrad bar spatial frequency and its images including and excluding aliasing effects are plotted in Figure K.4. Contrast enhancement due to aliasing is noticeable.

An analytical approach to this question gives a result similar to that obtained using virtual thermal image processing model. Equation 4 gives the horizontal MRTD target spectrum, which is the two-dimensional Fourier transform of the four-bar pattern.

$$I(f_x, f_y) = \left[\left(\frac{1}{\pi f_x}\right)\left(-\sin(\pi f_x W) + \sin(3\pi f_x W) - \sin(5\pi f_x W) + \sin(7\pi f_x W)\right)\right] \times \left(\frac{1}{\pi f_y W}\right)\sin(7\pi f_y W) \quad (4)$$

where f_x and f_y are the spatial frequencies along the horizontal and vertical directions. A plot of this spectrum along the x-axis ($f_y=0$) is given in Figure K.5. Note the repetition of the spectrum at intervals of the sampling frequency. The figure shows that the sample generated replicas of the original spectrum overlap with the target spectrum (baseband) and aliasing occurs. It is important to note that this result is in line with the result obtained from the virtual thermal image-processing model. Aliasing is an issue for bar-targets at four-bar spatial frequencies (1) below the Nyquist limit (3).

5. Aliasing Effects Above the Nyquist Limit

A number of approaches have been proposed to account for aliasing in imagery. It has been argued that aliasing can be adequately represented as signal-dependent additive noise [Ref. 5]. Another important observation made during the experiments with the virtual thermal image-processing model is that aliasing effects manifest themselves in much different form than noise in imagery. As demonstrated in Figure K.6, effects of noise are dominant at small spatial frequencies and noise tends to mask the target pattern. Aliasing effects, on the other hand become more important at higher spatial frequencies and aliasing creates distortion in imagery. The four-bar target may appear as a distorted three-bar pattern. A target image at a high spatial frequency where aliasing is dominant is presented in Figure K.7. At the same spatial frequency, noise alone does not distort the image; four bars are resolvable in Figure K.8. These results suggest that aliasing cannot be adequately represented as noise.

LIST OF REFERNCES

1.	Accetta, J.S. and Shumaker, D.L., *The Infrared and Electro-Optical Systems Handbook, Volume 4*, SPIE Optical Engineering Press, Bellingham, WA, 1996.

2.	Groen, M.S., Koc, C., Cooper, A.W., and Pieper, R.J., "*A Second Generation Visibility Based Model for Objective/Subjective FLIR MRTD*" Proceedings of the IRIS Specialty Group on Passive Sensors, Vol. 2, pp. 81-96, 1996.

3.	Groen, M., "*Development and Validation of Second Generation Visibility-Based Model for Predicting Subjective and Objective Minimum Resolvable Temperature Difference for Staring Thermal Imaging Systems*", Master's Thesis in Electrical Engineering and in Physics, Naval Postgraduate School, Monterey, CA, December 1995.

4.	Jacobs, E., Driggers, R., Edwards, T., and Cha, J., "*Virtual MRTD Experiments*" *SPIE,* Vol. 3701*,* pp. 74-80, April 1999.

5.	Park, S.K. and Hazra, R., "*Aliasing as Noise: A Quantitative and Qualitative Assessment*" SPIE, Vol. 1969, pp. 54-65, August 1993.
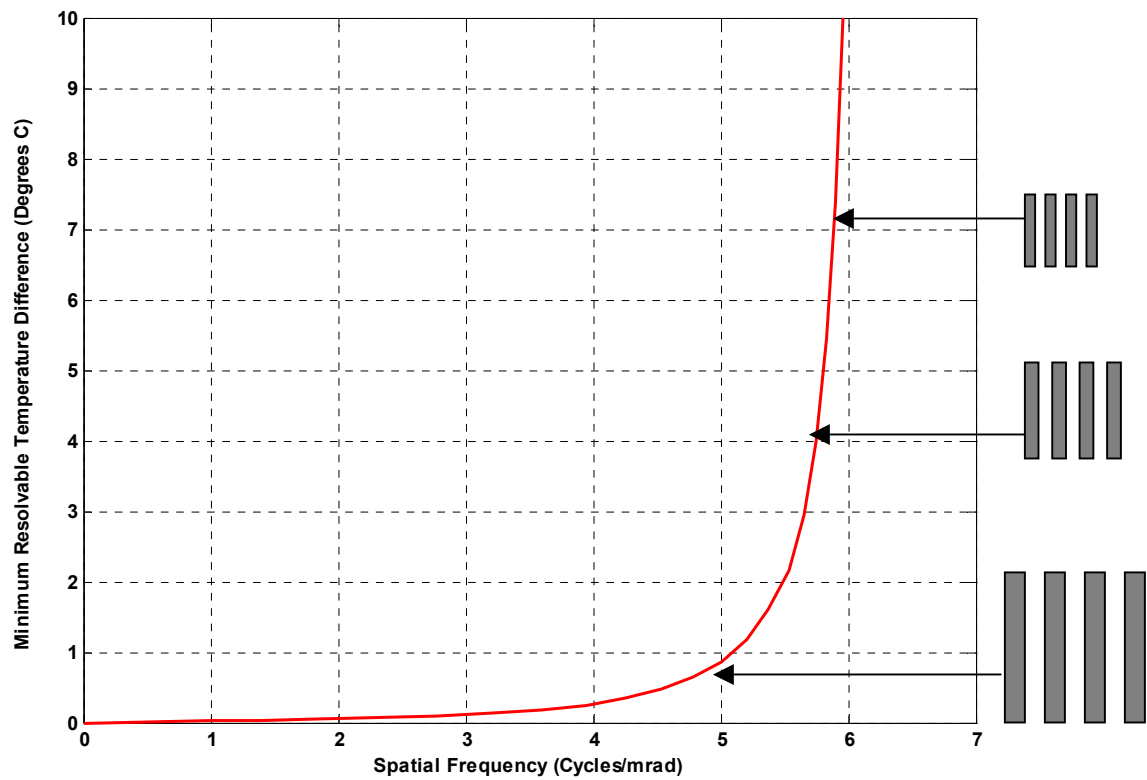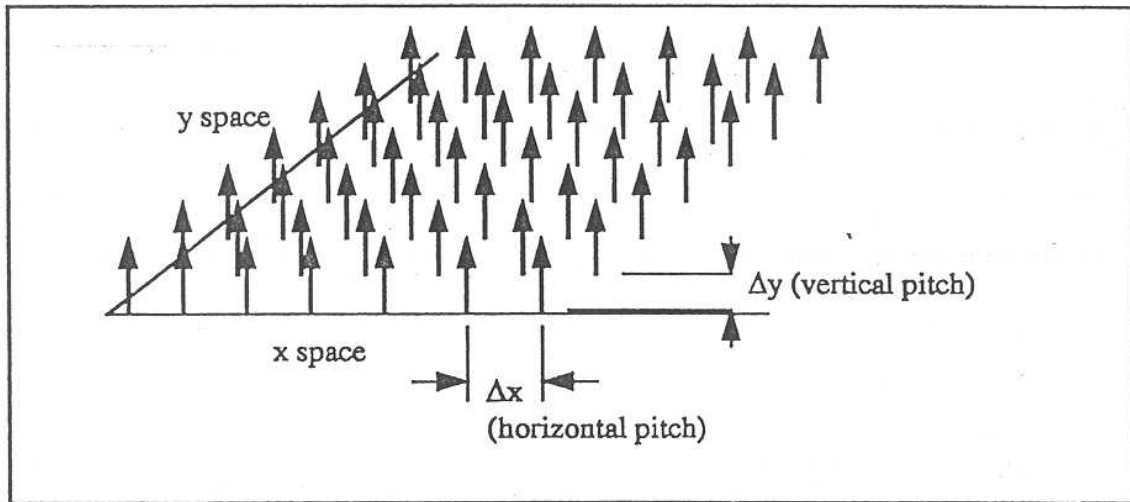
Figure K.1.   A Typical MRTD Plot "After [Ref. 1]".

Figure K.2.   Staring FPA as a Two-Dimensional Sampling Lattice "From [Ref. 3]".

2-D

Image Formation MTF

MTF_{optics}
MTF_{blur}
$MTF_{detector}$
$MTF_{Scene-Phasing}$ **(optional)**

Σ

2-D

White noise

Sampling and Aliasing

Image Reconstruction MTF

$MTF_{electronics}$
$PTF_{electronics}$
$MTF_{detector}$
$MTF_{display}$

2-D IFFT
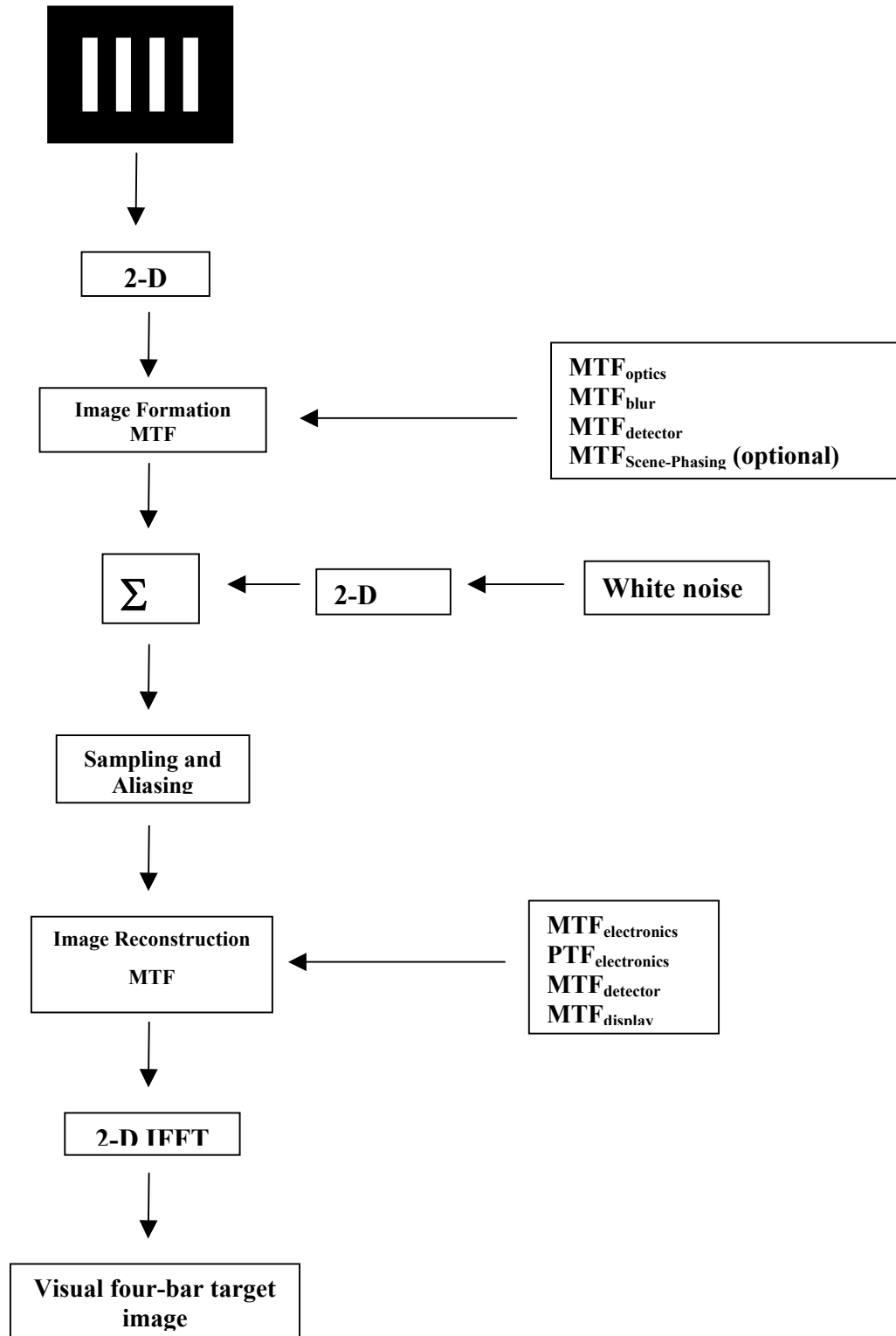
Visual four-bar target image

Figure K.3.   Block Diagram of the Virtual Thermal Image-Processing Model.
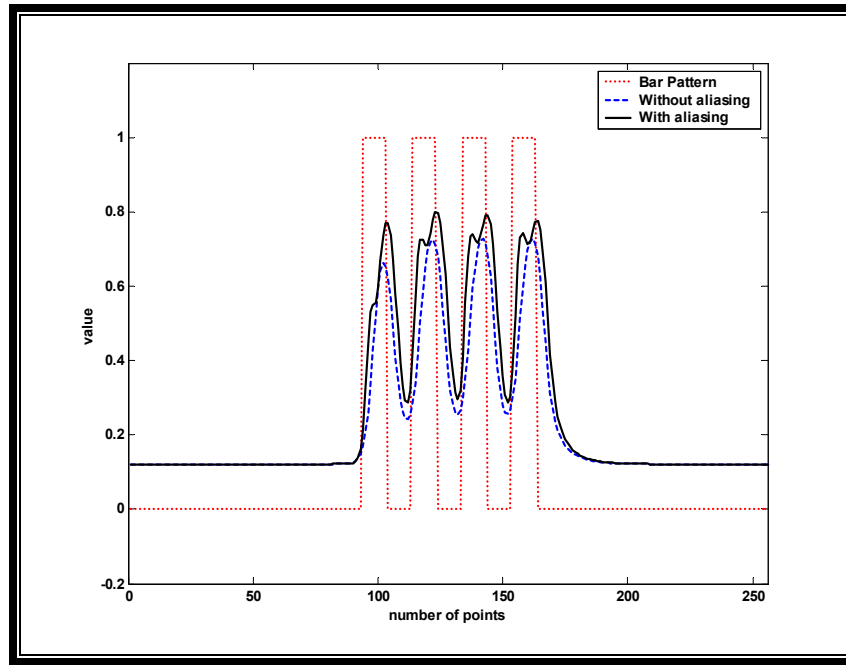
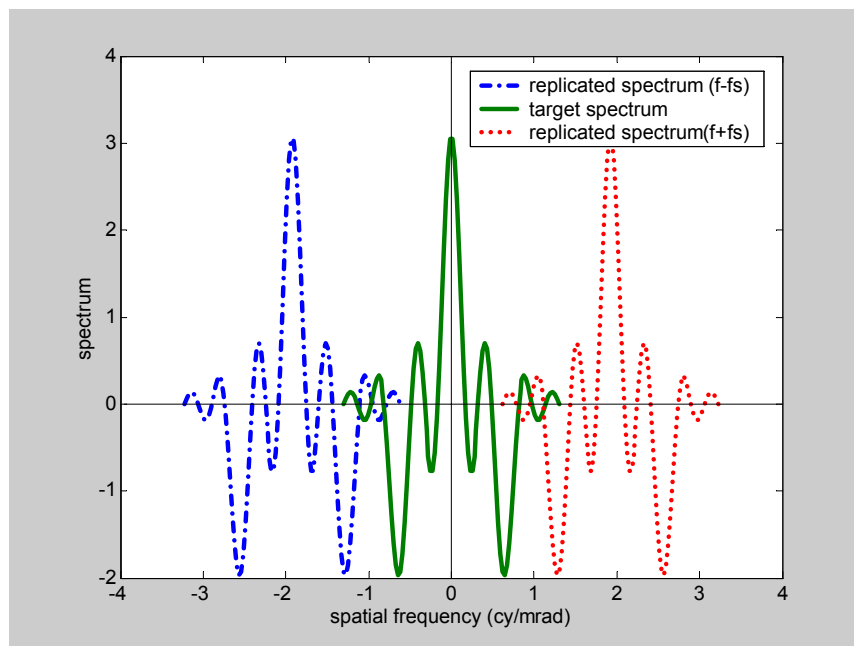**Figure K.4. Single Lines Passing through the Target and Image Centers (Four-Bar Frequency: 0.65 cy/mrad).**

Figure K.5. Horizontal MRTD Bar-Pattern along the x-Axis ($f_y = 0$) (Four-Bar Target Frequency: 0.65 cy/mrad).
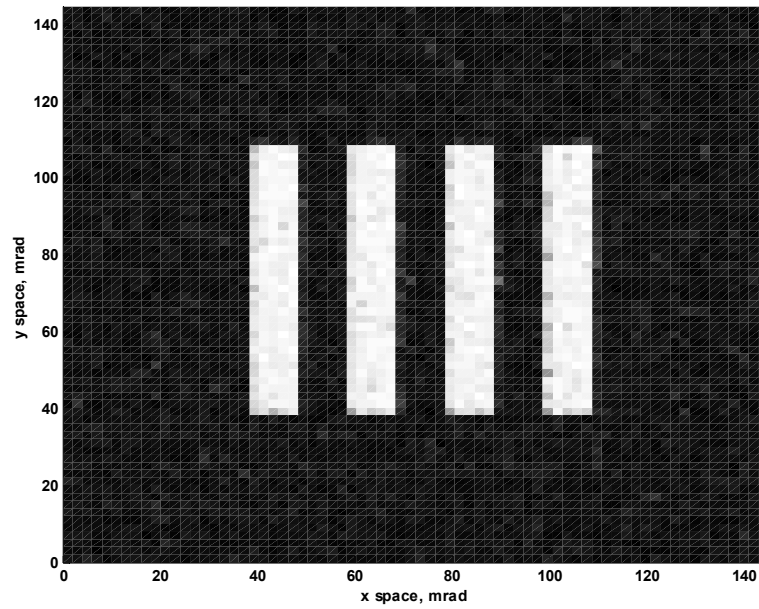
159

Figure K.6.   Image with Noise and Aliasing at 0.05 Cycles/mrad.
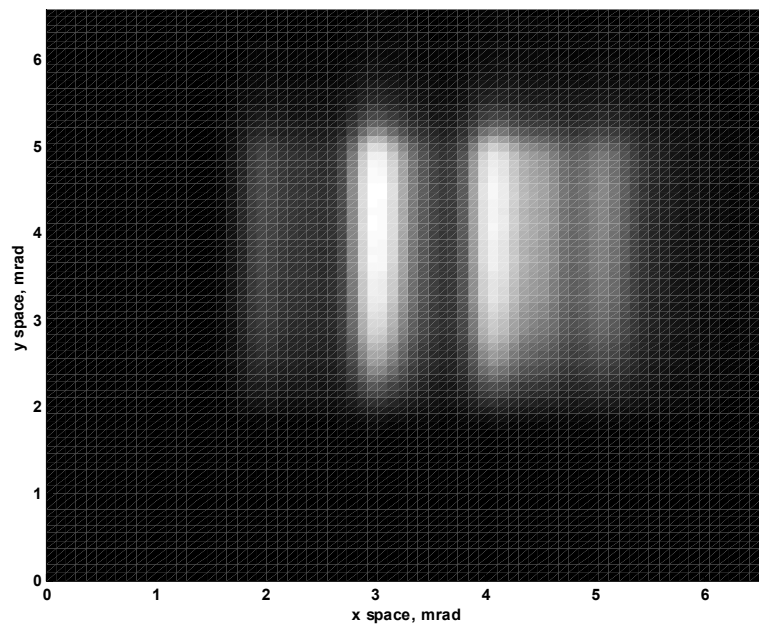

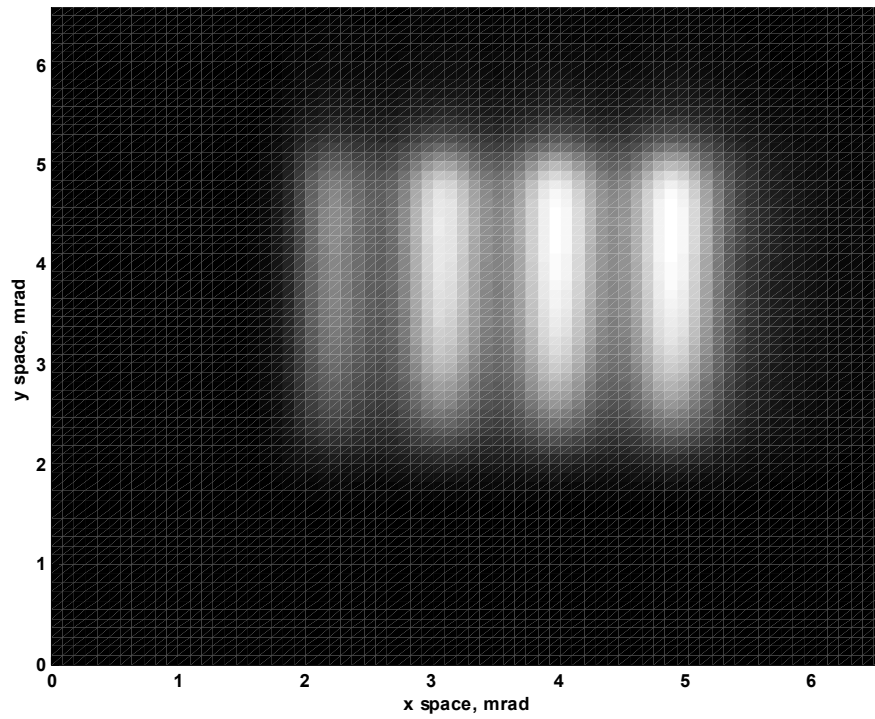**Figure K.7.   Image with Noise and Aliasing at 1.10 Cycles/mrad.**

Figure K.8.   Image with only Noise (no Aliasing) at 1.10 Cycles/mrad.

THIS PAGE INTENTIONALLY LEFT BLANK

LIST OF REFERENCES

1. Sendall R. L., F. A. Rosell, *Static Performance Model Based on the Perfect Synchronous Integrator Model*, Rosell F., Harvey G. eds. , NRL Report #8311, EOTPO Report No. 46, Washington D.C., May 10, 1979.

2. U.S. Army Night Vision and Electronic Sensors Directorate, *FLIR92 Thermal Imaging Systems Performance Model, Analyst's Reference Guide,* 1993.

3. Groen M. S., C. Koc, A. W. Cooper, R. J. Pieper, A Second Generation Visibility Based Model for Objective/Subjective FLIR MRTD, Proceedings of the IRIS Passive Sensors Symposium, Vol. 2, Naval Postgraduate School, Monterey, CA, March 1996.

4. Holst G. C., *Electro-Optical Imaging System Performance*, JCD Publishing, Second Edition, FL, 2000.

5. Driggers R. G., R. Vollmerhausen, Barbara O'Kane, Sampled Imaging Sensor Design Using the MTF Squeeze Model to Characterize Spurious Response*, SPIE*, Vol. 3701, April 1999.

6. Ratches J. A., Night Vision Modeling; Historical Perspective*, SPIE*, Vol.3701, April 1999.

7. Khalil Seyrafi and S. A. *Hovanessian*, *Introduction to Electro-Optical Imaging and Tracking Systems*, Artech House, Inc. MA, 1993.

8. Hudson R. D., *Infrared System Engineering,* John Wiley & Sons, New York, NY, 1969.

9. Driggers R. G., P. Cox, T. Edwards, *Introduction to Infrared and Electro-optical Systems*, Artech House, MA, 1999.

10. Lloyd J.M., *Thermal Imaging Systems*, Plenum Press, New York, 1975.

11. Acetta J.S. and D. L. Shumaker, *The Infrared and Electro-Optical Systems Handbook, Volume 4*, SPIE Optical Engineering Press, Bellingham, Washington, 1996.

12. Goodman J.W., *Introduction to Fourier Optics*, McGraw-Hill Physical and Quantum Electronics Series, 1968.

13. Watson E. A., R. A. Muse, F. P. Blommel, Aliasing and blurring in micro-scanned imagery, *SPIE,* Vol.1689 Infrared Imaging Systems, 1992.

14. Shumaker D. L., J. T. Wood and C. R. Thacker, *Infrared Imaging Systems Analysis*, The Environmental Research Institute of Michigan, 1993.

15. Rosell F., G. Harvey, *The Fundamentals of Thermal Imaging Systems*, NRL Report 8311, EOTPO Report No. 46, May 10 1979.

16. Holst G. C., *Testing and Evaluation of Infrared Imaging Systems,* JCD Publishing, Second Edition, FL, 1998.

17. McCracken W. and L. Wajsfelner, MRTD as a figure of merit, *SPIE,* Vol. 636, pp. 31-35, 1986.

18. Webb C. M., An Approach to 3-Dimensional Noise Spectral Analysis, *SPIE,* Vol. 2470, April 1995.

19. Groen M.S., Development and Validation of Second Generation Visibility-based Model for Predicting Subjective and Objective Minimum Resolvable Temperature Difference Performance for Staring Thermal Imaging Systems, Master's Thesis in Electrical Engineering and in Physics, Naval Postgraduate School, Dec 1995. Check all the way through

20. Ugarte A.R. and R.J. Pieper, A New Model for Predicting the MRTD Curves for Thermal Imagers, *24th Southeast Conference on System Theory*, pp. 231-374, March 1992.

21. Celik M., Measurements and Modeling Enhancements for the NPS Minimum Resolvable Temperature Difference Model, VISMOD II, Master's Thesis in Systems Engineering, Naval Postgraduate School, September 2001.

22. Edwards G.W., Objective Measurement of Minimum Resolvable Temperature Difference (MRTD) for Thermal Imagers, *SPIE*, Vol. 467, Image Assessment: Infrared and Visible (Sira), 1983.

23. Jacobs E., R. Driggers, T. Edwards and J. Cha, Virtual MRTD Experiments, *SPIE,* Vol.3701, pp.74-80, April 1999.

24. Mitsubishi Electronics Corporation, *IR-M500 Thermal Imager User's Guide*, Cypress, CA, January 1994.

25.   Mooney J.M., Effects of Spatial Noise on the Minimum Resolvable Temperature of a Staring Sensor, *Applied Optics*, Vol. 30, No. 23, pp. 3324-3332, August 1991.

26.   Park, S.K. and R. Hazra, Aliasing as Noise: A Quantitative and Qualitative Assessment, *SPIE*, Vol.1969, pp.54-65, August 1993.

27.   Orlando H. and M. Pappas, Automated Minimum Resolvable Temperature Implementation, *Proc. IRIS Passive Sensors*, Vol.2, pp. 115-121, 1996.

28.   Cuthbertson G., L. Shadrake, N. Short, A Technique for the Objective Measurement of MRTD, *SPIE,* Vol.590, pp. 179-192, 1985.

29.   Holst G., MRT Workshop, *SPIE,* Vol.2224, pp. 289-290, 1994.

30.   Bendall I., Automated Objective Minimum Resolvable Temperature Difference, *SPIE,* Vol.4030, pp. 50-58, 2000.

31.   Ugarte A.R., Modeling for Improved Minimum Resolvable Temperature Difference Measurements, Master's Thesis in Systems Engineering and Electrical Engineering, Naval Postgraduate School, Sep 1991.

THIS PAGE INTENTIONALLY LEFT BLANK

INITIAL DISTRIBUTION LIST

1.   Defense Technical Information Center
        Ft. Belvoir, Virginia

2.   Dudley Knox Library
        Naval Postgraduate School
        Monterey, California

3.   Professor Alfred W. Cooper, Code PH/Cr
        Naval Postgraduate School
        Monterey, California

        _____

4.   Professor Ronald J. Pieper, Code EC/Pr
        Naval Postgraduate School
        Monterey, California

        _____

5.   Yucel Kenter
        Muhittin mah. Kenan Evren cad. Guvenc apt. A/19
        Corlu, Turkey

        _____

6.   Professor Dan Boger, Chairman, Code IW
        Naval Postgraduate School
        Monterey, California

        _____